Microscopy and Microanalysis (2021), 1–53
doi:10.1017/S1431927621012125

Microscopy AND Microanalysis

Review Article

Advances and Applications of Atomic-Resolution Scanning Transmission Electron Microscopy

Jingyue (Jimmy) Liu
Department of Physics, Arizona State University, Tempe, AZ 85287, USA

Abstract

Although scanning transmission electron microscopy (STEM) images of individual heavy atoms were reported 50 years ago, the applications of atomic-resolution STEM imaging became wide spread only after the practical realization of aberration correctors on field-emission STEM/TEM instruments to form sub-Ångstrom electron probes. The innovative designs and advances of electron optical systems, the fundamental understanding of electron–specimen interaction processes, and the advances in detector technology all played a major role in achieving the goal of atomic-resolution STEM imaging of practical materials. It is clear that tremendous advances in computer technology and electronics, image acquisition and processing algorithms, image simulations, and precision machining synergistically made atomic-resolution STEM imaging routinely accessible. It is anticipated that further hardware/software development is needed to achieve three-dimensional atomic-resolution STEM imaging with single-atom chemical sensitivity, even for electron-beam-sensitive materials. Artificial intelligence, machine learning, and big-data science are expected to significantly enhance the impact of STEM and associated techniques on many research fields such as materials science and engineering, quantum and nanoscale science, physics and chemistry, and biology and medicine. This review focuses on advances of STEM imaging from the invention of the field-emission electron gun to the realization of aberration-corrected and monochromated atomic-resolution STEM and its broad applications.

Key words: atomic resolution, electron microscopy, imaging, materials science, nanostructure

(Received 1 January 2021; revised 5 June 2021; accepted 8 June 2021)

Introduction

Human beings have long been, and will continue to be, fascinated by Nature and how it works. Curiosity and a thirst for understanding Nature have fueled scientific and technological breakthroughs which have been continuously improving our quality of life. We develop our perception of Nature by sensing of which visualization plays a critical role. Since human eyes have a very limited angular resolution (~1 arcminute or approximately 0.0003 radians), our naked eyes cannot directly visualize either tiny features/creatures, such as individual living bacteria, or gigantic individual stars within constellations that are far away. The early practice of making spectacles and magnifiers with the goal of "seeing" small features more clearly led to the development of two important scientific tools: The telescope for clearly observing things far away and the microscope for examining small features/creatures that our naked eyes could not do. Both the early telescope and microscope relied on the unique properties of glass lenses that possess the power to manipulate light rays. The continuous improvement in telescopes has vastly expanded our knowledge of the Universe, while the development of various types of microscopes has enabled us to directly observe bacteria, viruses, molecules, and even individual atoms. The invention of both the telescope and the microscope has unlocked countless mysteries of Nature and enabled numerous discoveries that have positively impacted our daily life.

In this review, the goal is to account for the major advances in one particular type of microscope that is now broadly used for analyzing matter at the atomic scale: the scanning transmission electron microscope (STEM). Although STEM was used to image single metal atoms as early as 1970 (Crewe et al., 1970), it took a long time for the broader research communities to effectively utilize this powerful characterization method. The practical realization of the correction of lens aberrations to routinely achieve sub-Ångstrom image resolution with picometer precision and high chemical sensitivity greatly enhanced the impact of STEM and associated techniques on many research frontiers. Such an accomplishment has revolutionized how we understand matter at the atomic level and will have a tremendous impact on how we understand Nature. The significance of this accomplishment is evidenced by the recent award of the 2020 Kavli Prize in Nanoscience to Harald Rose, Maximilian Haider, Knut Urban, and Ondrej L. Krivanek "for sub-Ångstrom resolution imaging and chemical analysis using electron beams" (Rose et al., 2020).

Since many excellent reviews have been published on the topic of aberration-correction (e.g., Rose, 2008, 2009; Hawkes, 2009*a*, 2009*b*, 2015; Septier, 2017; Hawkes & Krivanek, 2019) we will focus, in this review, on the advances of forming high-resolution images by scanning a finely focused electron probe and how to

Email: jingyue.liu@asu.edu

Cite this article: Liu J (2021) Advances and Applications of Atomic-Resolution Scanning Transmission Electron Microscopy. *Microsc Microanal*. doi:10.1017/S1431927621012125

© The Author(s), 2021. Published by Cambridge University Press on behalf of the Microscopy Society of America. This is an Open Access article, distributed under the terms of the Creative Commons Attribution licence (http://creativecommons.org/licenses/by/4.0/), which permits unrestricted re-use, distribution, and reproduction in any medium, provided the original work is properly cited.

Downloaded from https://www.cambridge.org/core. IP address: 68.98.49.119, on 04 Sep 2021 at 06:14:57, subject to the Cambridge Core terms of use, available at https://www.cambridge.org/core/terms. https://doi.org/10.1017/S1431927621012125

correctly interpret such images. For the fundamental principles and applications of aberration-corrected STEM (ac-STEM), the interested reader is strongly encouraged to read the excellent reviews/books on these topics (Rose, 2009; Pennycook & Nellist, 2011; Erni, 2014; Tanaka, 2014; Hawkes & Krivanek, 2019; Nellist, 2019).

A Brief History of the Light Microscope and the Birth of the Electron Microscope

The Dutch eyeglass makers Hans Martens/Zacharias Janssen are frequently credited for inventing the compound microscope (Orchard & Nation, 2014), while Hans Lippershey, another Dutch eyeglass maker, is considered to be the first person to patent a telescope by assembling a concave eyepiece aligned with a convex objective lens (Van Helden, 1977). The early practical applications of these lens-based telescopes and microscopes were clearly reflected in their respective nicknames as spyglasses and flea glasses. Galileo Galilei, in 1609, constructed his own telescope and discovered that the moon was not a perfect sphere; and with finely polished lenses, he subsequently conducted scientific observations of celestial objects and discovered many distant systems that had not been previously known (Drake, 2003). Even though the modern James Webb Space Telescope (expected to be launched in late 2021) may cost more than $10 billion, our understanding of the Universe started by stacking two glass lenses to form a rudimentary telescope.

Although the early development and applications of the scientific microscope are difficult to trace exactly, Robert Hooke's publication of *Micrographia* in 1665 (Hooke, 1665) clearly demonstrated the power of using compound microscopes to observe tiny features that naked human eyes had not been able to do. Hooke also coined the word "cell" for describing the observed structures of the cork bark under a compound microscope. The discovery of the cell was made possible through the invention of the microscope. Because of the aberrations of poorly polished glass lenses and other related issues, the early compound microscopes could not provide high magnification images without severe image distortion. On the other hand, with a finely polished single glass lens, Antonie van Leeuwenhoek was able to examine a variety of biological specimens in an aqueous environment, even the dynamical movement of tiny creatures, with a magnification as high as ~300× (Lane, 2015). Through extensive observations via his refined single-lens microscope, van Leeuwenhoek discovered many secrets of Nature such as bacteria, microscopic protists, sperm cells, blood cells, and microscopic nematodes and rotifers. The invention of the light microscope made the invisible world visible and enabled many discoveries that helped us better understand Nature, created new scientific disciplines, and significantly improved the quality of life of human beings.

To understand how a microscope works and how to reliably produce high-quality light microscopes, Ernst Abbe formulated an imaging theory and established a resolution limit for light microscopes: due to diffraction effect, the wavelength of the light source controls the ultimate attainable image resolution of a light microscope to about half of the wavelength of the light source (Abbe, 1873). Even if the lens aberrations are perfectly corrected, the highest attainable resolution of a light microscope has been limited to about 200 nm. Such a theoretical limit prevented a clear observation of subcellular structures with smaller sizes. The early work on trying to overcome the image resolution barrier by scanning a localized light probe was not very successful (Synge, 1928, 1931, 1932). In 1957, Marvin Minsky filed a patent describing new approaches to constructing a confocal scanning microscope (Minsky, 1957, 1988). The subsequent incorporation of a laser beam into Minsky's design (Davidovits & Egger, 1969, 1971), and the use of fluorescent markers for three-dimensional (3D) detection of biological systems (Cremer & Cremer, 1978), significantly improved the image resolution and made it possible to obtain optical sectioning of 3D objects (Wilson, 2011). By using innovative approaches to generating and detecting fluorescent signals, the recent development of super-resolution microscopes, tremendously aided by the development of faster computers, high-quality lasers, fluorophores, and algorithms for image acquisition and processing, proved extremely successful in imaging biological objects with an image resolution of <20 nm (which can be improved to ~1 nm), enabling observations of dynamic movements of subcellular systems under physiologically relevant environment (Moerner & Kador, 1989; Betzig & Trautman, 1992; Betzig & Chichester, 1993; Hell & Wichmann, 1994; Betzig, 1995; Dickson et al., 1997; Klar et al., 2000; Hell, 2003; Betzig et al., 2006; Rust et al., 2006; Huang et al., 2009; Pujals et al., 2019).

Abbe's theory predicts that the use of much shorter wavelengths should provide improved image resolution. The de Broglie's hypothesis of matter waves (de Broglie, 1923, 1924), the subsequent experiments by Davisson and Germer to unambiguously verify the wave nature of electrons (Davisson & Germer, 1927), and Busch's theoretical prediction that a cylindrical magnetic lens could be used to focus electrons (Busch, 1926), analogous to the way light is refracted by a glass lens, led to the emergence of new microscopes based on electrons instead of light. Ruska and Knoll audaciously took the adventure of constructing a new type of microscope by using high-energy electrons emitted from a metal tip, which possess a wavelength much shorter than that of visible light (Ruska & Knoll, 1931; Ruska, 1987). With refinement of the electron optics, such an electron microscope easily provided an image resolution much better than any contemporary light microscopes. Since charged electrons are strongly scattered by molecules, a high-vacuum chamber is needed to house the electron gun, the sample of interest, and the recording media. The use of electrons, instead of light, to form images of matter significantly enhanced our understanding of the micro- and nano-world by attaining images of matter with continuously improved image resolution (Fig. 1). The requirement of maintaining a high vacuum within an electron microscope, in contrast to light microscopes, and the strong interaction between charged particles and matter impose significant limitations on practical applications of the various types of electron microscopes.

Development of the Scanning Transmission Electron Microscope

The Early Development

The invention of the fax machine by Alexander Bain is usually considered as the first use of forming images by a scanning system (Bain, 1843; McMullan, 1990). To overcome the Abbe limit on the resolution of light microscopes, Synge applied the scanning method, by using a light probe with an aperture smaller than the wavelength of the light, to form scanned images (Synge, 1928). Although there were no major breakthroughs in improving image resolution, Synge proposed the use of piezo-electric actuators, the formation of a visible image on a phosphor screen, and the image contrast expansion by processing electronic signals

Downloaded from https://www.cambridge.org/core. IP address: 68.98.49.119, on 04 Sep 2021 at 06:14:57, subject to the Cambridge Core terms of use, available at https://www.cambridge.org/core/terms. https://doi.org/10.1017/S1431927621012125

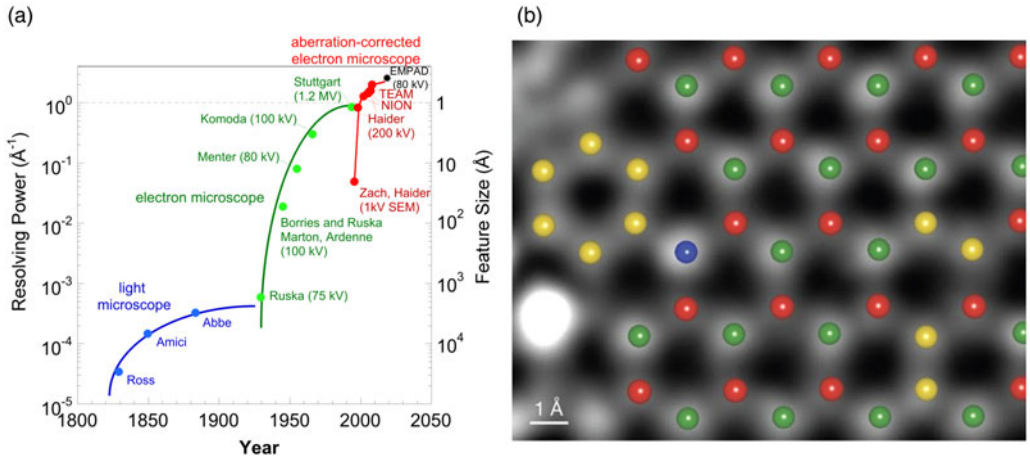

Fig. 1. (**a**) Hardware advances in resolving power of microscopes. (**b**) Atom-by-atom structural and chemical analysis by annular dark-field electron microscopy. Part of a density functional theory simulation of a single BN layer containing the experimentally observed substitutional impurities overlaid on the corresponding part of the experimental image. Boron in red; Carbon in yellow; Nitrogen in green; Oxygen in blue. (a) Adapted from Rose (2009) and Muller (https://devicematerialscommunity.nature.com/search?utf8=%E2%9C%93&query=muller). (**b**) Adapted from Krivanek et al. (2010*a*).

(Synge, 1928, 1931, 1932). All these early proposals have been effectively utilized for developing the state-of-the-art scanning microscopes. Stintzing filed a patent for a proposed scanning microscope to be capable of automatic detection and measurement of particles using a light or electron beam (Stintzing, 1929; McMullan, 1989). Since the possibility of focusing electrons was not known at that time, Stintzing proposed the use of crossed slits to form small diameter light or electron probes (McMullan, 1989). No practical scanning microscopes were constructed to demonstrate the feasibility of these scanning imaging systems.

Soon after the construction of the first transmission electron microscope (TEM), Max Knoll started working on television camera tubes and developed an electron-beam scanner for observing the targets of these tubes. Knoll was the first to publish images obtained by scanning an electron beam (Knoll, 1935). The electron-beam scanner that Knoll constructed, with electron energies in the range of 500–4,000 eV, possessed all the principal features of a modern scanning electron microscope (SEM). Knoll demonstrated that the image magnification of an SEM could be controlled by varying the ratio of the scan amplitudes: with a fixed display size, the smaller the scanned area, the higher the image magnification. Such an understanding of magnification of scanned images was also realized by the television and electron microscope pioneer Zworykin (Zworykin, 1934; Zworykin et al., 1942) who worked on a light microscope fitted with a TV camera. With the electron-beam scanner, Knoll investigated not only cathode-ray tubes but also other types of solid samples and determined the contrast mechanisms of his scanning images (Knoll, 1941; McMullan, 1995).

Manfred von Ardenne, an eminent applied physicist and prolific inventor, built the first STEM (Fig. 2a) with the goal to image thicker samples, which posed a major problem for TEM imaging due to chromatic effects, without degrading image resolution (McMullan, 1995). In a series of publications within a short period of time, von Ardenne described detailed analyses of the design and performance of probe-forming electron optics using magnetic lenses (von Ardenne, 1938*a*, 1938*b*, 1938*c*, 1939, 1940). He discussed the effects of lens aberrations on the probe size and how to calculate the current in an electron probe, showed how detectors should be placed for bright-field (BF) and dark-field (DF) STEM imaging, and considered the effects of electron beam and amplifier noise on image quality. With the use of a smaller electron probe for high-resolution imaging, the total electron-beam intensity within the electron probe was, however, drastically reduced, resulting in a long recording time to obtain each visually observable image. Since there were no suitable low-noise electronic detectors available at that time, photographic films had to be used to record reasonable quality STEM images. The long acquisition time to obtain each small-probe size STEM image imposed a fatal limitation on practical STEM imaging since one could not focus the electron probe properly without quickly examining the raster image. When large electron probe sizes, which provided higher probe current for rapid raster images, were used only low-resolution STEM images were obtained, offering no advantages over TEM. The lack of appropriate electron detectors and bright electron sources at that time severely limited the development and applications of high-resolution STEM. On the other hand, the high yield of low-energy secondary electrons and the development of the highly efficient Everhart-Thornley detector (Everhart & Thornley, 1960) made it possible to obtain high-quality SEM images of surfaces of various types of samples, leading to the successful commercialization of the first SEM by the Cambridge Instrument Company (Oatley, 1982).

Albert Crewe's Field-Emission Scanning Electron Microscope

Crewe proposed a new type of scanning microscope in 1963 with the objective to overcome the barriers to improving image resolution by using electron beams (Crewe, 1963). In his 1966 paper, Crewe, after analyzing the probe-forming lenses of the SEM (Oatley et al., 1965; Pease & Nixon, 1965), realized that the existing scanning microscopes were severely limited by electron source problems: The electron source brightness was too low and, therefore, it was not possible to de-magnify such an electron source to atomic size with any usable current (Crewe, 1966). Crewe realized the practicality of field emission from a small tungsten tip (Fowler & Nordheim, 1928; Dyke et al., 1953; Martin et al., 1960; Gomer, 1961; Butler, 1966; Crewe et al., 1968*b*) and proposed the use of such a tip as the electron gun to generate a high-brightness electron source. The current density from a cold field-emission gun

Downloaded from https://www.cambridge.org/core. IP address: 68.98.49.119, on 04 Sep 2021 at 06:14:57, subject to the Cambridge Core terms of use, available at https://www.cambridge.org/core/terms. https://doi.org/10.1017/S1431927621012125

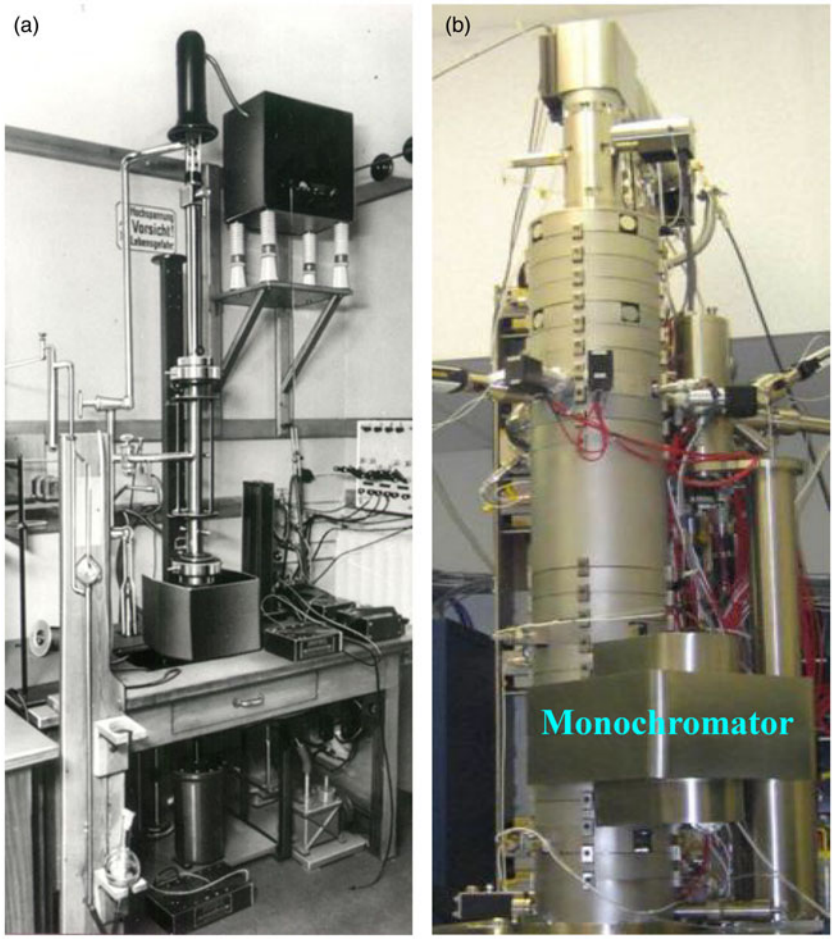

Fig. 2. (**a**) Manfred von Ardenne developed the first scanning transmission electron microscope (1938), with an electron-beam diameter on target of ~10 nm. His first image was a zinc oxide crystal at 8,000× magnification. Adapted from Science/AAAS Custom Publishing Office (http://poster.sciencemag.org/sem/#). (**b**) The Nion aberration-corrected and monochromated UltraSTEM 100 at Arizona State University: sub-Ångstrom resolution at 60/100 kV, about 1 Ångstrom resolution at 30/40 kV, and 10 meV energy solution in ultrafast EELS.

(10^8–10^9 A/cm^2 sr) could be orders of magnitude higher than that from a thermionic electron gun (<10^6 A/cm^2) and the diameter of the virtual source could be managed to become less than 10 nm. The use of a field-emission gun (FEG) was expected to drastically reduce the electron probe size and consequently to improve the image resolution of both SEM and STEM. Crewe further proposed the design of a new microscope with the use of quadrupole lenses and estimated that an electron source size of 3 nm could be achievable. The new microscope needed to maintain an ultrahigh vacuum to stabilize electron emission, and the transmitted electrons could be detected by a high-speed scintillator photomultiplier system. The newly proposed STEM could be easily fitted with an electrostatic spectrometer (Hillier & Baker, 1944) for analyzing the energy of the transmitted electrons to enhance image contrast or to provide chemical contrast imaging. Since an ultrahigh vacuum was required, it was expected that contamination issues would not pose a significant problem on either image resolution and/or image contrast.

Crewe and colleagues (Crewe et al., 1968*c*) published the design of a simple STEM (Fig. 3a) and built an STEM with a field-emission electron source and one lens, providing high-contrast images with 3 nm resolution. The field-emission tip required a vacuum pressure below 10^{-9} Torr for stable operation. The power of using a tungsten field-emission tip was further demonstrated by the fact that even with the use of only the FEG and without the use of any focusing lenses, an image resolution of ~10 nm was obtained in transmission electron micrographs (Crewe et al., 1969). The achievable electron probe current on the order of 100–10 pA, which allowed electron micrographs to be taken with scan times of 10 s, significantly improved from that of von Ardenne's STEM. The use of an FEG not only reduced the electron probe size but also drastically increased the probe current density, both of which enabled the attainment of high-resolution STEM images with a reasonable signal-to-noise ratio. The improved design and the astonishing performance of the new type of STEM, constructed by Crewe and his research group, were highlighted by the capability of directly observing single heavy atoms (Crewe & Wall, 1970; Crewe et al., 1970). With the improved STEM design, Crewe and colleagues constructed a stronger cylindrically symmetrical magnetic lens (focal lengths of 0.6–1.0 mm) to reduce the spherical aberration coefficient (~0.4 mm); incorporated an annular detector (Cosslett, 1965) to enhance the image contrast of different elements and to further improve signal strength; and attached an electrostatic electron spectrometer (0.3 eV resolution with 25 keV primary electron beam) to collect transmitted electrons with specific energies. The unique features of the new STEM as well as discussions on the various parameters that affect the final probe size were presented (Crewe & Wall, 1970). Since the probe-forming lens and the

Downloaded from https://www.cambridge.org/core. IP address: 68.98.49.119, on 04 Sep 2021 at 06:14:57, subject to the Cambridge Core terms of use, available at https://www.cambridge.org/core/terms. https://doi.org/10.1017/S1431927621012125

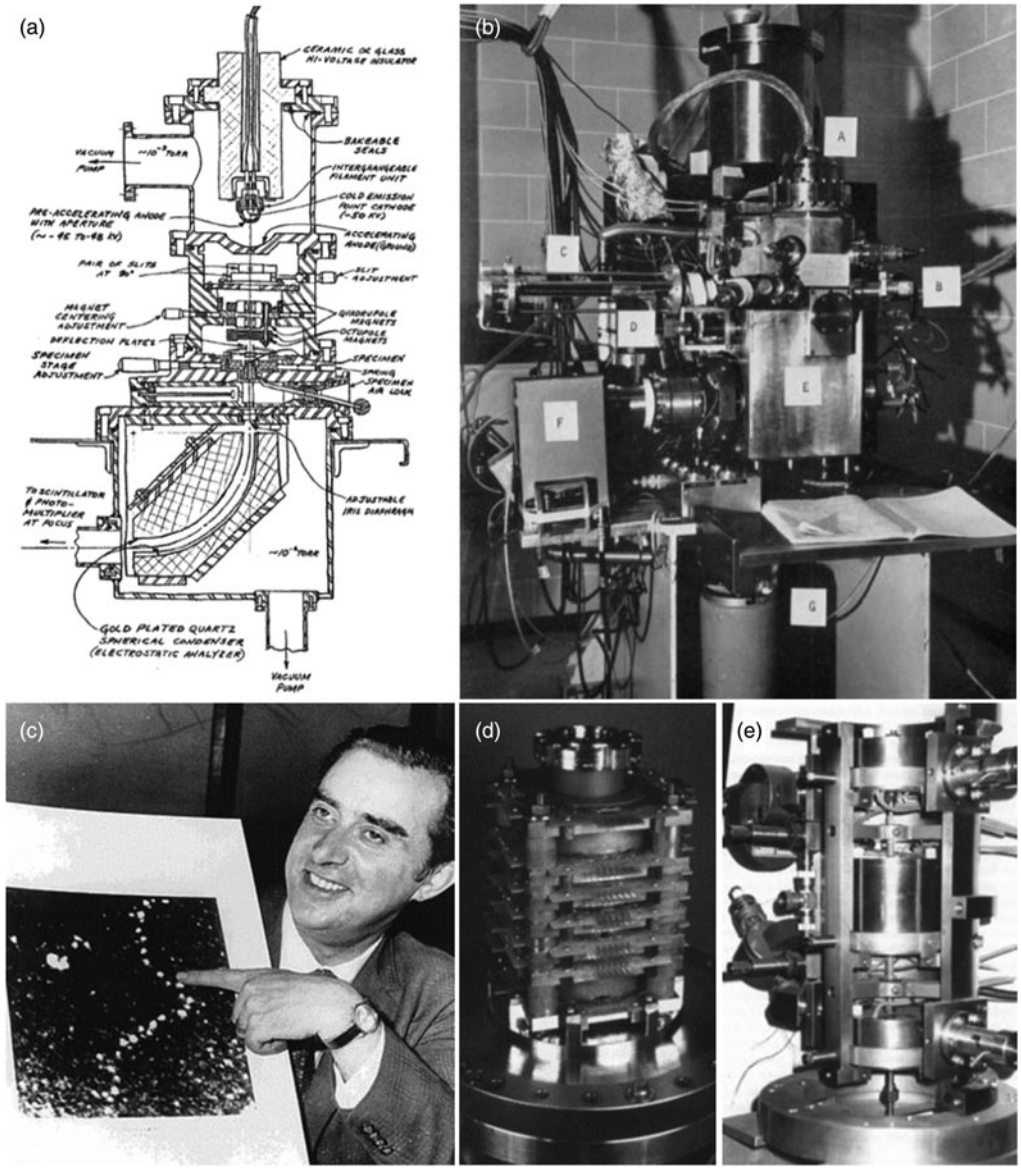

Fig. 3. Albert Crewe's first STEM design (**a**), the 0.5 nm STEM instrument (**b**), a chain of thorium atoms imaged on his STEM (**c**), the quadrupole–octupole corrector (**d**), and the sextupole corrector (**e**). Retrieved from https://www.microscopy.org/images/posters/Crewe.pdf.

electron gun were rigidly connected together, the only alignment of the optical system was to make sure that the field-emission tip was placed on the optical axis of the microscope system and that the tip emission cone would not change during operation. The authors realized that, in strong contrast to conventional TEM, the electron probe current and the collected signal strength were independent of image magnification. Since the signal strength did not change with the image magnification, one could operate the STEM at high image magnifications (up to 5×10^6). The Crewe's research group also realized that "phase contrast can be obtained by using a large aperture above the specimen and very small aperture below the specimen."

Even with a 0.5 nm electron probe at 25 kV (Fig. 3b), Crewe and colleagues were able to visualize individual heavy atoms supported on ultrathin carbon films (Crewe et al., 1970). They obtained two types of STEM images by collecting scattered electrons with an annular detector (excluding the directly transmitted electrons) and inelastically scattered electrons (passing through the hole of the annular detector) by the electron spectrometer. The ratio of these two images was expected to reduce the dependence of image contrast on thickness variations of the supporting carbon film, resulting in contrast enhancement of heavy atoms. Through detailed analyses and comparison of the experimentally measured visibility factors to those of theoretical calculations for carbon-supported uranium and thorium atoms, the authors concluded that the bright spots in their STEM images represented those of individual uranium or thorium atoms. To further corroborate their conclusion of visualizing individual heavy atoms, special samples, which consisted of isolated atom pairs, were prepared and examined. The experimentally obtained images matched the geometric patterns that were expected from the respective molecules supported on ultrathin carbon films. This was the first time ever to achieve the goal of directly imaging individual atoms with an electron microscope, and therefore, the FEG STEM surpassed the capability of conventional TEM for imaging individual heavy metal atoms (Fig. 3c; Crewe et al., 1970). Four main factors

Downloaded from https://www.cambridge.org/core. IP address: 68.98.49.119, on 04 Sep 2021 at 06:14:57, subject to the Cambridge Core terms of use, available at https://www.cambridge.org/core/terms. https://doi.org/10.1017/S1431927621012125

accounted for imaging individual heavy atoms with a probe size of ~0.5 nm: (1) the high-current density of the FEG, (2) the large distances between the heavy atoms, (3) the strong heavy-atom contrast, and (4) the ultrathin carbon support which significantly reduced the strength of the background signal. The strong heavy-atom contrast originated from the ratio signal which strongly depended on the atomic number "Z" of the individual heavy atoms (Crewe, 1971). Therefore, by processing different categories of transmitted electrons to form new images, one could enhance elemental differentiation of the samples of interest, especially for heavy metal atoms or clusters supported on amorphous, light-element thin films. With the capability of analyzing inelastically scattered electrons, Crewe and colleagues (Crewe et al., 1971*a*, 1971*b*) studied the interactions of fast electrons with biological molecules and measured the corresponding energy-loss spectra of various nucleic acid bases. They further studied the potential of utilizing the energy-loss signal to enhance image contrast of biological specimens and investigated the phenomena of electron-beam-induced radiation damage and provided a measure of these effects.

With further improvement of the STEM design, operating at relatively higher electron-beam energies, and collecting elastically scattered electrons with an annular dark-field (ADF) detector, not only individual heavy atoms were imaged, but also atomic columns of small crystallites of uranium and thorium compounds were resolved (Wall et al., 1974*b*). Furthermore, the authors used line intensity profiles of individual mercury atoms to estimate the finely focused electron probe size and demonstrated a full width at half maximum (FWHM) of 0.25 ± 0.02 nm at 42.5 kV with a total electron flux of 10^7 electrons/Å^2. Since the signal-to-noise ratio available from a single heavy atom on a carbon support would increase with improvement of instrumental resolution, the authors proposed that higher electron-beam voltages (e.g., 100 kV) and a smaller probe size (e.g., <0.2 nm) would allow sufficient signal-to-noise for directly visualizing single atoms over more than half of the periodic table (Crewe, 1974; Wall et al., 1974*a*, 1974*b*). By this time, the use of an FEG for STEM imaging had been unambiguously proved successful, especially for applications in imaging biological systems stained with heavy metal atoms or clusters.

The flexibility of STEM detectors, together with the capability of performing electron energy-loss analysis of transmitted electrons, provided a new approach to quantitatively evaluating mass thickness and composition of biological structures on a nanometer scale. The ADF imaging method was extensively used to determine the molecular masses of macromolecular assemblies and to visualize isolated protein assemblies via heavy metal labeling, leading to broad STEM applications in biology (Crewe, 1971; Wall & Hainfeld, 1986; Hainfeld, 1987; Colliex & Mory, 1994; Thomas et al., 1994; Sousa et al., 2008; Engel, 2009; Sousa & Leapman, 2012). The early applications of electron energy-loss spectroscopy (EELS) to biological systems (Crewe et al., 1971*a*, 1971*b*; Isaacson, 1972; Isaacson & Johnson, 1975) spurred EELS nanoanalysis in cell biology, pathology, microbiology, histology, and other branches of biomedical sciences (Ottensmeyer & Andrew, 1980; Leapman & Ornberg, 1988; Leapman & Andrews, 1992; Leapman, 2003; Aronova & Leapman, 2012).

The Emerging STEM Research and the Commercial Development of STEMs

The success of Crewe's new STEM and the progressive improvement of image resolution in conventional TEM, from crystal lattice imaging (Menter, 1956; Dowell, 1963; Komoda, 1966; Allpress et al., 1969) to structural imaging (Iijima, 1971; Cowley & Iijima, 1972; Allpress & Sanders, 1973), clearly galvanized the excitement for developing high-voltage, high-resolution electron microscopes. Cowley and Strojnik started designing and building a 600-kV transmission scanning electron microscope and reported the initial results of their effort (Cowley & Strojnik, 1968, 1969; Cowley, 1970; Cowley et al., 1970). In designing this high-voltage STEM, they used two lenses to form a small electron probe and added deflection systems to manipulate scattered electrons in order to obtain decent electron diffraction patterns and to direct the scattered electrons into the electron spectrometer for EELS analysis. Cowley specifically emphasized the usefulness of simultaneously acquiring STEM images and diffraction patterns from small regions of interest, for example, from dislocations or other types of defects (Cowley, 1970). If the scanning electron probe was stopped at any point of interest, a diffraction pattern, originating from a region with an area equal to the resolution limit of the STEM, would be recorded. In addition to investigating various STEM imaging modes, Cowley and colleagues studied the dependence of electron diffraction from crystalline samples on the defocus of the electron probe and discussed the origin of the fine structures in the observed convergent beam electron diffraction disks (Cowley et al., 1970; Smith & Cowley, 1971), similar to, but not exactly the same as, those reported for convergent beam electron diffraction (CBED) in conventional TEM (Cockayne et al., 1967). Cowley reported that the nature of the observed diffraction patterns depended on the aperture size of the probe-forming lens and that the lens aberrations (e.g., spherical and chromatic aberrations) had an effect on the observed fine structures in the wide-angle CBED patterns. When the electron beam was out-of-focus shadow images of the specimen within the wide-angle CBED disks appeared. It is interesting to note that Cowley and colleagues, based on the high-penetration power of high-energy electrons and the fact that, in an STEM, no imaging lenses were needed after the sample, proposed designs for conducting electron microscopy imaging and diffraction experiments on samples that could be exposed to air or other types of gases (Cowley et al., 1970). Cowley and Strojnik did not seem to consider the use of an FEG as the electron source. Even though they used high voltages and two lens systems to form the electron probe, the resolution of this high-voltage STEM was limited to ~1 nm.

Other research groups worldwide either proposed or started the construction of high-voltage electron microscopes with an expectation of approaching 0.1 nm image resolution, significantly extending the electron microscopes' capabilities, especially for studies of biological systems. Such an enthusiasm of the electron microscopy research community was clearly reflected in a special Physics Today report (Lubkin, 1974). Even the abstract of this special report described the excitement and the potential of high-resolution STEMs/TEMs as described below.

> "Several groups are building electron microscopes with high voltage or high resolution or both that should distinctly extend their capabilities, particularly for observations in biology. One such group, which we recently visited at the Cavendish Laboratory, University of Cambridge, is building a 600-kV conventional microscope that is expected to have a resolving power approaching 1 Å, according to V. E. Cosslett and W. C. Nixon, who head the Cavendish team. Among those hoping to extend the frontiers of electron microscopy, besides the Cavendish, are groups at Oak Ridge National Laboratory, Cornell University, the University of Kyoto, the University of Nagoya, the University of Chicago and Arizona State University."

Downloaded from https://www.cambridge.org/core. IP address: 68.98.49.119, on 04 Sep 2021 at 06:14:57, subject to the Cambridge Core terms of use, available at https://www.cambridge.org/core/terms. https://doi.org/10.1017/S1431927621012125

Crewe's development and demonstration of the power of his high-resolution, field-emission STEM stimulated the commercial development of such electron microscopes. Komoda and his colleagues in Japan started constructing scanning electron microscopes similar to Crewe's microscope (Komoda & Saito, 1972; Komoda et al., 1972). The constructed field-emission SEM could be used with accelerating voltages up to 50 kV with capabilities for STEM imaging as well as secondary electron imaging. The improved resolution in secondary electron imaging, due to the use of a smaller but high-current-density electron probe, eventually led to the successful development of the first commercialized cold FEG SEM in 1972. By 1975, Hitachi completed the design and development of a 50-kV cold FEG STEM which revealed 0.2 nm lattice spacings of Au in phase-contrast BF STEM images (Inada et al., 2009). Based on Peter Hawkes' account (Hawkes, 2009*a*, 2009*b*), in addition to Vacuum Generators, two other companies, AEI (Associated Electrical Industries) of Britain and Siemens of Germany, constructed STEMs in the early 1970s. By 1973, the AEI STEM provided an image resolution of ∼1.0 nm and could operate at 80 kV. Later, prototype AEI STEMs improved the image resolution to ∼0.3 nm and lattice spacings of ∼0.2 nm were discernible. The Siemens FEG STEM could operate from 10 to 100 kV and electron deflection systems both before and after the specimen were incorporated to adjust the electron beam to allow proper detection of scattered electrons by the imaging detectors/electron analyzer and to permit recording of diffraction patterns. The Siemens STEM demonstrated the employment of large bright-field detectors and ADF detectors to suppress phase contrast of biological samples.

Vacuum Generators (VGs), established to meet the demand of ultrahigh vacuum-based technologies, already started building low-energy electron diffraction (LEED) systems, Auger electron spectrometer systems, and X-ray photoelectron spectrometer (XPS) systems in the late 1960s and early 1970s. Since VG specialized in ultrahigh vacuum (UHV) chambers and had developed stable field-emission sources for commercial instruments (Lilburne et al., 1970), it was a natural fit for VG to move forward producing high-voltage and high-resolution UHV-based STEMs. VG established a microscope division by 1972 to produce commercial STEMs (Wardell & Bovey, 2009). The VG research team optimized all the relevant components of a dedicated commercial STEM (e.g., strongly excited asymmetrical objective lens, top entry specimen stage and cartridge, and so on). The design strategy for the objective lens followed Cowley's reciprocity principle between TEM and STEM (Cowley, 1969). The VG researchers especially emphasized the huge potential of incorporating analytical systems and post-specimen lens systems to the main microscope column and therefore decided to put the cold FEG at the bottom of the microscope column. By 1974, VG already delivered two dedicated STEMs (codenamed as HB5 of which HB refers to high-brightness electron gun) that could operate at 100 kV with a specified image resolution of ∼0.5 nm and these dedicated STEMS could resolve the 0.34 nm lattice fringes of graphite in the BF STEM imaging mode (Wardell et al., 1973; Wardell & Bovey, 2009). By working together with the STEM users, VG continuously improved the performance of the HB5 STEM, soon obtaining 0.144 nm Au lattice fringes. The later versions of the HB5 incorporated a windowless X-ray detector, a virtual objective aperture, an improved electron energy-loss spectrometer, a diffraction pattern observation screen, and so on (Wardell & Bovey, 2009). By integrating many of the progressive improvements that were practiced on the HB5 STEMs, VG introduced in 1981 a new model HB501 as a high-performance analytical electron microscope. In the late 1980s, the demand for atomic-resolution imaging expedited the development of the 100-kV HB501UX with a stronger objective lens, reaching an image resolution of ∼0.22 nm in the ADF imaging mode. The VG HB601, commercialized in the 1990s, incorporated all the available digital systems and new detector technologies.

VG also produced specialized STEM instruments including the Microscope for Imaging, Diffraction and Analysis of Surfaces (MIDAS) at Arizona State University (Fig. 4) (Venables et al., 1987; von Harrach, 2009). The MIDAS was a fully integrated UHV system including the microscope column, the sample preparation and transfer systems, the optical spectroscopy characterization systems, and gas exposure chambers. One of the unique designs of MIDAS involved the insertion of "parallelizer" coils in the objective lens bores, both before and after the specimen position (Kruit & Venables, 1988). The use of the "through-the-lens" design significantly increased the detection efficiency of Auger and secondary electrons. The MIDAS design increased the resolution of Auger electron imaging from tens of nanometers to below 1 nm. Such a surface and elemental sensitive imaging technique was applied to investigations of industrial bimetallic catalysts, with an expectation of extracting information about the effects of catalyst surface segregation on heterogeneous catalysis. For studies of *in situ* deposited Ag nanoclusters, detection of <10 Ag atoms by Auger analysis was accomplished (Liu et al., 1992, 1993*a*). Based on the design and construction of the MIDAS, VG started designing and constructing 300-kV STEMs (von Harrach, 2009), denoted as HB603, with excellent analytical capabilities (Lyman et al., 1994; von Harrach, 1994; Watanabe & Williams, 1999). The VG HB603 U was developed for ultrahigh image resolution (von Harrach et al., 1993; von Harrach, 1994). Unfortunately, the VG Microscopes Ltd. stopped operation in May 1996, just a few years prior to the broad acceptance of the power of STEMs by scientific research communities.

The sudden stop of the production of dedicated STEMs by VG Microscopes shocked the elite community who relied on VG dedicated STEMs to conduct their research. Nigel Browning of the University of Illinois–Chicago, who had planned to purchase a VG dedicated STEM for his research programs, could not find a supplier of dedicated STEMs. Although FEG TEMs were readily available from electron microscope vendors, there were no reports, however, on achieving atomic-resolution ADF STEM images on such FEG TEMs. By working with the JEOL company to slightly modify an FEG JEOL 2010F (200 kV) to produce a small electron probe and to collect electrons scattered to high angles, Browning and colleagues (James et al., 1998) were able to demonstrate a sub-2 Å resolution in high-angle ADF (HAADF) images. These impressive results manifested that a commercial FEG TEM could be operated as an STEM and could provide atomic-resolution STEM images comparable to those that achieved at 300 kV on the VG HB603 U dedicated STEM. In a subsequent paper, James & Browning (1999) conducted a full investigation on how to obtain small electron probes for STEM imaging on a high-performance FEG TEM. They further demonstrated that all the capabilities achievable on a dedicated STEM could be accomplished on an FEG TEM except that with a Schottky-emission electron gun, the energy resolution of the acquired EELS spectra was not as good as that obtained on a cold FEG dedicated STEM. The demonstration of achieving atomic-resolution STEM imaging on a conventional 200-kV FEG TEM with a Schottky-emission electron gun had important implications and, to a large degree, accelerated the adoption of atomic-resolution STEM imaging and the associated

Downloaded from https://www.cambridge.org/core. IP address: 68.98.49.119, on 04 Sep 2021 at 06:14:57, subject to the Cambridge Core terms of use, available at https://www.cambridge.org/core/terms. https://doi.org/10.1017/S1431927621012125

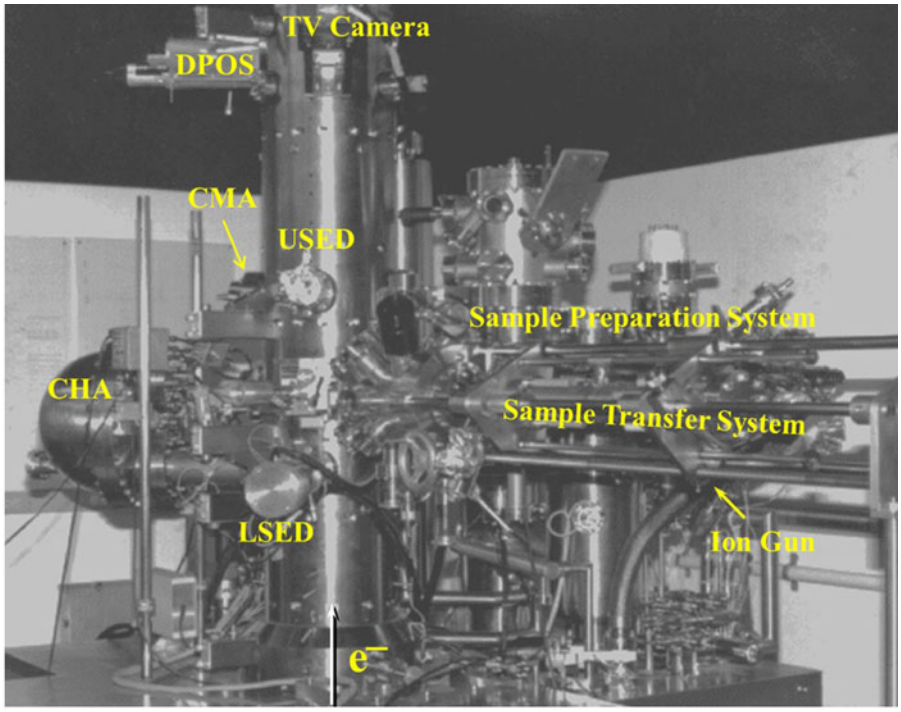

Fig. 4. Arizona State University's MIDAS (Microscope for Imaging, Diffraction and Analysis of Surfaces).

techniques by broad scientific research communities. The quick acceptance of atomic-resolution Z-contrast imaging on FEG TEMs, the significant reduction of instabilities due to microscope and/or environmental factors, and the realization of aberration-correction to form sub-Å electron probes all expedited the broad applications of atomic-resolution STEM in solving challenging materials problems.

The Era of Aberration-Corrected STEM

Unlike light microscopes, electron microscopes suffer from the unavoidable, positive spherical aberration of rotationally symmetric electron lenses regardless of skillful lens design and perfect fabrication (Scherzer, 1936). Scherzer pointed out that by considering alternative approaches, drastically different from axially symmetric round lenses, it would be possible to correct electron lens aberrations (Scherzer, 1947). Tremendous efforts were devoted to searching designs of lens and aberration correctors that would provide controllable and/or diminishing aberrations (Hawkes, 1980, 2009*a*, 2009*b*, 2015; Rose, 2009; Marko & Rose, 2010; Septier, 2017). Soon after the FEG STEM was in operation, Crewe and colleagues started designing and developing aberration correctors with the goal of drastically reducing the effects of lens aberrations on limiting the STEM probe size (Crewe et al., 1968*a*; Beck & Crewe, 1974; Beck, 1979; Crewe, 1980, 1982, 1983*a*, 1983*b*, 1995, 2009; Crewe & Jiye, 1985; Figs. 3d, 3e). Shao (1988) published a paper discussing the mechanisms of the generation of fifth-order aberrations in a sextupole-corrected electron optical system and proposed a new approach to compensating the rotationally symmetric part of fifth-order aberrations. Numerical simulations implied that by using an additional round lens, the electron probe radius could be reduced from 0.08 to about 0.04 nm for 200 keV electrons, achieving sub-Ångstrom resolution. On the experimental front, however, the progress was much more sluggish and frustrating. Crewe and colleagues tested the quadrupole/octupole corrector, introduced the concept of sextupole corrector, and other optical elements. Even with their tremendous effects (>30 years), however, they did not succeed in demonstrating practical resolution improvement (Crewe, 2004). In retrospect, many of the required tools for successfully diagnosing and auto-tuning the lens aberrations had not been developed. In addition to innovative optical designs, faster computers, robust testing algorithms, high-quality electronic devices, and high-precision lens fabrication skills are all required for the successful development of practical aberration correctors. Furthermore, as the STEM probe size became smaller and smaller stringent requirements for microscope and environment stability might have imposed another limiting factor on achieving sub-Å resolution imaging.

Zach and Haider (1994, 1995*a*, 1995*b*), based on a new design of a high-resolution low-voltage scanning electron microscope (Zach, 1989), developed the first workable multipole corrector and clearly demonstrated resolution improvement, even for low-energy electron beams. By using a quadrupole/octupole corrector, they reduced both the spherical and chromatic aberration, allowing for a theoretical resolution limit of ~1 nm at electron-beam energies between 0.5 and 1 keV. They experimentally obtained an image resolution <2 nm at 1 keV. Haider et al. (1995), based on Rose's solution for spherical aberration-correction (Rose, 1990), utilized two electromagnetic hexapoles and four additional lenses to construct a hexapole-corrector for a 200 kV TEM and experimentally demonstrated resolution improvement over the non-aberration-corrected TEM (Haider et al., 1997, 1998). These astonishing achievements firmly established the practicality of incorporating aberration correctors into TEMs to significantly improve image resolution.

In a parallel development, Krivanek and colleagues constructed a quadrupole/octopole corrector equipped with computer control which could make numerous adjustments rapidly and systematically. They incorporated this corrector into a dedicated STEM

Downloaded from https://www.cambridge.org/core. IP address: 68.98.49.119, on 04 Sep 2021 at 06:14:57, subject to the Cambridge Core terms of use, available at https://www.cambridge.org/core/terms. https://doi.org/10.1017/S1431927621012125

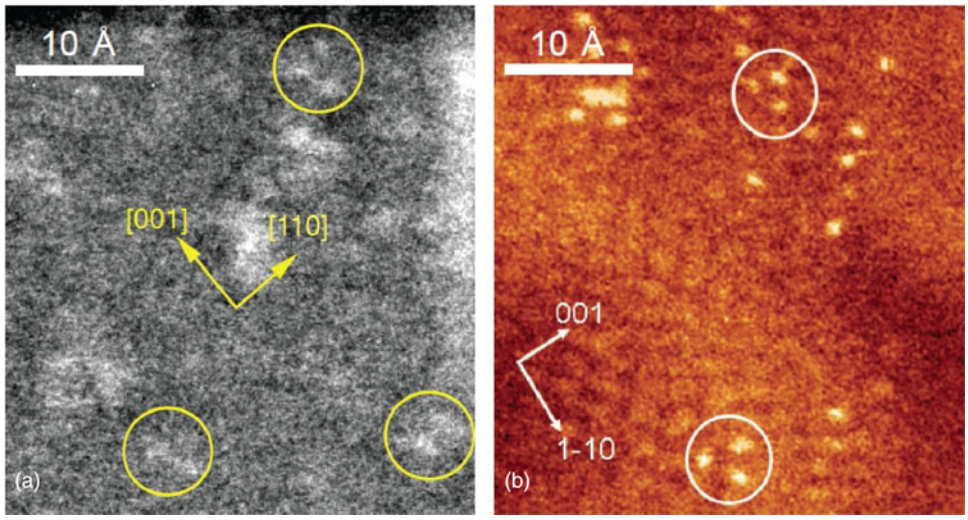

Fig. 5. Imaging of Pt atoms on γ-alumina with a VG Microscopes HB603 U 300 kV STEM (**a**) before and (**b**) after aberration-correction. Some Pt trimers and dimers are just visible in (**a**) but individual atoms and clusters are much clearly visualized in (**b**). Reproduced from Pennycook (2017).

instrument and were able to produce smaller electron probes by increasing the size of the illumination aperture which also allowed more electrons passing through the lens (Krivanek et al., 1997*a*, 1997*b*). In their subsequent work, Krivanek et al. (1998) showed a Ronchigram with the radius of the flat phase disk extending to ~15 mrad which was ~2× larger than that of the uncorrected STEM instrument, unambiguously demonstrating the correction of spherical aberration to produce smaller probe sizes. The BF STEM images showed a reduced delocalization effect as well. Krivanek et al. (1999) presented the design of a second-generation quadrupole–octupole C_S corrector to compensate high-order parasitic aberrations and predicted that sub-Ångstrom electron probes should be achievable at 100 kV when system instabilities were significantly reduced. In this new design, the fifth-order geometrical aberrations of the combination of corrector and probe-forming lens were expected to be eliminated. By 2001, impressive experimental results were obtained at 100 kV with an image resolution of ~123 pm in ADF STEM images (Dellby et al., 2001). By 2002, Batson et al. (2002), by integrating a second-generation STEM corrector to an old VG HB501 STEM (120 kV), obtained impressive ADF images of gold atoms with a measured width of ~80 pm. This result unambiguously demonstrated the power of aberration-corrected STEM and its huge potential for materials characterization at sub-Ångstrom level with low-energy electrons. Krivanek's STEM corrector demonstrated an image resolution of 78 pm at 300 kV, clearly resolving the close-packed Si_{444} atomic spacing with the electron beam along the Si [112] zone axis (Nellist et al., 2004).

Haider et al. (2000) discussed the upper limits for the residual aberrations to form desired probe sizes and provided guidance on selecting appropriate parameters that control corrector alignment and diagnosis. Krivanek et al. (2003) described a new design of a quadrupole/octupole corrector to correct all fifth-order aberrations while still keeping a small C_C value. They proposed that when such a corrector is coupled to an optimized STEM column, sub-Ångstrom probe sizes would be obtainable at 100 kV and sub-0.5 Å probes would be achievable at higher operating voltages. In addition to reducing the electron probe size, the proposed STEM corrector could increase the total current available in an atom-size probe by a factor of 10 or more. Further refinements in aberration correctors, improvement in illumination source size and coherence, and microscope stability continuously improved the STEM image resolution to 63 pm in 2007 (Sawada et al., 2007), 47 pm in 2009 (Erni et al., 2009; Sawada et al., 2009), ~45 pm in 2015 (Sawada et al., 2015), and 40.5 pm in 2018 (Morishita et al., 2018). Figure 5 shows the comparison of a pair of HAADF-STEM images obtained before and after aberration-correction, demonstrating the power of aberration-corrected STEM in characterizing nanostructured catalysts (Nellist & Pennycook, 1996; Pennycook, 2017). Figure 6 displays a series of images (with an acquisition time of 4 s per frame) obtained sequentially to track the diffusion path of Ce dopant in the w-AlN single crystal (Ishikawa et al., 2014). The Al–N "dumbbells" are clearly resolved and the brighter columns represent the Al sites. The brightest column, indicated by the white arrowhead, contained a single Ce dopant, moving to a different location in each image panel. By detailed image analyses and simulations, the authors deduced that these observations strongly suggested vacancy-, and occasionally, interstitial-mediated diffusion in Ce-doped w-AlN. Although the Ce diffusion was driven by the electron-beam-induced effects, such a method could be applicable for studying diffusion mechanisms in other materials systems with diffusion barriers such that the transition times are comparable to the scan rate of the STEM.

Since electron-beam-induced knock-on damage depends on the primary electron energy, atomic-resolution STEM imaging at low voltages is critical to studying a variety of materials, especially 2D materials or carbon-based materials. After optimizing the conditions of the ac-STEM, Krivanek et al. (2010*a*) were able to obtain impressive ADF STEM images, at 60 kV, of monolayer BN sample with clear contrast differentiation between B and N atoms. These authors further demonstrated that they could differentiate B, C, N, and O atoms that were present in the BN sample (Fig. 1b). This work unambiguously demonstrated the potential of low-voltage atomic-resolution STEM for resolving and identifying atomic species in 2D materials systems. Atom-by-atom structural and chemical analysis of all radiation damage-resistant atoms present in, and on top of, ultrathin sheets became practical (Krivanek et al., 2010*a*, 2010*b*; Sasaki et al., 2010; Dellby et al., 2011; Suenaga et al., 2011).

Another major development was the incorporation of monochromators for ultrahigh energy-resolution EELS. The electron

Downloaded from https://www.cambridge.org/core. IP address: 68.98.49.119, on 04 Sep 2021 at 06:14:57, subject to the Cambridge Core terms of use, available at https://www.cambridge.org/core/terms. https://doi.org/10.1017/S1431927621012125

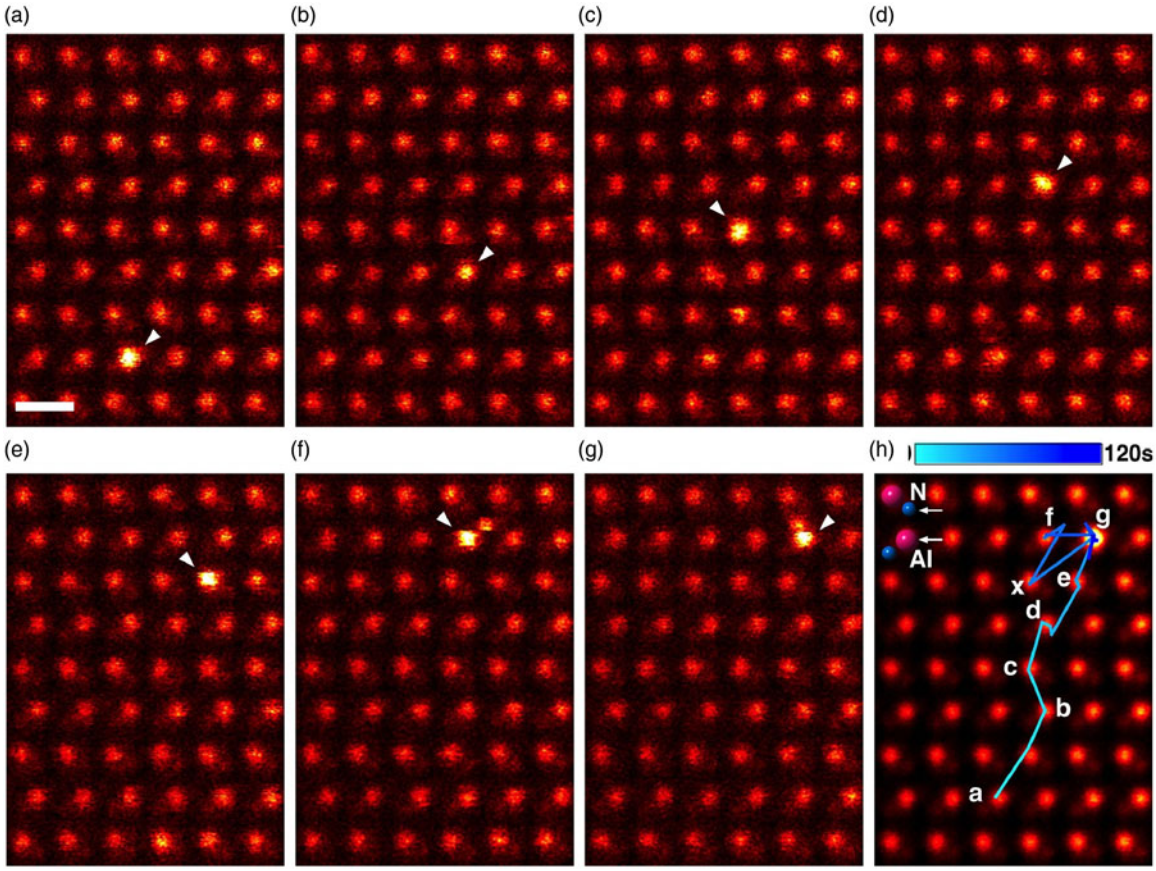

Fig. 6. Selected frames from a sequence of 30 Z-contrast images of a w-AlN single-crystal doped with Ce viewed along the [11–20] zone axis. (**a**–**g**) Frames 1, 4, 5, 6, 10, 16, 20, respectively, show the locations of a single Ce dopant as marked by the arrowhead in each panel. (**h**) Frame-averaged Z-contrast image. The observed Ce trace is overlaid and the Ce positions in each panel (**a**–**g**) are indicated. The scale bar is 3 Å. Reproduced from Ishikawa et al. (2014).

analyzer was incorporated at the very beginning of STEM development to enable chemical analysis capabilities with high spatial resolution (Crewe et al., 1971*b*; Colliex et al., 1976). However, even with a cold FEG the energy resolution (~0.2–0.3 eV) is still too large compared with other broad beam techniques (e.g., Raman or infrared spectroscopy) and consequently vibrational excitations of matter could not be explored at high spatial resolution. The integration of a monochromator (Tsuno, 2011; Kimoto, 2014; Hawkes & Krivanek, 2019) into an STEM instrument (Fig. 2b) drastically improved the energy resolution of STEM-EELS (Krivanek et al., 2009). An energy resolution of 30 meV was demonstrated with an atom-size electron probe, enabling both atomic-resolution STEM imaging and ultrahigh energy-resolution EELS (Krivanek et al., 2013). The full potential of atomic-resolution monochromated STEM was realized and vibrational spectra from different systems with atom-size probes were reported (Krivanek et al., 2014*a*), firmly establishing the practical applications of vibrational spectroscopy on an STEM instrument. Further improvement to an energy resolution of sub-10 meV on the Nion ac-STEM was proposed (Krivanek et al., 2014*b*), and with optimization of electron optical and electronic systems, an energy resolution of ~4 meV was realized (Hachtel et al., 2019; Krivanek et al., 2019). Figure 7 schematically illustrates the configuration of the Nion monochromator and how it is incorporated into an aberration-corrected Nion STEM for ultrahigh energy-resolution experiments. It is anticipated that further improvement in energy resolution to sub-meV may become plausible.

The integration of vibrational spectroscopy into the atomic-resolution STEM opened new opportunities for investigating the properties and functions of matter, and impressive results have already been published (Krivanek et al., 2014*a*; Lagos et al., 2017; Idrobo et al., 2018; Hachtel et al., 2019; Hage et al., 2019; Senga et al., 2019). The possibility of atomic-resolution phonon mapping was proposed (Lugg et al., 2015*a*; Dwyer, 2017; Hage et al., 2019) and practically realized by Venkatraman et al. (2019) (Fig. 8), although the fundamental localization mechanisms and image contrast still need to be carefully evaluated (Hage et al., 2020*b*; Rez & Singh, 2021). Hage et al. (2020*a*) demonstrated the detection of distinctive localized vibrational signatures from a single-atom impurity in a solid (Si atom in graphene), clearly demonstrating single-atom sensitivity by STEM vibrational spectroscopy and inviting intriguing implications across the fields of physics, chemistry, and materials science. It is expected that with further development of novel electron detectors (Plotkin-Swing et al., 2020), atomic-resolution STEM-EELS, including vibrational spectroscopy, will significantly impact many research fields such as energy, nanoscience, and quantum science.

The Development of STEM Imaging Theory

The Reciprocity Principle

When a crystalline specimen was examined, STEM images revealed diffraction effects such as Fresnel fringes, phase-contrast

Downloaded from https://www.cambridge.org/core. IP address: 68.98.49.119, on 04 Sep 2021 at 06:14:57, subject to the Cambridge Core terms of use, available at https://www.cambridge.org/core/terms. https://doi.org/10.1017/S1431927621012125

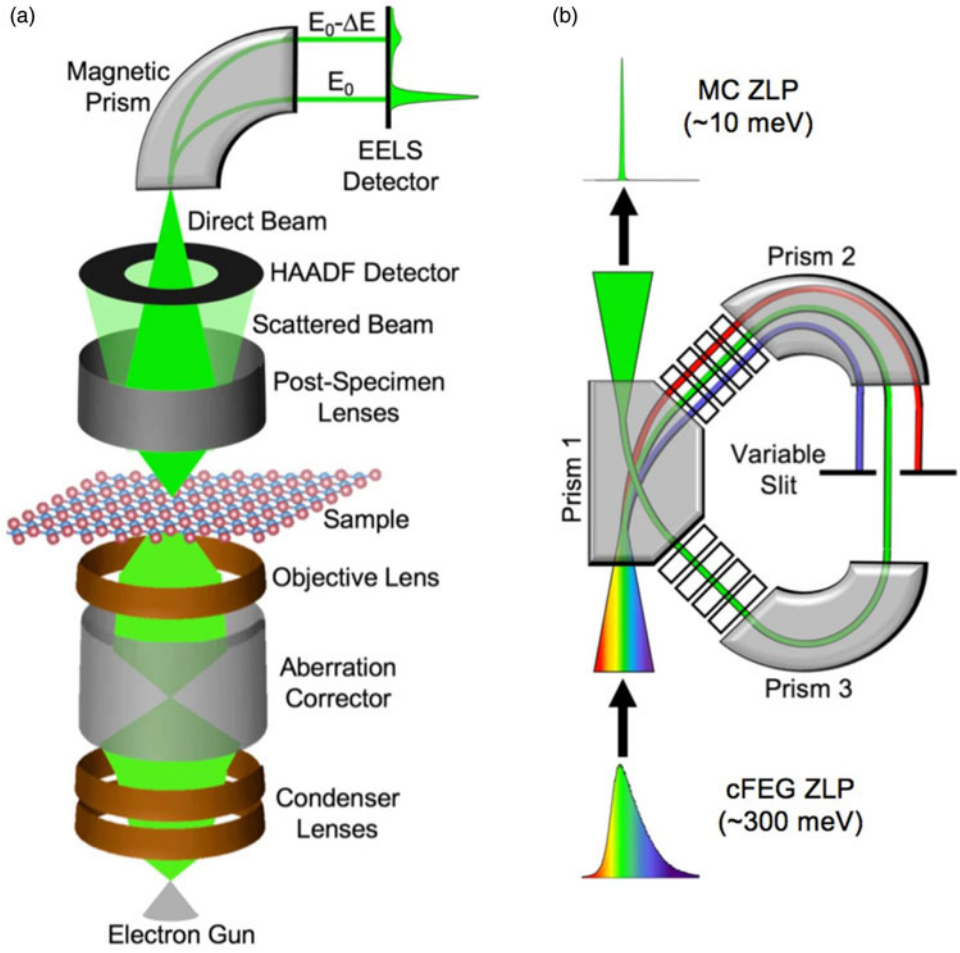

Fig. 7. Electron energy-loss spectroscopy and monochromation. (**a**) Schematic of electron energy-loss spectroscopy (EELS) experiment in a scanning transmission electron microscope (STEM). (**b**) Schematic of monochromation of electron beam (occurring between the electron gun and the condenser lenses). Reproduced from Hachtel et al. (2018).

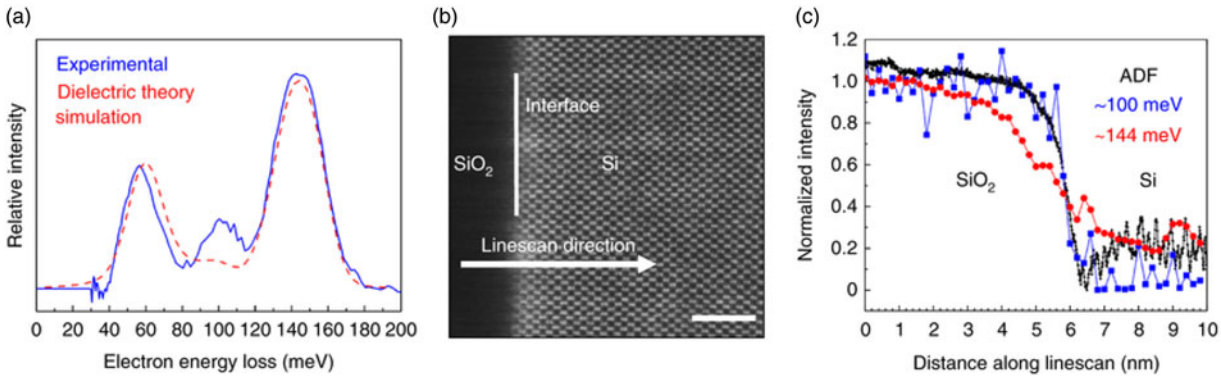

Fig. 8. High-resolution vibrational spectroscopy in SiO_2. (**a**) Experimental energy-loss spectrum in SiO_2 far from the interface (solid blue line) and a dielectric theory simulation of the spectrum (dashed red line). The peak at ~100 meV does not appear strongly in the dielectric simulation, indicating that it is predominantly excited by impact scattering. (**b**) Atomic-resolution ADF image of the SiO_2/Si interface (showing the linescan direction across the interface). Scale bar = 2 nm. (**c**) Normalized signal profiles across the interface-100 meV (blue) and 144 meV (red)—overlaid on the contrast-reversed ADF signal profile. The 100 meV signal traces the ADF signal profile, thereby demonstrating high spatial resolution. Reproduced from Venkatraman et al. (2019).

effects, and lattice fringes, which represented common features of conventional TEM images (Cowley & Strojnik, 1968, 1969; Crewe et al., 1968*c*; Cowley, 1969). To understand such STEM image contrast, Cowley (1969) invoked the reciprocity principle, which had been previously discussed to link electron diffraction and imaging in conventional TEM (Pogany & Turner, 1968), to explain the diffraction and phase contrast in STEM images. By applying the reciprocity principle, Cowley concluded that "the

Downloaded from https://www.cambridge.org/core. IP address: 68.98.49.119, on 04 Sep 2021 at 06:14:57, subject to the Cambridge Core terms of use, available at https://www.cambridge.org/core/terms. https://doi.org/10.1017/S1431927621012125

image contrast of the STEM may be interpreted by direct analogy with the CTEM (conventional TEM) and the whole associated body of imaging theory will apply, the only variations being those depending on the geometry and special features of individual instruments." Based on the symmetry of the Green's function formulation (Pogany & Turner, 1968), the reciprocity principle applies to multiple scattering events as well. Pogany and Turner stated that an approximate reciprocity relationship also held for inelastically scattered electrons provided that the change in energy and wave vector would be small enough. Further discussions on the reciprocity principle and its relationship to contrasts in STEM images can be found in papers published by Zeitler & Thomson (1970*a*, 1970*b*).

In practice, the electron sources and detectors are not point objects but possess finite sizes which introduce the equivalence of coherent conditions in the corresponding configurations of CTEM and STEM, respectively. Since there are no imaging lenses, in an STEM, after the specimen the displayed pixel intensity of an STEM image should be proportional to the total number of electrons that are collected by the specific STEM detector. Therefore, the total signal strength collected by an STEM detector is the summation of the electron intensity (not wavefunction amplitude!) over all the detector pixels: The size, shape, and the position of the STEM detector with respect to the optical axis of the incident electron beam become critically important for interpreting the observed image contrast. If an STEM disk detector is positioned at the optical axis and subtends a convergent semi-angle α at the specimen then, by reciprocity, the equivalent TEM image should be formed with a condenser aperture that subtends the same convergent semi-angle α at the specimen, but this aperture should be incoherently illuminated. Therefore, BF STEM images obtained with larger detector sizes should have reduced phase contrast, analogy to the CTEM phase-contrast images obtained with large condenser apertures and incoherent illuminations. On the other hand, parallel illumination in the TEM generates coherently diffracted beams at the exit surface of the specimen. The equivalent condition for STEM imaging requires electron coherence across the hole of the STEM probe-forming aperture and the use of an infinitely small BF detector. The small size, cold FEGs satisfy the coherent requirement, resulting in small electron probes at the specimen provided that the effects of spherical and chromatic aberrations on the probe size are minimized. From this perspective, one can control the degree of phase contrast in BF STEM images by manipulating the effective size of the BF STEM detector.

Imaging Heavy Metal Atoms on Ultrathin Amorphous Films by the ADF Detector

The demonstration of ADF STEM imaging of isolated heavy atoms by Crewe and colleagues clearly attracted attention from the electron microscopy community and broader scientific research communities. From an electron scattering perspective, the bright contrast of heavy atoms supported on thin carbon films or decorating biological molecules seems intuitively understandable: the light-element thin support film does not scatter many of the incident electrons into the ADF detector while heavy atoms do. By collecting all the electrons scattered out of the incident electron illumination cone, high-quality atomic-resolution images enabled studies of diffusion processes of heavy atoms (Isaacson et al., 1977). The direct visualization of diffusion of individual uranium atoms adsorbed onto a thin carbon film was thus realized. After careful evaluation of electron-beam-induced effects, the authors concluded that the observed motion of metal atoms was not caused by the impinging high-energy electrons. Since the primary electron-beam energies that were used to image supported metal atoms were relatively low, the knock-on damage, by the primary electrons, on both the carbon films and the metal atoms was most probably suppressed. However, other types of electron-beam-induced effects could not be completely ruled out, especially when the heavy metal atoms were not strongly anchored onto the support films.

The image contrast of supported metal atoms was evaluated by theoretical calculations and the results were compared to experimental data (Langmore et al., 1973; Retsky, 1974; Wall et al., 1974*a*, 1974*b*; Beck & Crewe, 1975; Crewe, 1979, 1983*a*). These calculations illustrated the effects of electron probe size and atom size on the observed image resolution and intensities. Retsky's results clearly revealed quantization of the observed image intensities corresponding to one or two uranium atoms, suggesting that the experimentally acquired ADF images might represent incoherent imaging. With detailed analyses of image intensity profiles, differentiation of isolated Pt atoms from Pd atoms was also accomplished by collecting all the scattered electrons (Isaacson et al., 1979). In these early studies, most of the substrates were amorphous films and the metals were either single atoms or small clusters. Electron diffraction and channeling effects, which are usually present in STEM images of crystalline substrates or larger metal particles, did not play a dominant role, enabling a clear identification of single metal atoms with high image contrast. With this type of ideal samples, even though the inner collection angle of the ADF detector was small, the contrast of heavy atoms in ADF STEM images was intuitively interpretable. Although imaging of isolated metal atoms, and even their dynamic movement, were accomplished on these early atomic-resolution STEM instruments, practical applications of these atomic-resolution imaging methods to characterizing practical materials, frequently polycrystalline in nature and relatively thick, were not realized until much later.

Atomic Number (Z) and Phase-Contrast STEM Imaging

The Need for Reliably Identifying Supported Metal Clusters and Particles

The STEM images obtained by collecting all electrons scattered out of the primary electron illumination cone with a low-angle ADF detector demonstrated atomic number (Z)-dependent contrast for heavy metal atoms and clusters supported on thin carbon films (Crewe et al., 1970, 1975). Dividing the ADF signal by the simultaneously acquired signal of inelastically scattered electrons was expected to yield an interpretable Z-contrast image without the complications arising from variations in sample thicknesses. When Treacy et al. (1978) used this method to characterize supported Pt and Pd catalysts, they discovered that strong diffraction contrasts, arising from Bragg reflections in the crystalline component phases of the sample, dominated both the EELS and the ADF signals, masking the expected Z-dependence image contrast of metal clusters and nanoparticles. These authors realized that by increasing the inner collection angle of the ADF detector >0.25/nm (~100 mrad for 100 keV electrons), the Z-dependence contrast of the noble metal nanoclusters with sizes as small as 0.5 nm was recovered. Howie (1979) immediately pointed out that at such high angles of scattered electrons, thermal diffuse scattering could be more prominent than the coherent Bragg

Downloaded from https://www.cambridge.org/core. IP address: 68.98.49.119, on 04 Sep 2021 at 06:14:57, subject to the Cambridge Core terms of use, available at https://www.cambridge.org/core/terms. https://doi.org/10.1017/S1431927621012125

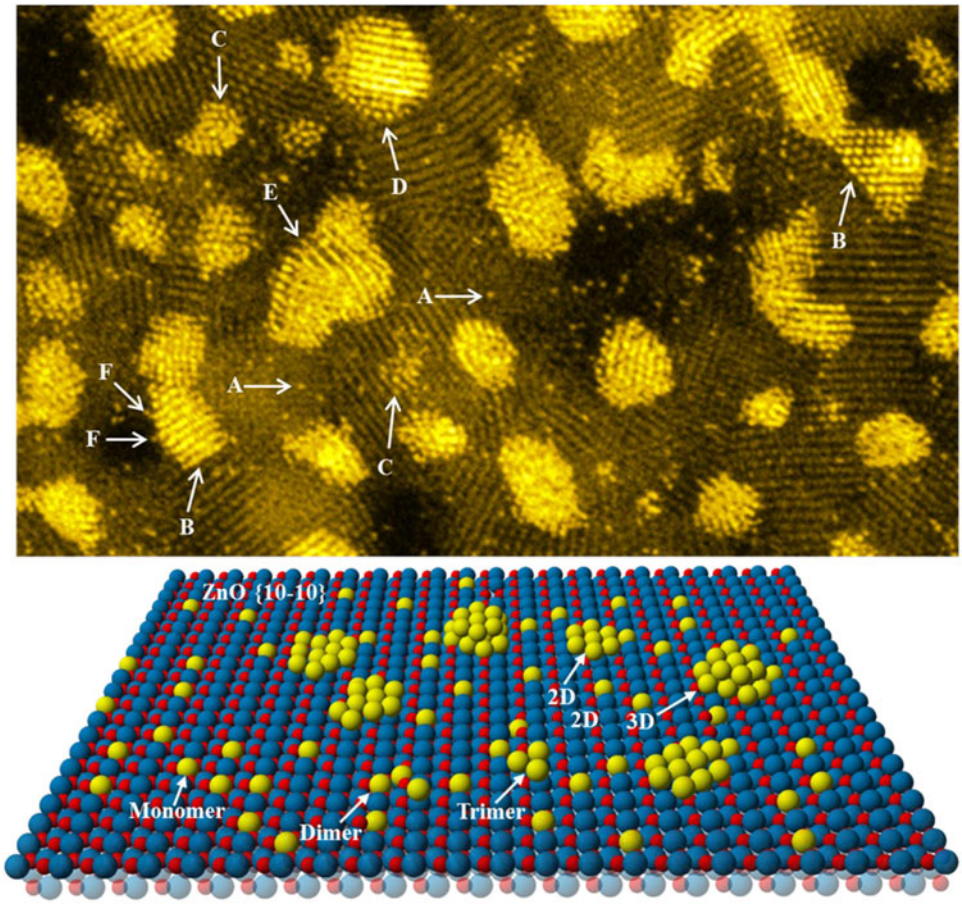

Fig. 9. Top panel: Aberration-corrected HAADF-STEM image of a Pt/ZnO catalyst shows the presence of Pt single atoms (A), faceted Pt clusters (B), highly disordered Pt subnanometer clusters (C), reconstructed surface atoms of Pt nanoparticles (D), strained lattices of Pt (E), and highly unsaturated Pt atoms attached to the Pt nanocrystal (F). Bottom panel: Schematic illustration of the various types of metal clusters, trimers, dimers, and monomers dispersed onto the ZnO {10–10} surface. Reproduced from Liu (2017b).

scattering. Furthermore, electron-channeling effects could still persist since even backscattered electrons had demonstrated channeling effects (Coates, 1967; Howie et al., 1971; Spencer et al., 1972). Based on Howie's proposal, Treacy et al. (1980) and Treacy (1982) demonstrated the power of HAADF imaging of supported metal catalysts, especially small metal clusters that could not be easily detected by TEM or other types of STEM imaging modes. The use of the HAADF imaging method has become a standard tool for characterizing supported metal catalysts, especially small noble metal clusters, atomically dispersed metals, and even isolated individual metal atoms on practical catalyst supports (Treacy & Rice, 1989; Liu & Cowley, 1990; Rice et al., 1990; Bradley et al., 1994, 2012; Nellist & Pennycook, 1996; Liu, 2004, 2005, 2011; Qiao et al., 2011; Liu, 2017*a*, 2017*b*). Figure 9 shows an atomic-resolution HAADF-STEM image of a supported Pt catalyst, clearly revealing Pt monomers, dimers, multimers, clusters, and nanoparticles. The surface disorder and faceting of metal clusters and small metal particles are revealed with sub-Ångstrom image resolution.

Bright-Field and Annular Dark-Field STEM Imaging

In addition to his work on understanding the contrast mechanisms of high-resolution TEM images of thin crystals (Cowley & Iijima, 1972), Cowley was extremely interested in understanding the contrast of high-resolution STEM images (Cowley, 1973*a*, 1973*b*, 1975, 1976; Cowley et al., 1974), especially with respect to the nature of dark-field imaging in STEM. Spence & Cowley (1978) pointed out that the contrast in STEM lattice images originated from the coherent interference between overlapping CBED discs at the STEM detector position. They also concluded that the intensity at the middle point of the overlapping disks was independent of the beam defocus and aberrations of the probe-forming lens, implying the potential of constructing special detectors for efficient STEM imaging with significantly improved resolution. Enlarging the size of the STEM detector, reduces such interference effects as well as the fringe visibility. Such an understanding of phase-contrast STEM imaging had important consequences on designing special optical systems to be attached to the VG HB5 that ASU installed in 1978 (Cowley & Au, 1978). With the heavily modified HB5 STEM, Cowley quickly developed shadow-image-based methods for STEM alignment and adjustment (Cowley, 1979*a*) and explored the readily available imaging modes and microdiffraction from regions as small as the STEM probe size (Cowley & Spence, 1979). Figure 10 schematically illustrates the detection configuration that Cowley used for his STEM work. With the use of a cold FEG, Cowley observed coherent interference effects within CBED disks and shadow images (Cowley, 1979*b*).

Although Cowley evaluated the ADF STEM imaging mode on his high-resolution HB5 and believed that the wide-angle ADF

Downloaded from https://www.cambridge.org/core. IP address: 68.98.49.119, on 04 Sep 2021 at 06:14:57, subject to the Cambridge Core terms of use, available at https://www.cambridge.org/core/terms. https://doi.org/10.1017/S1431927621012125

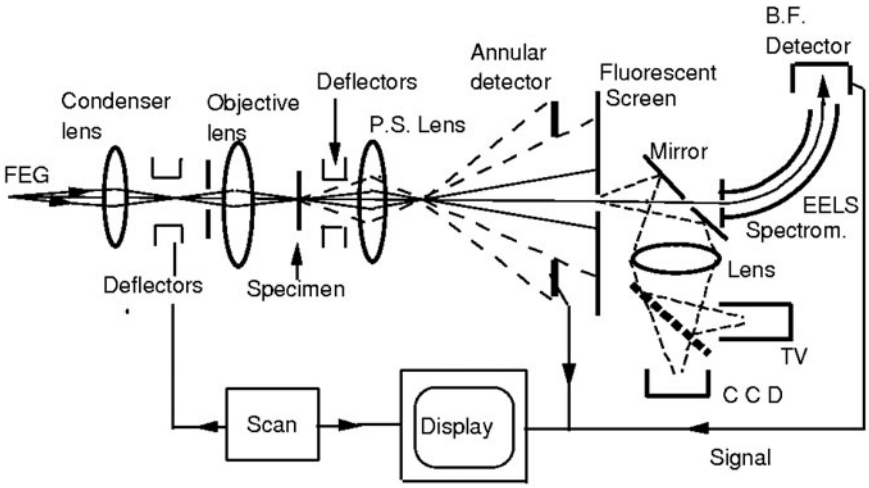

Fig. 10. Diagram of an STEM instrument, modified for the convenient display and recording of shadow images and nanodiffraction patterns. A condenser lens and an objective lens produce the incident electron probe on the specimen and one (or more) post-specimen (P.S.) lenses govern the display of the diffraction pattern on a transmission phosphor screen which may be viewed using a TV-VCR system or a CCD camera with digital recording. The optical lens system can be manipulated by various types of masks. Courtesy of Professor John M. Cowley.

imaging configuration would provide higher image resolution than the BF STEM imaging mode (Cowley, 1984*a*, 1984*b*, 1984*c*), his research group did not aggressively pursue this direction. Instead, they focused on exploring microdiffraction, in-line holograms, and studies of surfaces (Cowley, 1979*b*, 1979*c*, 1979*d*, 1981*a*, 1981*b*, 1982, 1983, 1984*a*, 1984*b*, 1984*c*, 1986; Cowley & Walker, 1981; Lin & Cowley, 1986*a*, 1986*b*). By 1984, the present author joined Cowley's research group and started working on Cowley's heavily modified high-resolution VG HB5 (equipped with a special high-resolution pole piece with a spherical aberration coefficient of ~0.8 mm). The optical systems attached to the top of the HB5 column (Fig. 11) facilitated simultaneous observation of an ADF STEM image, energy-filtered image, and a microdiffraction pattern either in the stationary mode or in the scan mode at 10 Mx. Since the optical systems were outside of the electron microscope vacuum chamber, they could be conveniently modified for assessing the effects of various types of STEM detector configurations on the corresponding STEM image contrast. Differences in image contrast were demonstrated by placing either a penny (low-angle ADF) or a quarter (high-angle ADF) coin to block the central portion of the diffraction pattern which could also be contracted or expanded by varying the settings of the two post-specimen lenses. To reduce the effects of light reflection from the metal coin on the ADF image contrast, the present author fabricated a set of disks, from a light-adsorbing black cardboard, of various sizes and shapes as "high-quality" masks to produce a variety of configured STEM images. Since the black cardboard adsorbed light much better than the shiny coins, the atomic number contrast in the ADF STEM images was observably improved. Square and triangular masks were explored. However, the interpretation of images from such exotic STEM detectors became dubious. In retrospect, the lack of high-sensitivity electron detectors, faster computers, image acquisition and processing algorithms, and environmental stability significantly retarded the development of atomic-resolution STEM imaging. The lack of perceived applications of *Z*-contrast imaging played another important role in not focusing on exploring the capabilities of HAADF imaging mode until projects on characterizing quantum wells (Liu, 1990), supported metal catalysts (Liu et al., 1990), and mineralogical Franckeite ($Pb_5Sn_3Sb_2S_{14}$) structures (Wang et al., 1990, 1995) were started.

The installation of the VG Microscopes HB501UX high-resolution STEM at Oak Ridge National Laboratory in 1988 made it possible for Pennycook and Boatner to obtain chemically sensitive atomic-resolution images of heavy-atom planes in superconductors ($YBa_2Cu_3O_{7-x}$ and $ErBa_2Cu_3O_{7-x}$), directly resolving columns of atoms with different atomic number *Z* (Pennycook & Boatner, 1988; Pennycook, 1989*a*). Their subsequent work on semiconductor interfaces unambiguously demonstrated the atomic number sensitivity of HAADF imaging of crystalline materials and the advantages of this imaging mode over phase-contrast high-resolution TEM (HRTEM) (Pennycook, 1989*b*). Unlike phase-contrast HRTEM imaging, the *Z*-contrast atomic-resolution STEM images did not show obvious contrast reversals with either sample thickness or lens defocus, demonstrating characteristics of incoherent imaging. Previously, multislice simulations of ADF imaging of thin silicon crystal-supported Pt and Au atoms (Kirkland et al., 1987; Loane et al., 1988) showed that the image contrast would be oscillatory, probably due to the fact that the inner angle of the ADF detector was not large enough. These image simulations, however, predicted that silicon lattice spacings would be visible and no contrast reversal with increasing sample thickness would be observed, reflecting characteristics of incoherent imaging even when diffracted Bragg peaks were included in the ADF detector. With the use of a slightly larger objective aperture, better image resolution than that of the optimum Scherzer resolution (Scherzer, 1949) was obtained (Shin et al., 1989; Xu et al., 1990). It should be realized that the STEM image resolution, especially for ADF imaging, is not well-defined since the STEM probe intensity distribution can be manipulated by varying the size of the probe-forming aperture and the defocus value. If the signal strength is strong enough, sharp-peaked electron probes can provide higher image resolution in ADF/HAADF-STEM images.

To understand the observed characteristics of atomic-resolution HAADF images of crystalline specimens, Pennycook and Jessen conducted Bloch wave analysis, which had been used to understand the thickness-dependent contrast in phase-contrast HRTEM

Downloaded from https://www.cambridge.org/core. IP address: 68.98.49.119, on 04 Sep 2021 at 06:14:57, subject to the Cambridge Core terms of use, available at https://www.cambridge.org/core/terms. https://doi.org/10.1017/S1431927621012125

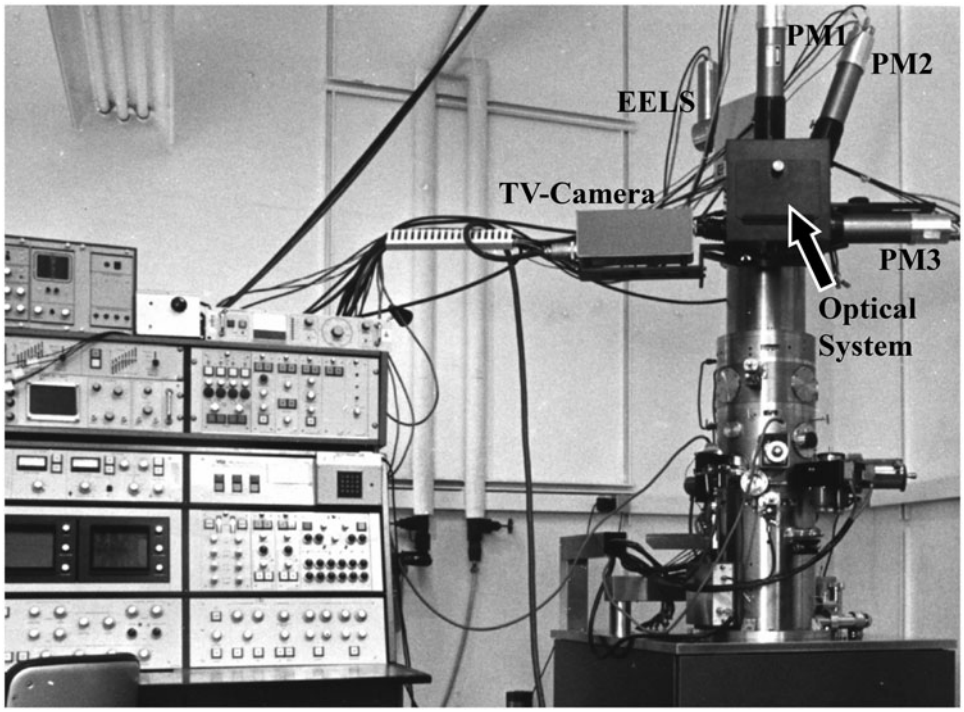

Fig. 11. The heavily modified VG HB-5 STEM of which Professor John M. Cowley used at Arizona State University for all his experimental research work. The black box (indicated by the arrow) contained the unique optical system that transfers the light to various photomultipliers (PM) and the low-light sensitivity TV camera. The annular dark-field images were formed by positioning a light-absorbing mask in the center of the optical lens system. Other types of configured STEM detectors were also tried by masking the various parts of the diffraction pattern displayed on the optical system inside the black box.

images (Kambe, 1982), of primary electrons propagating through a crystal (Pennycook & Jesson, 1990). The key outcome of this analysis provided a picture that high-angle Rutherford scattering of the incident high-energy electrons was primarily produced by the 1*s* Bloch state, tightly bound to the atomic nuclei. Therefore, interference effects (among different Bloch states) are significantly reduced. The collected HAADF signal strength was an additive integration through the specimen thickness, increasing monotonically with sample thickness, modulated by small oscillations due to residue interferences among the Bloch states. For very thin samples and under nonchanneling conditions, the HAADF intensity might increase linearly with sample thickness. Because of the highly localized nature of high-angle scattered electrons interference effects, commonly observed in phase-contrast HRTEM images, at interfaces, surfaces, or crystal defects would be minimal or not observable in HAADF-STEM images. Dynamical diffraction and electron-channeling effects would persist for a thicker crystalline specimen, modifying the thickness-dependent trend of the high-angle scattered electrons. The Bloch wave analyses (Pennycook & Jesson, 1990, 1991, 1992) provided an intuitive understanding of the experimentally observed imaging characteristics of atomic-resolution HAADF images of various types of crystalline materials (Chisholm & Pennycook, 1991; Norton et al., 1991; Pennycook et al., 1991, 1992; Jesson et al., 1993*a*, 1993*b*). It should be pointed out that the degree of interference effects in ADF images strongly depends on the inner collection angle of the annular detector, ranging from complete coherent interference (hole in a disk detector), to partial coherent imaging (annular ring detector), and to completely incoherent imaging (very large inner angle ADF detector or backscattered electron detector).

For STEM imaging, the detector plane contains all the (elastically and inelastically) scattered and nonscattered electrons. At large angles, the electrons scattered by specimen phonons (thermal diffuse scattering) may become dominant (especially for thick specimens, at high temperatures, at surfaces/interfaces, or at various types of defects) while the intensities of Bragg diffraction peaks drop. Phonon-scattered electrons lose a small amount of energy, but the (lateral) momentum transfer can be large, resulting in high-angle scattering events (Hall, 1965; Hall & Hirsch, 1965; Cowley & Pogany, 1968; Earney, 1971; Rez et al., 1977). To evaluate the effects of phonon scattering on the contrast of HAADF images of single crystals and semiconductor interfaces, Wang & Cowley (1989, 1990) incorporated phonon scattering in their multislice calculations. A "frozen-phonon" model (Hall & Hirsch, 1965), justified on the basis of the semiclassical argument that incident high-energy electrons "feel" an instant atomic configuration of the crystalline specimen, was introduced into multislice calculations to reproduce key features observed in CBED patterns of a crystalline specimen (Loane et al., 1991). Further image simulations with either the frozen-phonon approximation or the Bloch wave approach demonstrated similar results and in agreement with experimental measurements (Loane et al., 1992; Hillyard & Silcox, 1993; Hillyard et al., 1993). These calculations were based on single-phonon scattering processes. Multislice simulations based on a detailed phonon dispersion curve in a crystalline specimen showed that the frozen-phonon approximation was valid for quantitatively understanding the image contrast in ADF images of zone-axis crystals (Muller et al., 2001). However, a system in thermal equilibrium with its environment should not be described by a pure state and a many-body quantum-mechanical model for multiple

Downloaded from https://www.cambridge.org/core. IP address: 68.98.49.119, on 04 Sep 2021 at 06:14:57, subject to the Cambridge Core terms of use, available at https://www.cambridge.org/core/terms. https://doi.org/10.1017/S1431927621012125

scattering of fast electrons due to phonon excitations should be used (Forbes et al., 2010). The results of Forbes et al. suggested that treating phonon excitation as one of the inelastic scattering processes would be a more physically meaningful approach. Recent analyses of phonon-scattered electrons supported the model of quantum excitation of phonons and confirmed that the contrast in ADF STEM images would be determined by inelastic scattering events associated with multiple phonon excitations, not consistent with the frozen-phonon model (Hage et al., 2019).

The resolution of STEM imaging certainly depends on the incident probe size but also on the specific detector configuration. For BF STEM imaging with a small on-axis detector, the image resolution should be similar to that of the corresponding TEM imaging. When the size of the BF STEM detector increases, the image resolution can be improved at the expense of phase contrast. For HAADF-STEM imaging, the incoherent imaging characteristics become dominant. The optimum probe size is determined by the lens properties (e.g., aperture size, aberration coefficients, astigmatism, probe defocus, etc.), the energy of the primary electrons, and the properties of the electron gun. Assuming a coherent point source for a non-aberration-corrected STEM, the optimum defocus value and the optimum aperture size, which defines the optimum semi-convergence angle (α) of the illumination cone at the specimen, are given by $\Delta f = -(\lambda C_S)^{1/2}$ and $\alpha = (4\lambda/C_S)^{1/4}$, respectively (Scherzer, 1949; Crewe, 1983*a*, 1983*b*), where C_S is the spherical aberration coefficient of the probe-forming lens and λ is the wavelength of the incident electron. For incoherent imaging, the image resolution is defined as $\delta = 0.43 {C_S}^{1/4} \lambda^{3/4}$ while for phase-contrast imaging $\delta = 0.63 {C_S}^{1/4} \lambda^{3/4}$ (Scherzer, 1949; Cowley & Iijima, 1972). However, since the electron probe intensity distribution plays an important role in determining the observable features in an incoherent HAADF image, it is plausible to manipulate the probe intensity distribution to gain better image resolution at the expense of image contrast (Liu, 1990; Liu & Cowley, 1993). Loane et al. (1992) predicted that by defocusing the electron beam, it would be possible to achieve an image resolution beyond the Scherzer-focus resolution limit of an uncorrected STEM instrument. Such a practice becomes less relevant with aberration-corrected STEM instruments. By using configured STEM detectors, the STEM image resolution can be further improved (Cowley, 1993) provided that one can correctly interpret the image contrast. The effectiveness of such strategies on extracting useful information about the specimen needs to be re-evaluated on aberration-corrected STEMs.

With continuous improvement in image resolution, especially after lens aberrations were corrected, the measurement of image resolution became a nontrivial problem (O'Keefe, 1992; O'Keefe & Allard, 2004; O'Keefe et al., 2005; Smith, 2008). Furthermore, how to define the resolution in a microscope image needs to be carefully evaluated as well (Rayleigh, 1879; Sparrow, 1916; Black & Linfoot, 1957). Depending on the nature of aberration-corrections of the microscope, the evaluation of conditions for obtaining an optimum STEM probe size required careful consideration (Kirkland, 2011; Sasaki et al., 2012). The optical transfer function of the probe-forming lens, relevant for understanding information transfer of the specific lens system, should be studied in three dimensions (Fig. 12; Jones & Nellist, 2014). For practical measurement of image resolution, not only the lens parameters are important but also the nature of the specimen, the intrinsic properties of the scattered electrons, and the type of the STEM detector that is used to obtain the image all become relevant (Peng et al., 2008). The ultimate information transfer limit in an HAADF-STEM image is controlled by the effective size of the objective aperture provided that external interferences, instabilities, and the signal-to-noise ratio are not the limiting factors. Even for the smallest probe size, which is available on the newest generation ac-STEMs, accurate measurement of the "sizes" of various types of individual atoms needs to be carefully scrutinized and verified since the recorded "sizes" of the bright-dots in HAADF-STEM images originate from the convolution of the probe intensity distribution with the effective "atom sizes" which may depend on detector configuration, robustness of the specimen under electron irradiation, and environmental factors.

Configured Detectors for Versatile STEM Imaging

STEM provides various approaches to extracting information from the specimen of interest. The variable sizes and configurations (via adjustment of post-specimen lenses, use of masks, or digital manipulation) of BF and/or ADF detectors can be employed to form images. Such a flexibility, however, poses a critical question on the interpretability of the acquired STEM images. Each type of signal, generated from the interaction of a coherent electron probe with a specimen, can be collected to form the corresponding image which carries specific information about the specimen. Historically, a critical question arises on the nature of the acquired STEM image: coherent versus incoherent formation of images. Such a distinction is critical to understanding the interpretability of, and the ultimate achievable image resolution in, the acquired STEM image. The secondary (emitted) signals such as X-rays, secondary electrons, Auger electrons, or cathodoluminescence light quanta are considered to be incoherent, although the effects of incident electron channeling in crystalline specimens still play a role in determining the collected signal strength. For high-energy primary electrons transmitted through a thin crystal, however, the situation can become complicated. First, with the use of a cold FEG and an optimum probe-forming aperture, all electrons within a small electron probe can be considered fully coherent. The reciprocity principle suggests that, with the use of a small (ideally a delta function) STEM detector, the acquired STEM image can be fully interpreted as a BF/DF phase-contrast TEM image. This statement is valid regardless of the probe size as long as it is fully coherent. Spence & Cowley (1978) pointed out that unless the small STEM detector was positioned at the overlapping regions of the diffraction disks lattice fringes (due to interference effect) of a crystalline specimen would not be obtained. Such a requirement for overlapping diffraction disks demands an effective minimum convergence angle of the incident probe or the size of the probe-forming aperture, which determines the minimum probe size if the lens aberrations are fully corrected. Lattice fringes with spacings smaller than the probe size can be observed as long as the STEM probe is fully coherent and the diffraction disks overlap (Liu & Cowley, 1991, 1993). In order to understand the image contrast and resolution of STEM images obtained with configured STEM detectors, we provide here a simple qualitative description of STEM imaging (Cowley, 1993; Liu & Cowley, 1993) and relate the critical role of the size and shape of the STEM detectors to the contrast of the corresponding STEM images.

When a small, coherent electron probe interacts with a crystalline specimen in an STEM instrument, the incident electrons are scattered both elastically and inelastically. If the specimen is thin enough, then all the incident electrons can penetrate through the specimen (conservation of the total electron flux). Such an

Downloaded from https://www.cambridge.org/core. IP address: 68.98.49.119, on 04 Sep 2021 at 06:14:57, subject to the Cambridge Core terms of use, available at https://www.cambridge.org/core/terms. https://doi.org/10.1017/S1431927621012125

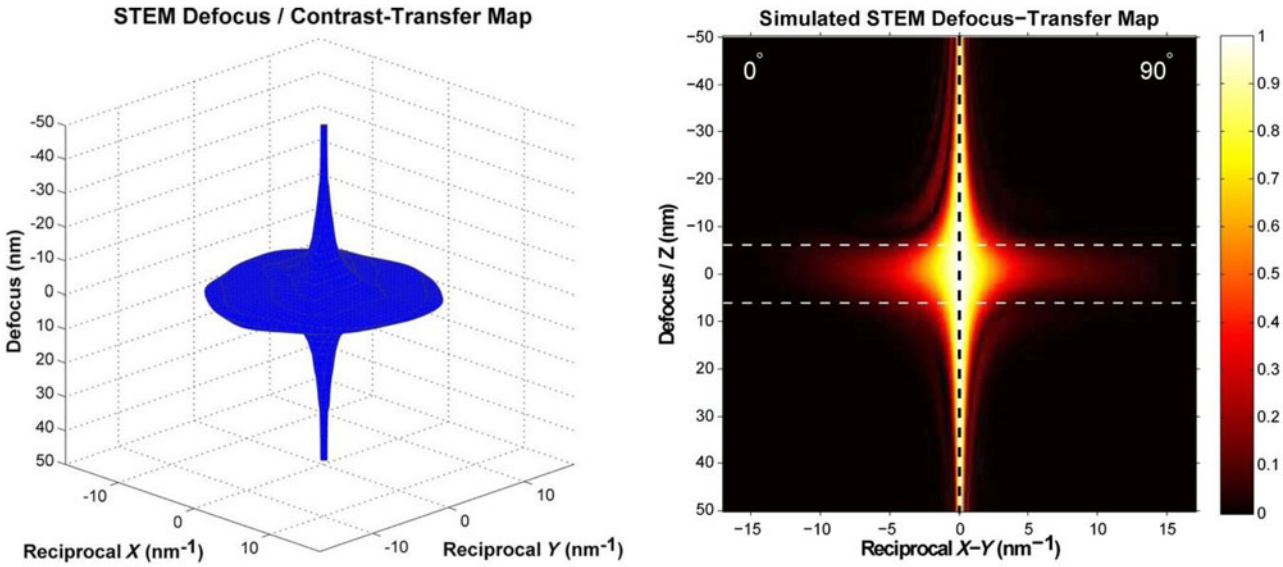

Fig. 12. Left-hand panel: the 3D optical transfer versus defocus iso-surface for a simulated probe with a "real" mixture or aberration strengths, orientations, and other microscope properties. Bounding surface shows 10% optical level. Right-hand panel: sections through the modulus of the 3D optical transfer function in the reciprocal *x*-direction (left half) and at 90° from this, in the reciprocal *y*-direction (right half). Reproduced from Jones & Nellist (2014).

assumption is generally valid for atomic-resolution STEM imaging. At the exit surface of the specimen, the amplitude distribution of electrons scattered into a solid angle $\boldsymbol{\Omega}$ with an energy E can be described by a wave function $\psi(\boldsymbol{\Omega}, E)$, where E is the energy of the (elastically or inelastically) scattered electrons. For elastic scattering, $E = E_0$ (incident electron energy). For inelastic scattering, $E = E_0 - \Delta E$, where ΔE is the energy loss of the incident electrons due to inelastic scattering events by sample electrons or phonons. At the far-field (Fraunhofer diffraction condition) detector plane, a diffraction pattern appears and can be recorded by a camera. Ideally, the diffraction pattern should be separated into many individual sets of patterns by a spectroscopic-diffraction approach: Each diffraction pattern is recorded with a specific electron energy. For example, elastically scattered electrons provide a zero-energy-loss diffraction pattern while the diffraction pattern obtained with a phonon energy loss reflects the momentum distribution of the incident electrons which are inelastically scattered by the specific type of specimen phonon excitation. Quantitative analysis of such spectroscopic-diffraction data should provide all useful information about the various electron–specimen interaction processes and consequently the nature of the specimen of interest.

If only electrons scattered along the direction $\boldsymbol{K}$ are considered, then the wave function, emerging at position $\boldsymbol{X}$ on the exit surface of the specimen, can be represented as $\psi(\boldsymbol{K}, \boldsymbol{X}, E)$, where $\boldsymbol{K}$ is a two-dimensional reciprocal space vector with the amplitude determined by $|\boldsymbol{K}| = 2\sin\left(\frac{\theta}{2}\right)/\lambda$ (θ is the scattering angle and λ is the wavelength of the scattered electron with energy E) and $\boldsymbol{X}$ is a two-dimensional vector in real space, describing the coordinate of the electron probe at the exit surface of the specimen. When the electron probe is scanned across a specimen, the variations in the five-dimensional wave function $\psi(\boldsymbol{K}, \boldsymbol{X}, E)$ carry all the relevant information about the specimen structure and chemistry. Since the wave function $\psi(\boldsymbol{K}, \boldsymbol{X}, E)$ is not an observable, what is experimentally recorded at the STEM detector plane is the intensity $I(\boldsymbol{K}, \boldsymbol{X}, E)$, which is proportional to $|\psi(\boldsymbol{K}, \boldsymbol{X}, E)|^2$. Assuming that the elastically scattered electrons do not coherently interfere with the inelastically scattered electrons, then the experimentally (without energy filtering) recorded intensity is $I(\boldsymbol{K}, \boldsymbol{X}) = \int I(\boldsymbol{K}, \boldsymbol{X}, E)dE$. It should be noted that when the electron probe is moved across a specimen, the local intensity of the diffraction pattern may redistribute, but the integrated total intensity of the whole diffraction pattern should be constant regardless of the probe position and probe size (preservation of the electron flux). The integration over energy may impose strict requirements on sample thickness and incident beam energy: Extremely thin samples or use of very high incident electron energies simplify the image interpretation.

When the detected signal, corresponding to each probe position, is displayed, a two-dimensional image is formed. Variations in the signal strength, collected by the STEM detector, provide image contrast. The various types of STEM images include X-ray maps, secondary electron images, Auger electron images, images formed with elastically scattered electrons or inelastically scattered electrons, etc. In the following discussion, we only focus on STEM images that are formed by collecting elastically or inelastically scattered primary electrons. For each fixed probe position $\boldsymbol{X}$, a full diffraction pattern appears on the detector plane. If each detector pixel records and converts the detected signal independently, then the detected signal strength corresponding to the specimen position $\boldsymbol{X}$ can be expressed as

$$I(\boldsymbol{X}) = \int D(\boldsymbol{K})|\psi(\boldsymbol{K}, \boldsymbol{X})|^2 d\boldsymbol{K} = \iint D(K_x, K_y)|\psi(K_x, K_y, \boldsymbol{X})|^2 dK_x dK_y, \quad (1)$$

where $D(\mathbf{K})$ is a two-dimensional detector function (The detector function is usually a step function but can become more complicated to represent a configured detector). We dropped the energy dependence of the wave function on the assumption that the STEM detector collects all the elastically and inelastically scattered electrons with equal efficiency. For a thin specimen, all the transmitted electrons arrive at the detector plane and the detector

Downloaded from https://www.cambridge.org/core. IP address: 68.98.49.119, on 04 Sep 2021 at 06:14:57, subject to the Cambridge Core terms of use, available at https://www.cambridge.org/core/terms. https://doi.org/10.1017/S1431927621012125

response can be assumed to be independent of angle and energy of the scattered electrons (This assumption is correct for general ADF and BF detectors. However, this assumption is not correct when an electron spectrometer is used). Under these assumptions, the intensity integration over the whole two-dimensional detector plane should be constant (preservation of the incident electron flux). By adding the signal strength of all the STEM detectors that cover the whole diffraction plane, we obtain

$$I(\boldsymbol{X}) = \sum_i \int_{K_i}^{K_{i+1}} D_i(\boldsymbol{K}) |\psi(\boldsymbol{K},\ \boldsymbol{X})|^2 d\boldsymbol{K} \equiv \mathrm{C}, \tag{2}$$

where $D_i(\boldsymbol{K})$ represents the detector function of the ith STEM detector, the summation is over all the STEM detectors, and C is a constant. In equation (2), the total probe intensity can be normalized to unity ($C = 1$). The physical picture of equation (2) can be visualized as if the whole diffraction pattern at the detector plane is filled with independent STEM detectors of various sizes and shapes. The summation of the intensities of all the STEM detectors represents the total intensity of the whole diffraction pattern, which should be constant and does not depend on the probe position, probe size, defocus, or lens aberrations. Equation (2) clearly demonstrates the flexibility of STEM detectors and the intrinsic relationship among these detectors. Even though an infinitely large STEM detector, which can be divided into many detectors of various shapes and sizes, does not provide any information about the specimen, each individual detector, regardless of its size and shape, provides specific information about the specimen. The size, shape, and position of each individual STEM detector control the image contrast and the resolution of the corresponding STEM image if the incident probe size is small enough.

If a point STEM detector, which is represented by δ ($\boldsymbol{K}$-$\boldsymbol{G}$) (where $\boldsymbol{G}$ is a vector drawn from the optic axis to any point on the diffraction pattern), is used, then equation (1) gives $I(\boldsymbol{X}) = |\psi(\boldsymbol{G},\ \boldsymbol{X})|^2$. When $\boldsymbol{G}$ is at the optic axis or at a Bragg diffraction spot of a crystalline specimen, the STEM image is equivalent to a BF or tilted DF TEM image with parallel illumination, respectively. If the STEM detector is slightly enlarged but is still considered to be small, then the STEM image is equivalent to the corresponding TEM image obtained with an incoherent convergent illumination, blurring the phase-contrast features. When the CBED disks overlap, lattice fringes should be detected if the small STEM detector is positioned within the overlapping regions. Two-dimensional fringes should be formed when the STEM detector is positioned at any point within the regions that three or more noncollinear diffraction disks overlap. Therefore, atomic-resolution phase-contrast BF and DF STEM images can be obtained and interpreted, similar to those of HRTEM images. Such imaging modes, however, do not have any advantages over the HRTEM technique, except for nanoanalysis and nanodiffraction studies, or for imaging thicker samples.

If many small STEM detectors ($D(\boldsymbol{K}) = \sum_0^N \delta(\boldsymbol{K} - \boldsymbol{G}_n)$) are used together to collect all the Bragg diffracted peaks and the transmitted beam (or if all the diffracted and transmitted spots are excluded), then the image contrast in the corresponding STEM image should highlight specimen features that cause diffuse scattering (phonon scattering plus diffuse scattering from defects). If the diffraction disks overlap, one can collect all the equivalent overlapping regions to enhance the signal-to-noise and signal-to-background ratios. In the late 1980s, the present author tried these approaches on Cowley's unique optical systems attached to his high-resolution VG HB5. Due to the low signal-to-noise ratio and complications in precisely positioning the masks at the desired locations, such work, however, did not yield fruitful results. Nowadays, such a scheme can be easily accomplished by using high-quality electron detectors, digital acquisition and processing methods, and reconstruction algorithms, leading to four-dimensional electron microscopy which will be discussed later.

If only two complementary STEM detectors are used to collect the whole electron diffraction pattern, then the corresponding STEM images are complementary to each other regardless of the shape, size, or position of the two detectors. A simple example consists of a disk detector and a complementary annular detector, both centered at the optic axis, covering the whole electron diffraction pattern at the detector plane. The relationship between the two complementary STEM images is given by

$$I(\boldsymbol{X}) = \int_{u_C}^{\infty} D(u) |\psi(u, \boldsymbol{X})|^2 du = 1 - \int_0^{u_C} D(u) |\psi(u, \boldsymbol{X})|^2 du, \tag{3}$$

where u_C represents the radius of the disk detector or the inner radius of the annular detector. For a thin specimen, the signal strength of electrons, which are scattered to very large angles, is negligible. In this case, extending the integration over the outer radius of the annular detector to infinity should not introduce appreciable error. For thick specimens, which most probably is not relevant to high-resolution imaging, such an approximation is not valid (Liu & Cowley, 1991, 1993). In theory, subtraction of a uniform background from an STEM image should not modify the characteristics of the corresponding image. Therefore, the normalized image contrast of the two complementary STEM images can be considered as $C_{\mathrm{ADF}}(\boldsymbol{X}) = -C_{BF}(\boldsymbol{X})$. Regardless of the size of the inner angle of the annular detector, the corresponding BF STEM image (right-hand side of (3)) is always complementary to the ADF STEM image (left-hand side of (3)) and these pair images should always possess the same imaging characteristics. By generalizing this specific example, one can state that the two complementary STEM images should contain the same amount of information but with a contrast reversal. From this perspective, an HAADF-STEM image, regardless of the inner collection angle, contains the same type of information about the specimen as the corresponding complementary BF (cBF) STEM image does.

When u_C becomes small (small inner collection angle of the ADF detector), phase contrast may become dominant in the low-angle ADF STEM image. When u_C becomes large, the phase contrast is suppressed and the Z-contrast can become dominant in both the HAADF and the cBF pair images, complementary to each other, and the image resolution can be significantly improved in both images (Liu, 1990; Liu & Cowley, 1991, 1993). The contrast in an STEM image strongly depends on the specific size, shape, and position of the STEM detector, varying from predominantly interference-based phase contrast to incoherent Z-contrast. In fact, any types of STEM detector can be designed and implemented to acquire useful information about the specimen. Cowley explored different types of STEM imaging modes by developing specialized detectors (Cowley, 1993; Cowley & Liu, 1993; Cowley et al., 1995). In particular, he focused on the use of a thin annular detector (TAD) to select the specific angular range of the scattered electrons for resolution improvement and/or for contrast enhancement of specific elements of interest. By employing a TAD (with a width

Downloaded from https://www.cambridge.org/core. IP address: 68.98.49.119, on 04 Sep 2021 at 06:14:57, subject to the Cambridge Core terms of use, available at https://www.cambridge.org/core/terms. https://doi.org/10.1017/S1431927621012125

equal to ~10% of the inner radius) and the use of post-specimen lenses, Cowley developed several STEM imaging modes including the TAD-based BF, DF, and marginal imaging configurations (Cowley, 1993, 2001; Cowley et al., 1995; Liu & Cowley, 1996). He discussed why these special imaging modes, based on the estimation of the point spread functions, would provide much better image resolution. By selecting the appropriate angular range with a TAD, light-element clusters dispersed on heavy-element supports can be distinguished (Liu & Cowley, 1996; Cowley, 2001). For the STEM marginal imaging mode, the image contrast is proportional to the square of the differential of the projected specimen potential, and thus any deflection of the incident beam spot due to a change of the projected potential gives bright contrast in the marginal TAD STEM images.

The angular dependence of scattered electrons, combined with the intrinsic characteristics of annular ring detectors, was used for special purposes (Cowley, 2001). Such an angular-filtered imaging strategy was used to image thick amorphous/biological samples and other types of materials (Smith & Cowley, 1975; Liu & Cowley, 1991, 1993, 1996; Haider et al., 1994; Cowley, 2001; Hyun et al., 2008; de Jonge et al., 2009; Zhang et al., 2015). The flexibility of designing and developing STEM detectors affords us to explore the reciprocal space of the specimen in many different ways. By selecting specific regions of the reciprocal space, one can extract specific type of information that is present in the real space. For example, angle-selective (or momentum-selective) imaging approaches have been effectively utilized (Daberkow et al., 1993; Haider et al., 1994; Hammel & Rose, 1995; Zhang et al., 2015; Müller-Caspary et al., 2016; Johnson et al., 2017). By selecting a small range of low scattering angles, the contrast of defect-containing atomic columns was investigated (Johnson et al., 2017). Although the image contrast is still affected by the sample thickness, crystal orientation, local strain, and probe convergence angle, the angle-selective imaging method opens new possibilities for 3D structural characterization of individual point defects in functional materials.

Annular Bright-Field (ABF) and Differential Phase-Contrast STEM Imaging

Based on the reciprocity principle, phase-contrast STEM images should be obtainable by placing a small axial detector at the optical axis of the microscope. BF STEM images acquired with such small disk detectors, however, usually have very low signal-to-noise ratio since the majority of the transmitted/scattered electrons within the illumination cone are excluded. The signal-to-noise issue becomes more problematic for atomic-resolution STEM imaging with small-probe sizes which require large probe-forming apertures. Thomson analyzed the image quality issues and proposed to use large-axial BF STEM detectors to enhance signal strength without compromising too much on phase contrast (Thomson, 1973). Similar to phase-contrast TEM images, phase-contrast STEM images of a periodic crystal lattice have no obvious plane of focus for maximum interpretability since the electron waves, originated from different atomic sites, constructively or destructively interfere at different image planes (Cowley & Moodie, 1957). At each focal plane, the relationship between the positions of the "atom" columns in the image and the actual positions of atom columns in the crystal unit cell is typically ambiguous; rigorous image simulations are usually required to extract the exact positions of atomic columns. The flexibility of configuring the STEM detector provides a unique approach to forming different types of images that contain specific types of specimen information. After carefully examining the potential imaging modes on an STEM, Rose explored the use of an annular bright-field (ABF) detector to improve the quality of phase-contrast STEM images (Rose, 1974; Fertig & Rose, 1979). Rose proposed simultaneous acquisition of two types of images: One detector system consisted of an ABF detector to collect BF signal from the outside of the illumination cone and another BF disk detector beneath the ABF detector to collect the remaining BF signal. Rose further proposed that the image contrast would be enhanced by taking the difference between the simultaneously registered signals from the two detectors. Such STEM images might result in improved resolution over that of the CTEM or BF STEM images.

Based on the reciprocity principle, TEM images obtained with hollow-cone illumination (Mathews, 1953) or the use of a ring-shaped condenser aperture should provide similar high-resolution images obtained with an ABF or TAD detector. Therefore, the contrast transfer in ABF imaging is expected to yield better image resolution than the conventional BF STEM and possesses nonoscillating contrast transfer characteristics (Saxton et al., 1978). Early experimental results demonstrated the advantages of such a TEM imaging mode, revealing simultaneously different sets of lattice fringes of Au nanoparticles (Heinemann & Poppa, 1970) and DF/BF imaging with the hollow-cone illumination resolved isolated heavy atoms (Thon & Willasch, 1972). The ring-shaped objective aperture in TEM was tried to enhance image resolution and contrast in DF TEM images (Heinemann & Poppa, 1972). The use of ring-shaped condenser apertures or hollow-cone illumination was expected to yield images free of chromatic aberration effects (Komoda, 1966; Cowley, 1973*a*), and significant improvement in image resolution as well as the signal-to-noise ratio were obtained (Mathews, 1953; Cowley, 1973*a*, 1973*b*; Rose, 1977; Dinges et al., 1994; Rosenauer et al., 2014).

Although Cowley investigated the potential advantages of the various types of TAD detectors including the TAD-based BF configurations (Cowley et al., 1995; Cowley, 2001), the full advantages of atomic-resolution ABF imaging of light elements in practical crystalline samples were not clearly demonstrated until much later. Okunishi et al. (2009), using an aberration-corrected TEM/STEM which was equipped with an ABF and an ADF detector to simultaneously acquire both ABF and HAADF images, unambiguously and clearly resolved both cations and anions in $SrTiO_3$ and Fe_3O_4 samples. In a subsequent paper, Findlay et al. (2009) discussed the image contrast variations with sample thickness and electron probe defocus. Based on the s-state channeling model of fast electrons (Van Dyck & Op de Beeck, 1996), Findlay et al. (2009) generalized such an electron propagation model to explain the experimentally observed ABF image contrast. Through both experimental results and systematic simulations, the authors demonstrated that an ABF detector would produce an "absorption" image, revealing both heavy- and light-atom columns of a zone-axis crystal. The authors further demonstrated that ABF images, complementary to simultaneously acquired HAADF images, were robust and interpretable over a wide range of specimen thicknesses. The characteristics of the ABF imaging mode are very different from those of pure phase-contrast TEM/STEM imaging modes, and the ABF method constitutes a powerful approach to identifying atom locations of both light and heavy elements in a crystalline specimen.

Findlay et al. (2010*a*, 2010*b*) further investigated the dynamics of ABF image formation and its contrast characteristics. These studies firmly established the foundations of reliably imaging both light- and heavy-element columns over a range of sample thicknesses.

Downloaded from https://www.cambridge.org/core. IP address: 68.98.49.119, on 04 Sep 2021 at 06:14:57, subject to the Cambridge Core terms of use, available at https://www.cambridge.org/core/terms. https://doi.org/10.1017/S1431927621012125

The authors discussed the dependence of ABF image contrast on specimen thickness, detector configuration, probe size/defocus, and the sensitivity of this imaging method to intercolumn spacing and local crystal disorder. Through a comprehensive image simulation study, the authors confirmed the robustness of the ABF imaging mode with respect to sample thickness and a limited defocus range over which the ABF images would be directly interpretable. They further demonstrated that, unlike the HAADF imaging mode, the ABF image contrast might not have an intuitively interpretable dependence on the atomic number of the element of interest. The s-state electron-channeling model is intuitively simple but has its limitations. For example, such a simplified model breaks down when the intercolumn spacing becomes small enough that the s-states of adjacent columns of atoms overlap (Anstis et al., 2003). Both experimental studies and image simulations (Findlay et al., 2010*a*, 2010*b*) showed that the ABF image intensity of atomic columns oscillated with sample thickness, especially for thin specimen and/or light elements. Although the s-state electron-channeling model is adequate for interpreting ABF image contrast of certain light elements, thermal diffuse scattering should be considered for understanding the ABF image contrast of heavy elements. Diffuse scattering of incident electrons may play a more important role in ABF images obtained with smaller probe sizes (larger illumination cone), of crystals containing defects/disorders, or of thicker specimens.

The simple s-state channeling model may not work well for understanding ABF images of ultra-light elements, such as hydrogen or lithium, since the attractive potential to confine the electrons traveling along the atomic columns is relatively weak. The optimization of the ABF imaging detector configurations was conducted. For example, Ohtsuka et al. (2012) studied the image characteristics of a middle-angle BF (MABF, complementary to ABF) and concluded that both light O atomic columns and heavy Sr and Ti–O atomic columns of $SrTiO_3$(001) were visible with distinct bright and dark contrast over practical ranges of the probe-forming lens defocus and sample thickness. The authors claimed that the difference in contrast between heavy and light atomic columns is greater than that of ABF STEM images. Furthermore, Findlay et al. (2014) developed an enhanced-ABF (eABF) imaging mode to achieve a higher image contrast for light-element columns by subtracting the images obtained from these two complementary MABF and ABF detectors. These improvements are based on configuring detector size/geometry and signal manipulations, representing specific examples of the STEM configured detectors discussed in the section "Configured detectors for versatile STEM imaging". A recent example of such development is the use of annular segmented-detector configuration to enhance the image contrast of light elements by mathematical manipulation of different types of STEM images (Ooe et al., 2019).

The most important characteristics of ABF imaging is the precise and simultaneous identification of atom positions of both light- and heavy-element columns in a zone-axis crystal. The HAADF image intensity strongly depends on the atomic number ($\sim Z^{4/3\text{-}2}$) and the inner collection angle (Treacy, 2011). Although it is difficult to establish a direct relationship between the ABF signal strength and the atomic number of the probed element, Findlay et al. (2010*a*, 2010*b*) proposed, under relatively ideal imaging and specimen conditions, a weaker dependence of ABF signal strength on the atomic number ($\sim Z^{1/3}$). The significantly reduced dependence on atomic number Z makes it possible to visualize both light and heavy elements in the same ABF image. To appreciate the effect of such difference in the Z-dependence on atom visibility in ABF and HAADF images, Figure 13 shows the plots of $Z^{1.7}$ (representing HAADF imaging) and $Z^{0.33}$ (representing ABF imaging) versus atomic number Z. Although such a comparison is not necessarily rigorous, one can immediately and intuitively understand that compared with the HAADF signal strength, the ABF signal strength only weakly depends on the atomic number Z, leading to appreciable atom visibility for all elements within a specimen. On the other hand, the large difference in signal strength between a light element (e.g., Li) and a relatively heavy element (e.g., Co) in an HAADF image overshadows the visibility of the light element due to the integrated effects of (1) nonlocal nature of the probe intensity profile, (2) nonlocalized scattering cross-sections, and (3) short distances among the nearest atom columns of different elements within a crystal. Figure 13 implies that the chemical sensitivity of the HAADF imaging mode is much higher than that of the ABF imaging mode. Without detailed image simulations, one may not be able to intuitively correlate the absorption contrast in ABF images with the atomic number Z of the elements of interest. Under certain imaging conditions, contrast reversal in ABF images can occur. For example, Lee et al. (2013) reported that for very thin specimens, ABF images showed dark dips at atomic columns in over-focus and reversed to bright peaks in under-focus. These authors further demonstrated that for the same incident probe convergence angle, the depth of focus (DOF) was narrower in an ABF image than in an HAADF image and the optimum defocus for ABF imaging was closer to the specimen surface. The combination of the ABF imaging mode with the corresponding HAADF imaging mode, however, significantly enhances the power of STEM in solving challenging materials problems. ABF STEM imaging, in combination with HAADF imaging, provides quantitative measurement of local structure distortion, especially for structural investigations of complex oxides (Aso et al., 2013, 2014; Gao et al., 2016*a*; Kim et al., 2017).

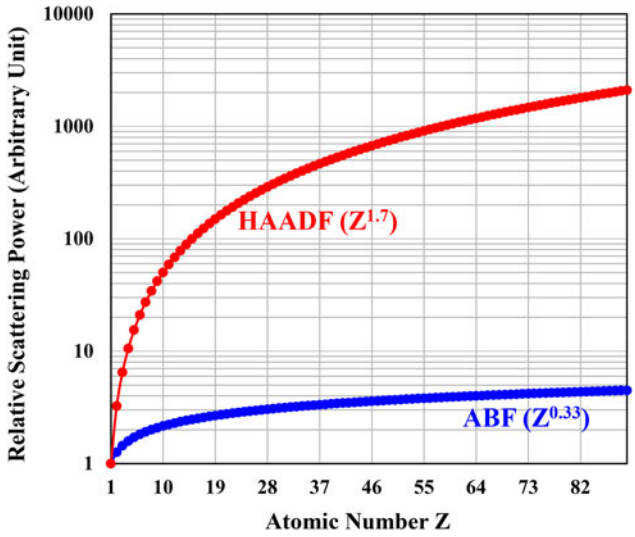

Fig. 13. Plots of the dependence of HAADF ($\sim Z^{1.7}$) and ABF ($\sim Z^{1/3}$) signal strength on the atomic number Z.

Full understanding of the factors that affect the precise measurement of atom positions in ABF images is of importance for precise measurement of distances and angles between different atomic columns in a crystal. Based on the dynamical scattering theory, Van Dyck et al. (1998) discussed the effects of different range of specimen tilt on electron channeling in crystalline specimens. Investigations on how a specimen tilt affects the contrast of

Downloaded from https://www.cambridge.org/core. IP address: 68.98.49.119, on 04 Sep 2021 at 06:14:57, subject to the Cambridge Core terms of use, available at https://www.cambridge.org/core/terms. https://doi.org/10.1017/S1431927621012125

atomic-resolution ADF STEM images were conducted (Yamazaki et al., 2002; Maccagnano-Zacher et al., 2008; Yu et al., 2008; So & Kimoto, 2012; Cui et al., 2017). Since the contrast of an ABF image is at least partially determined by the phase of the forward-scattering electrons, the tilt of the incident electron beam with respect to a crystal zone axis may have a larger impact on ABF imaging than on HAADF imaging. Specimen tilt might cause significant artifact in extracting correct atom positions from STEM images. For example, Gao et al. (2016*b*) found that in a tilted crystal, the shift of atom positions depended on atom species, that is, larger shift for lighter anion columns and smaller shift for heavier cation columns. They also found that the tilt-induced displacement of atom positions depended on electron probe defocus, incident beam convergence angle, and specimen thickness. Zhou et al. (2016) investigated the deviations of atom positions in ABF images from those of the corresponding ADF images and studied the effect of specimen tilt on the bond angle measurements in ZrO_2. Brown et al. (2017) proposed a method for evaluating and correcting specimen tilt by simultaneously recording a central BF STEM and the corresponding ABF STEM image. Kim et al. (2017) quantitively compared the BF and ABF STEM images and discussed the robustness of structural measurements of oxygen octahedral tilts as a function of specimen tilt and electron probe defocus. With the understanding of the characteristics of the ABF imaging mode, picometer-scale atom position determination of light elements became plausible (Gao et al., 2018).

The simultaneous acquisition of HAADF and ABF images to visualize atomic columns of a large range of various cations and anions is critical to atomic-scale study of materials systems that consist of both light and heavy elements. The development of the ABF imaging mode significantly enhanced the power of atomic-resolution STEM imaging of a wide variety of crystalline specimens. Such atomic-resolution imaging capabilities proved to be essential for correlating macroscopic properties of complex oxides to the small changes of ligand coordination or the exact arrangement of oxygen sub-lattice at hetero-interfaces (Huang et al., 2014). Because of its power in resolving atomic columns of light elements, the ABF imaging method was readily applied for direct imaging of hydrogen columns in crystalline solids (Findlay et al., 2010*a*, 2010*b*; Ishikawa et al., 2011; Kim et al., 2013), Li atoms in battery-related materials (Oshima et al., 2010; Gu et al., 2011, 2015; Huang et al., 2011; Lee et al., 2012; Yu et al., 2013; Findlay et al., 2017), and a plethora of other materials systems. Other example applications of ABF STEM imaging include visualization of oxygen vacancies in a perovskite oxide (Kobayashi et al., 2012), observation of electrically induced migration of oxygen vacancies (Zhang et al., 2017), and quantitative evaluation of oxygen distortions in lithium-rich transition-metal-oxide cathodes (Liberti et al., 2020).

Differential phase contrast (DPC), using a detector system consisting of two half discs, was proposed to extract unique features of the specimen (Dekkers & De Lang, 1974). Theoretical considerations (Rose, 1976, 1977) suggested that the image, formed by taking the signal difference between the two half-disk detectors, would provide the gradient of the object potential along the scan direction. STEM detector systems consisting of four quadrant detectors were proposed as well (Rose, 1977) and DPC imaging method was applied to visualize magnetic domain wall profiles by using an annular detector consisting of eight segments (Chapman et al., 1978). Butler & Cowley (1983) investigated the DPC using a split-field detector arrangement and studied the contrast and resolution of DPC images as a function of detector aperture size. These early examples clearly demonstrated the flexibility of the STEM imaging modes and their potential for providing unique and useful information about the specimen, especially with better electron detectors, faster computers, and efficient algorithms for real-time image processing.

With the development of aberration-corrected STEM and highly sensitive electron detectors, atomic-resolution DPC images, formed by using different types of STEM detectors and the subsequent image processing, have demonstrated the power of such imaging modes in providing useful information about the specimen. Segmented detector with 16 segments was developed to form atomic-resolution images (Shibata et al., 2010), yielding information on the gradient of the electrostatic potential of columns of atoms (Shibata et al., 2012). Example applications of DPC STEM imaging include observation of the magnetic skyrmion domain boundary structure (Matsumoto et al., 2016), quantitative electric field measurement of quantum well structures (Lohr et al., 2016) and p-n junctions (Toyama et al., 2020), and direct visualization of the magnetostructural phase transitions (Almeida et al., 2020). Electric field imaging of individual single Au atoms was reported (Shibata et al., 2017), clearly demonstrating the power of atomic-resolution DPC method (Fig. 14). DPC STEM imaging of real-space charge density with sub-Ångstrom resolution provided an important approach to studying local bonding in crystalline solids (Gao et al., 2019).

For thin specimens, the integrated DPC (iDPC) method (Lazić et al., 2016) possesses advantages for imaging both light and heavy elements (Yücelen et al., 2018). The iDPC STEM imaging method was used to detect hydrogen atoms at metal–metal hydride interfaces (de Graaf et al., 2020) and subsurface interstitial hydrogen in palladium hydrides (Lin et al., 2020). For thicker specimens, large illumination angles may enable accurate structure reconstructions of electric potentials by incorporating probe spreading via a multiple plane phase-contrast transfer function (Brown et al., 2019). The effect of lens aberrations, electron-beam tilt, and specimen thickness on DPC STEM imaging characteristics was investigated (Buerger et al., 2020). Understanding of these factors is critical to correctly interpreting and quantifying contrasts in DPC images. Ultrahigh-contrast STEM imaging via high-speed segmented/pixelated detectors by optimum BF (OBF) STEM imaging mode may significantly reduce the electron dose without compromising image resolution (Ooe et al., 2021). Breakthrough developments in electron detectors, computers, and algorithms significantly advanced the practical realization of imaging technologies.

Coherent versus Incoherent STEM Imaging

The flexibility of STEM imaging provides various approaches to forming images of the sample of interest. Configured STEM detectors, however, can provide entirely different views of the specimen, yielding completely different contrast, resolution limits, and chemical sensitivity. Multiple STEM images can be simultaneously acquired with the same incident electron probe, but the interpretation of these images can be totally different depending on the specific detector size and configuration. For example, when the inner collection angle of the ADF detector increases, the characteristics of the ADF and its corresponding cBF STEM images change from coherent phase contrast to incoherent *Z*-contrast. For heavy metal atoms supported on ultrathin amorphous carbon films, even low-angle ADF images revealed a certain degree of *Z*-contrast of metal atoms and demonstrated characteristics of incoherent imaging (Crewe et al., 1970; Wall

Downloaded from https://www.cambridge.org/core. IP address: 68.98.49.119, on 04 Sep 2021 at 06:14:57, subject to the Cambridge Core terms of use, available at https://www.cambridge.org/core/terms. https://doi.org/10.1017/S1431927621012125

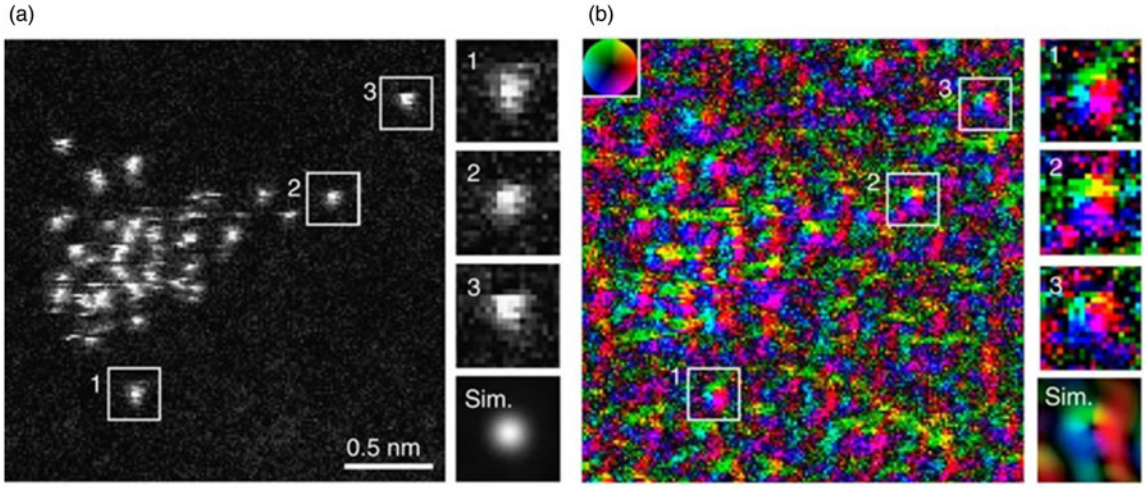

Fig. 14. Simultaneous atomic-resolution ADF STEM image (**a**) and electric field vector map (**b**) of Au single atoms. The dwell time is 300 μs per pixel. The inset color wheel indicates how color and shade denote the electric field orientation and strength. Magnified images from three isolated Au atom positions are indicated. Simulated image of a single Au atom supported on a 10 nm-thick amorphous carbon substrate is also shown. Reproduced from Shibata et al. (2017).

et al., 1974*a*, 1974*b*; Crewe, 1979, 1983*a*, 1983*b*). The very large HAADF detector configurations that were used to image supported metal catalysts also demonstrated characteristics of incoherent imaging (Treacy et al., 1980; Treacy, 1982; Treacy & Rice, 1989). The incoherent imaging characteristics include: (1) no contrast reversal with defocus, (2) no interference fringes at interfaces and surfaces, (3) no thickness fringes at crystal wedges, and (4) high atomic number sensitivity. Moreover, the image intensity in an HAADF image of a thin specimen may increase linearly with sample thickness provided that electron-channeling conditions are avoided.

Based on image formation theory, for the same lens systems, incoherent imaging yields higher image resolution than coherent imaging (Scherzer, 1949). When a zone-axis crystalline specimen is imaged with an ADF detector, the situation becomes dubious: Is the acquired image coherent or incoherent? The question arises about the exact inner angle of the ADF detector for incoherent imaging. Early calculations (Engel et al., 1974; Misell et al., 1974) suggested that if the ADF detector collected all of the scattered electrons, then the incoherent imaging characteristics would be displayed. Cowley (1973*a*, 1976), however, pointed out that the scattering of high-energy incident electrons by coordinated atoms in a crystalline specimen to an ADF detector might not be a simple summation of independent intensity contributions. Another question arises about the fact that one cannot separate out the scattered electrons from the nonscattered electrons since large convergence angles of the primary electron beam are needed to achieve atomic-resolution imaging. For example, when high-order lens aberrations are corrected, the incident illumination cone may extend to 70–100 mrad even with 200 keV electrons.

Equation (3) discussed in the section "Configured detectors for versatile STEM imaging" is valid as long as the total flux of the incident electrons is preserved. Therefore, the characteristics of ADF images can be understood in terms of the characteristics of the corresponding cBF images provided that the outer angle of the ADF detector is large enough (This assumption implies that the signal strength for electrons scattered at angles larger than the outer angle of the ADF detector is negligible). Since the cBF detector can be considered as the summation of many small detectors with their detector function approaching a delta function, the cBF image intensity can be considered as the summation of the intensity of all the phase-contrast STEM images obtained with such infinitely small BF STEM detectors. The contrast of the cBF and thus the corresponding ADF image is controlled by the sum of all the phase-contrast BF STEM images. Based on the reciprocity principle, a cBF STEM image should be equivalent to a TEM image that is obtained with an incoherently filled illumination aperture, the size of which is determined by the size of the corresponding cBF detector. By analyzing the coherence length of the incoherently filled TEM condenser aperture at the specimen, we can comprehend how a cBF (ADF) STEM image changes from fully coherent to fully incoherent by simply increasing the size of the cBF detector continuously. Furthermore, we will show that in an ADF STEM image, the larger features may be interpreted by an incoherent imaging theory while the smaller features have to be interpreted by a coherent imaging theory. From this perspective, an ultrahigh-resolution ADF STEM image always contains both coherent and incoherent imaging details. For further discussions on partial coherent imaging in scanning microscopes and the effects of detector sizes, the reader should consult relevant publications (Burge & Dainty, 1976; Fertig & Rose, 1977; Sheppard & Wilson, 1978; Wilson & Carlini, 1987).

We assume that the intensity distribution of the detected electrons is uniform on a disk-like cBF detector with a radius u_C, corresponding to a collection angle of θ_C. Such an assumption greatly overestimates the detected intensity at large scattering angles. In practice, the electron intensity at each detector pixel should be determined by the resultant dynamical electron diffraction pattern, which depends on the crystal structure and orientation, thickness of the specimen, electron probe characteristics, and so on. With the use of such a simplified model, one can, however, easily estimate the widths of transverse coherence/incoherence present in the cBF and the corresponding ADF STEM images. For an incoherently filled TEM condenser aperture, the incoherence and coherence width at the specimen can be approximated by $X_i = \lambda/\theta_C$ and $X_C = \lambda/(2\pi\theta_C)$ (Spence, 2013), where θ_C corresponds to the inner collection angle of the ADF detector or the outer collection angle of the cBF detector. For any specimen features $>X_i$, the corresponding cBF and ADF STEM images can be

Downloaded from https://www.cambridge.org/core. IP address: 68.98.49.119, on 04 Sep 2021 at 06:14:57, subject to the Cambridge Core terms of use, available at https://www.cambridge.org/core/terms. https://doi.org/10.1017/S1431927621012125

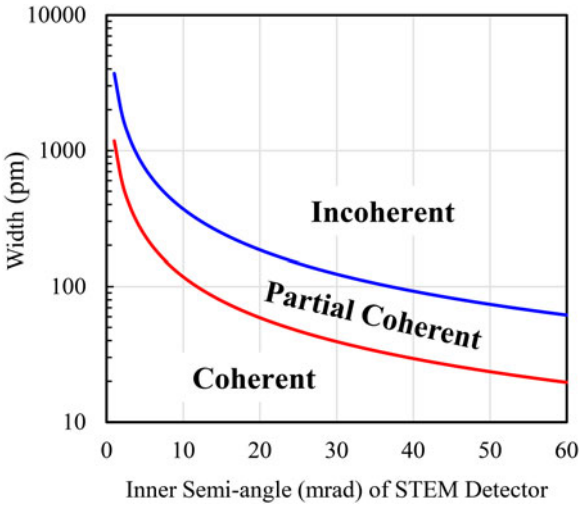

Fig. 15. Calculated dependence of coherence, partial coherence, and incoherence width on the inner semi-collection angle of an ADF detector. The calculation assumed fully coherent and infinitely small incident electron probe and extremely large outer collection angle of the ADF detector. The incoherent nature of image features strongly depends on the feature size and the inner collection angle of the ADF detector.

approximately interpreted as incoherent imaging. On the other hand, for any specimen features $<X_C$, the ADF and cBF STEM images can be interpreted as coherent imaging. For any features with length scales between these two numbers, the images possess both coherent and incoherent characteristics. To gain an intuitive understanding of this complex nature of STEM images, Figure 15 shows the dependence of the incoherence and coherence width on the cBF detector angle for 100 keV electrons. Without knowing the details of the specimen, these plots provide a lower limit for the coherence and incoherence width in the cBF and ADF STEM images. It is clear that for small cBF detectors (corresponding to small ADF inner detector angles), most of the high-resolution features are due to coherent imaging. On the other hand, for very large cBF detectors (corresponding to large ADF inner detector angles), even sub-Ångstrom features can be interpreted by incoherent imaging theory. Figure 15 also suggests that if a smaller probe size (e.g., ac-STEM probe) is used to improve image resolution, then much larger inner collection angles of the ADF detector have to be used to achieve incoherent imaging. If a very small electron probe is used then by varying the inner detection angle of the ADF detector, the corresponding image changes from primarily coherent imaging to primarily incoherent imaging. Since the reciprocity principle applies to inelastic electron scattering with small energy losses (e.g., phonon excitation), the above discussion is valid for experimentally observed STEM images of thin specimens. With large energy-loss electrons, the inelastically scattered electrons do not coherently interfere. Even though the model we used above is rudimentary, the general concept about coherent/incoherent STEM imaging and how the detector size plays a critical role are illustrated. In fact, the difference between incoherent and coherent imaging for a light microscope was discussed in detail by Rayleigh (1896). When there are no "permanent phase-relations" between the light emitting from different points on the object, incoherent imaging follows. For nonluminous objects, Rayleigh pointed out that the use of a convergent source of illumination, provided by a condenser lens, would result in effective incoherent imaging. The large convergence angle from a condenser lens results in a short transverse coherence width, effectively destroys the coherence between neighboring points and provides a very good approximation to incoherent imaging. Although incoherent imaging provides intuitive image interpretation, it contains less information about the specimen than coherent imaging does.

In practice, both incoherence and coherence width depend on the nature of the specimen: the projected intensity distribution on the STEM detector plane controls the minimum inner detector angle of the ADF detector that provides incoherent imaging characteristics. Since the angular dependence of the scattering cross-section is different for different atomic columns and structures, the incoherence width in an ADF image should be different when the primary electron probe is scanned across the specimen. Generally speaking, the incoherence width is larger for those elements or structures that concentrate the elastic electron scattering to smaller angles. With the use of a thin annular detector, both the coherence and incoherence width increase significantly, leading to partial coherent imaging of high-resolution details. In this case, one can utilize the characteristics of partial coherent imaging to identify the features of interest about the specimen (Cowley, 2001). Digital processing of a series of TAD images can be effectively utilized to gain image contrast and resolution.

Bloch wave and multislice calculations have been extensively carried out to understand the nature of incoherent imaging by the HAADF detector (Pennycook & Jesson, 1990, 1992; Loane et al., 1991, 1992; Jesson & Pennycook, 1993, 1995; Treacy & Gibson, 1993; Amali & Rez, 1997; Nellist & Pennycook, 1999; Nellist et al., 2000; Mitsuishi et al., 2001; Muller et al., 2001; Nellist, 2007, 2011). The outcome of these extensive studies suggests that the large size of the HAADF detector effectively suppresses transverse (perpendicular to the electron-beam traveling direction) coherence. However, phonon scattering (single plus multiple) is needed to destroy the longitudinal (along the electron beam) coherence. The vibrating atoms only coordinate the movement of its nearest neighbors along a column of atoms of a crystalline specimen and do not have long-range coordination. Therefore, a coherent volume, consisting of "cigar-like" wave packets (Treacy & Gibson, 1993), which are narrow in the transverse direction but are highly elongated along the incident beam direction, can be visualized to produce coordinated phonon scattering. Even in thick crystals where dynamical diffraction effects become dominant, the large angular range of the HAADF detector averages out the intensity variations and makes it insensitive to multiple scattering effects. Bloch wave decomposition analyses show that the highly localized 1*s* state interacts with the atomic nuclei more effectively, resulting in more large-angle scattering events than those of the less tightly bound 2*s* state. Therefore, interference at large scattering angles between the 1*s* and 2*s* states, which produces experimentally observed thickness fringes in BF/DF TEM images, is suppressed (Nellist & Pennycook, 1999; Rafferty et al., 2001; Anstis et al., 2003). Dynamical diffraction effects still persist since the electron probe does not interact equally with the columns of atoms throughout the sample depth. The HAADF intensity thus monotonically increases with sample thickness but quickly reaches a saturation point due to (1) absorption of the 1*s* state and (2) broadening of the electron probe as the electrons propagate down the columns of atoms. With a small enough electron probe incident onto a zone-axis crystal, it can be easily observed experimentally that the whole diffraction pattern brightens and "expands" when the electron probe is positioned exactly on the columns of atoms. On the other hand,

Downloaded from https://www.cambridge.org/core. IP address: 68.98.49.119, on 04 Sep 2021 at 06:14:57, subject to the Cambridge Core terms of use, available at https://www.cambridge.org/core/terms. https://doi.org/10.1017/S1431927621012125

when the electron probe is positioned at the vacuum channels (between columns of atoms), the intensity of the scattered electrons drops significantly. This is the origin of the "intuitive interpretation" of atomic-resolution *Z*-contrast STEM images of very thin specimens. When the effective sample thickness increases, such an intuitive interpretation of *Z*-contrast ADF images may not be valid. For thin specimens, both Bloch wave and multislice simulations yield similar results (LeBeau & Stemmer, 2008; LeBeau et al., 2008, 2009*a*, 2009*b*). For thicker samples, however, the Bloch wave method underestimates the intensity since it does not fully account for the effects of phonon scattering which can play a dominant role in determining the signal strength of the high-angle scattered electrons. Multislice calculations, based on the frozen-phonon model, suggest that when a small electron probe is positioned at an atom column of a zone-axis crystal, the strength of the thermal diffuse scattering is much higher than when the electron probe is positioned between the atom columns. Therefore, the HAADF detector collects not only the Rutherford-scattered electrons but also a large proportion of high-angle phonon-scattered electrons, especially for thicker crystals or specimens at high temperatures.

Electron-Beam Channeling and Atomic Focuser in STEM

Channeling of a charged particle in a crystalline solid refers to the process that the strong interaction of a charged particle with the crystal field of a specimen constrains the propagation of the charged particle along a preferred crystallographic direction (Robinson & Oen, 1963; Lindhard, 1965; Gemmell, 1974). Channeling phenomena and its induced effects reflect the nature of charged particle interactions with crystalline materials. Electron channeling in crystalline samples have long been investigated (Coates, 1967; Kreiner et al., 1970; Uggerhøj & Frandsen, 1970; Kambe et al., 1974; Komaki & Fujimoto, 1974; Joy et al., 1982). Contrary to positively charged particles, Rutherford scattering events increased for electrons moving parallel to a zone axis (axial channeling) or a net plane (planar channeling) (Uggerhøj & Frandsen, 1970). Under channeling conditions, incident electrons concentrate on the columns of nuclei and those electrons eventually suffer a high-angle Rutherford scattering or energy-loss events, resulting in a dechanneling process. For thicker samples, re-channeling may occur at the same atomic column or at a nearby atomic column (cross-talking).

Electron channeling affects the collected signal strength of both scattered electrons and emitted particles. Electron channeling modifies image contrast in atomic-resolution STEM images, especially the visibility of single-atom dopants or adatoms (Loane et al., 1988; Voyles et al., 2002, 2003; Rossouw et al., 2003). Channeling of electrons around columns of nuclei can significantly modify the emitted or inelastically scattered signals due to the crystal orientation dependence of electron interaction with the specimen atoms (Spence & Tafto, 1983; Pennycook & Narayan, 1985; Rossouw et al., 2003; Lugg et al., 2014, 2015*a*, 2015*b*; Allen et al., 2006; Kotula et al., 2012; MacArthur et al., 2017). For atomic-resolution imaging, electron channeling can be beneficial since it facilitates focusing of a highly convergent STEM probe onto a given atomic column, producing an enhanced ADF signal (Rossouw et al., 2003). Such electron-channeling effects, however, pose significant problems for implementing confocal STEM imaging to provide three-dimensional images of crystals, since the channeled electrons may stay along the atomic column for a relatively large distance (Borisevich et al., 2006; Cosgriff & Nellist, 2006). Even for small electron probes formed with very large incident beam convergence angles, which are practical on an ac-STEM and are desired for 3D STEM confocal imaging (Ishikawa et al., 2015, 2016; Nellist, 2017), channeling effects may still pose a problem. For imaging polycrystalline specimens, the channeling effects can mess up the *Z*-contrast in HAADF images, especially for relatively thicker crystalline materials of heavy elements. In this case, one may be able to differentiate the *Z*-contrast from channeling contrast by acquiring a pair of images with a slight tilt of the specimen orientation: The channeling contrast is more sensitive to specimen orientation than the *Z*-contrast, especially for electron probes with relatively small convergence angles.

Channeling effects cannot be avoided in STEM images of polycrystalline thin films regardless of detector angle since the signal strength of even backscattered electrons strongly depends on the orientation of a crystalline specimen. Depending on the specimen thickness, the change in signal strength in an HAADF image can be significant between on-channeling and off-channeling conditions. Diffuse scattering and channeling–dechanneling contrast were used to investigate defects in crystalline specimens (Cowley & Huang, 1992; Liu & Cowley, 1992; Perovic et al., 1993*a*, 1993*b*; Amali et al., 1997). When a crystal is oriented for incident electrons to channel along atomic columns, distortion of the lattice by the defect-induced strain field or the presence of any other heterogeneous entities (surfaces, interfaces, dopants, vacancies, etc.) may de-channel the electrons, leading to detectable darker contrast in ADF images. Based on electron de-channeling interpretation model, the ADF image contrast originates from any types of processes that disrupt electron-channeling conditions. On the other hand, if a crystal is oriented just slightly off the electron-channeling condition, then the strain field around a defect may induce channeling of the electron beam, leading to brighter image contrast in ADF images. Based on these discussions, defects can appear dark, bright, or even invisible in ADF images of zone-axis crystals. Huang scattering (Huang, 1947) caused by static displacements of atoms in crystals, as well as channeling-induced scattering both contribute to the collected ADF signal. At very high scattering angles (e.g., HAADF imaging), the channeling or de-channeling contrast dominates (Wang, 1994; Grillo et al., 2011; Phillips et al., 2012). The contrast features of dislocations depend on both the inner angle of the ADF detector and the depth location of the defects within a specimen (Oveisi et al., 2019). Electron channeling and de-channeling effects in crystalline specimens can be effectively utilized to facilitate investigations of interface or surface structures (Yu et al., 2008; Grillo, 2009*a*, 2009*b*; Liu & Allard, 2010; Grieb et al., 2013). For plan-view imaging of interfaces, multilayers, precipitates, dopants or supported metal atoms and clusters, electron-channeling effects can be used to enhance visibility of on-column atoms while it suppresses the contrast from atoms sitting between the atomic columns of a crystalline support (Kourkoutis et al., 2011). Such channeling effects can overshadow the *Z*-contrast and therefore should be avoided if one desires to interpret an HAADF image as *Z*-contrast image.

Dynamical diffraction of electrons can be described in real space by considering the fact that electrons are trapped in the electrostatic potential of the atomic columns of a zone-axis crystal (Van Dyck & Op de Beeck, 1996). The interaction of such channeling electrons with the atomic potential of the specimen leads to dynamical diffraction effects. The wave of the channeling electrons inside a zone-axis crystal was proposed to be compressed to subatomic dimensions along the atomic columns (Fertig & Rose, 1981). Under certain conditions, the interaction of the high-

Downloaded from https://www.cambridge.org/core. IP address: 68.98.49.119, on 04 Sep 2021 at 06:14:57, subject to the Cambridge Core terms of use, available at https://www.cambridge.org/core/terms. https://doi.org/10.1017/S1431927621012125

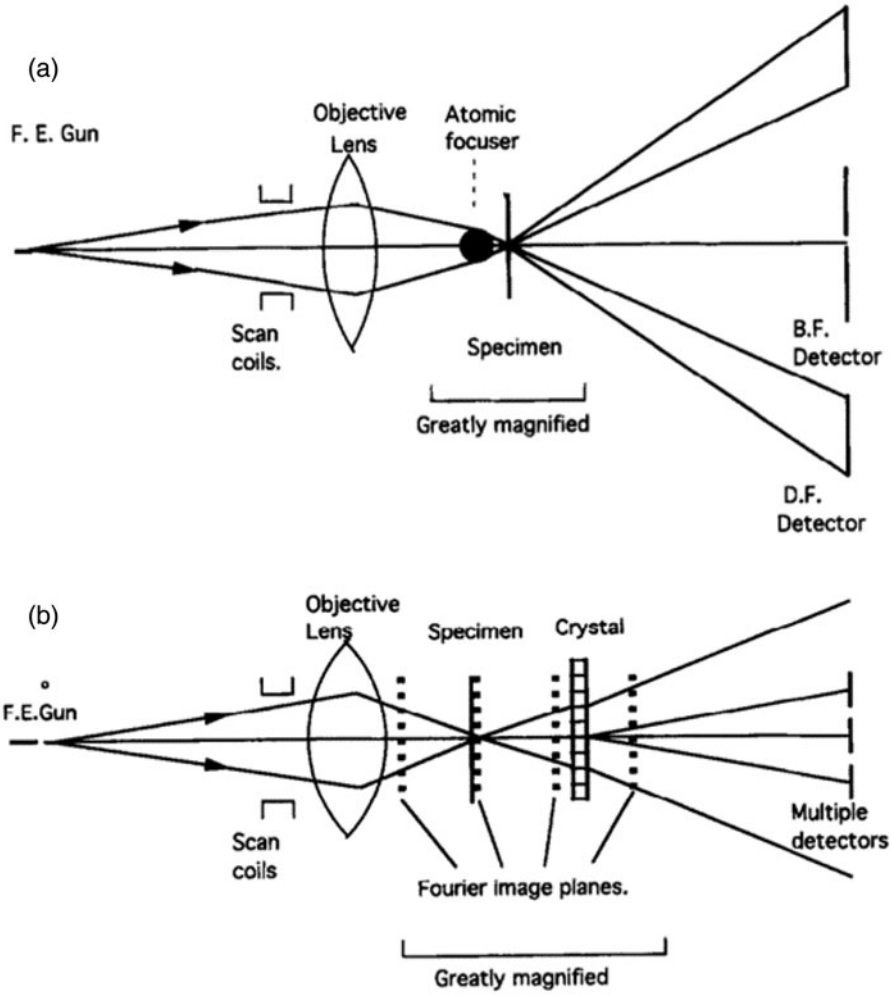

Fig. 16. Schematic diagrams illustrate the STEM imaging with a single atomic focuser (**a**) and with a thin single crystal, making use of the virtual Fourier images (**b**). Adapted from Cowley et al. (1997).

energy electrons with the crystalline specimen can be treated as if they interact with individual columns of atoms. Cowley et al. (1997) realized that when a small STEM probe was channeled along columns of atoms, the electron probe was "focused" by the electrostatic fields of the atoms to produce a much smaller probe which would persist after the electrons exited the specimen. In fact, calculations (Cowley et al., 1997) suggested that even a heavy single atom could act as a focusing lens (atomic focuser) to produce smaller electron probes (Fig. 16). Thin crystals of high-Z elements were proposed to have a significant focusing effect. A zone-axis thin crystal of a heavy metal could channel a small STEM probe to produce a sharply peaked electron beam outside the exit surface of the crystal, focusing a 0.2 nm initial probe down to ~0.05 nm via a gold atomic focuser (Cowley et al., 1997). Although such an approach to ultrahigh image resolution may work in theory, there exist practical difficulties due to fast broadening of an electron probe propagating through vacuum. Various imaging modes and designs on how to realize such an ultrahigh-resolution imaging scheme were proposed (Cowley et al., 1997; Sanchez & Cowley, 1998; Dunin-Borkowski & Cowley, 1999; Cowley, 2000; Cowley & Hudis, 2000; Smirnov & Cowley, 2002).

Both elastic and inelastic electron scattering at a particular location along an atomic column strongly depend on the spatial distribution of the probe intensity profile. Electron-channeling-induced oscillations of STEM probe intensity directly affect many types of collected signals such as emitted X-rays, electron energy-loss events, and electrons scattered into an ADF or BF detector. Understanding the electron-channeling behavior is critical to conducting quantitative analysis of STEM images and spectroscopy data. Detailed calculations (Wu et al., 2017) suggested that low-Z elements would not have much focusing effect while high-Z elements would act as excellent atomic focusers. Furthermore, the authors concluded that the propagation of the channeling electrons would be strongly regulated by the dynamic angular distribution of the traveling electron probe. Therefore, the nature of the specimen and the characteristics of the incident electron probe control how the channeling electrons produce the various types of scattered and emitted signals. Simulations of electron channeling at a subatomic length scale (Jeong et al., 2019) demonstrated that subatomic channeling of high-energy electrons could occur and such electron-channeling effects could even produce helicon-type electron beams (Fig. 17). The helicon-type electron beams may have the potential for probing electronic orbitals of atoms and for measuring magnetic properties of individual atomic columns. The subatomic channeling condition is different from that for on-column channeling. The frequency of the oscillating waves depends on the probe position relative to

Downloaded from https://www.cambridge.org/core. IP address: 68.98.49.119, on 04 Sep 2021 at 06:14:57, subject to the Cambridge Core terms of use, available at https://www.cambridge.org/core/terms. https://doi.org/10.1017/S1431927621012125

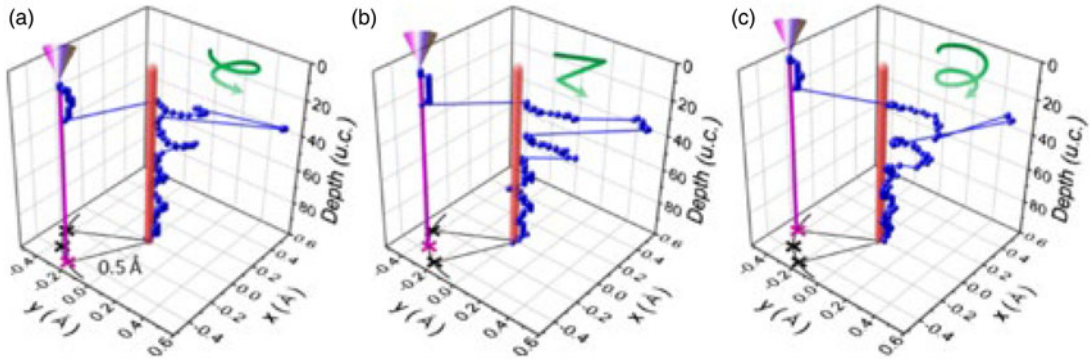

Fig. 17. The formation of a helicon-type beam around the O atomic column in the $SrTiO_3$ crystal. The paths of the electron beams are represented by the maximum intensity positions for the electron probe located at different positions R1 (**a**), R2 (**b**), and R3 (**c**). In all three cases, the probe is located 0.5 Å away from the O atomic column. R1 and R3 are located slightly off the border line, which connects two close O columns in the unit cell, and R2 is located on that line. The probe positions and O atomic column are indicated by the magenta and red vertical lines, respectively. Positions R1 and R3 produce helicon-type beams with opposite chirality, and position R2 produces an oscillating beam. Reproduced from Jeong et al. (2019).

the center of the atomic column and its atomic number (Jeong et al., 2019). The behavior of electron channeling across heterointerfaces and multilayers controls the image contrast of interfacial misfit dislocation networks in STEM-based images (Perovic et al., 1993*a*, 1993*b*; Kourkoutis et al., 2011; Oveisi et al., 2019). The interpretation of HAADF-STEM images of overlapping crystals can become quite complicated since the image appearance and contrast depend on a variety of electron optical and specimen parameters (Yun et al., 2020).

The atomic focusing model of an atom or a column of atoms was used to predict electron scattering cross-sections of heterogeneous materials (van den Bos et al., 2016). For a zone-axis-oriented crystalline specimen, the electron wave passes successive atomic focuser, producing an oscillating probe intensity that depends on the atomic number of the focusing atoms, the atom spacing along the column, the nature of the surrounding atomic columns, and the thermal vibration of the individual atoms. De-channeling can occur, for example, due to scattering by phonons and/or impurity atoms, vacancies, or other types of defects. An atomic lensing model was developed for quantitatively evaluating the 3D structure of Au@Ag core–shell nanorods (van den Bos et al., 2016) and mixed elements within columns (van den Bos et al., 2019). The use of such an atomic focuser model facilitated atom-counting in heterogeneous nanocrystals. With detailed image simulation and matching with experimental results, it was proposed that the lensing effect of an atom would be independent of electron-beam defocus. Such a method, however, may not be reliable for studying thicker samples and further investigations are needed before such a complicated image interpretation mechanism can be broadly implemented. Although an HAADF imaging mode is preferred for obtaining quantitative information about the specimen of interest, the lensing method also provided valuable information when low-angle ADF (LAADF) and medium-angle ADF (MAADF) imaging modes were employed (van den Bos et al., 2019).

Nanodiffraction, Ronchigram, Ptychography, and 4D-STEM

When an STEM probe is positioned at any point of a specimen, a CCD camera can capture all the transmitted electrons in the detector plane and, depending on post-specimen lens settings, display part or the whole scattering pattern. The characteristics of the collected diffraction pattern strongly depend on the size of the probe-forming aperture and electron-beam focus. When a small probe-forming aperture is used and the electron probe focuses at a crystalline specimen, a CBED pattern is formed. Such diffraction patterns were traditionally called microdiffraction or nanodiffraction patterns because the diffracted electrons originate from a specimen area of the size of the electron probe (Cowley, 1979a, 1980, 1981*a*, 1981*b*, 1982, 1984*a*, 1984*b*, 1984*c*, 1999, 2004; Cowley & Ou, 1989). The size of the nanodiffraction disk in the detector plane is proportional to the incident beam convergence angle. When a very small incident beam convergence angle is used, leading to large electron probe size due to diffraction effect, the observed electron diffraction patterns resemble those of selected area diffraction patterns in TEM. Structural analyses of small nanoparticles, precipitates, line defects, and so on, can be accomplished by combining STEM imaging with nanodiffraction (Zhu & Cowley, 1982; Pan et al., 1990; Liu, 2005). The diffraction spot splitting/streaking at surfaces/interfaces, due to coherent interference, was evaluated (Liu et al., 1993*b*; Gajdardziska-Josifovska et al., 1995; Liu, 2005).

When the size of the probe-forming aperture increases, diffracted and transmitted disks broaden and can overlap, yielding interference effects among the transmitted and diffracted electrons. When the probe-forming aperture is completely removed or very large, all the diffraction disks overlap with each other and with the transmitted disk, forming a highly distorted projection (shadow) image of the specimen (Cowley, 1979*a*). When the electron beam is highly defocused, the shadow-image resembles a low magnification TEM image. If a crystalline specimen is examined, then the close-to-focus shadow image consists of many sets of 1D or 2D fringes which can be highly distorted due to lens aberrations. Since the image characteristics of crystalline shadow images are similar to those observed in light optics for measuring lens aberrations by Ronchi (1964), Cowley coined the term electron Ronchigram for describing such shadow images (Cowley, 1980). The axial aberrations of a probe-forming lens are directly visible in a Ronchigram of either a crystalline or an amorphous specimen. The appearance of an electron Ronchigram depends sensitively on probe defocus, astigmatism, spherical aberration coefficient, and the alignment of the electron optical system. Cowley described the electron Ronchigram by considering a transfer function and the projected potential of a specimen (Cowley, 1976, 1979*a*, 1986). The measurement of aberration parameters of the probe-forming lens can be accomplished by using a focal series of Ronchigrams and

Downloaded from https://www.cambridge.org/core. IP address: 68.98.49.119, on 04 Sep 2021 at 06:14:57, subject to the Cambridge Core terms of use, available at https://www.cambridge.org/core/terms. https://doi.org/10.1017/S1431927621012125

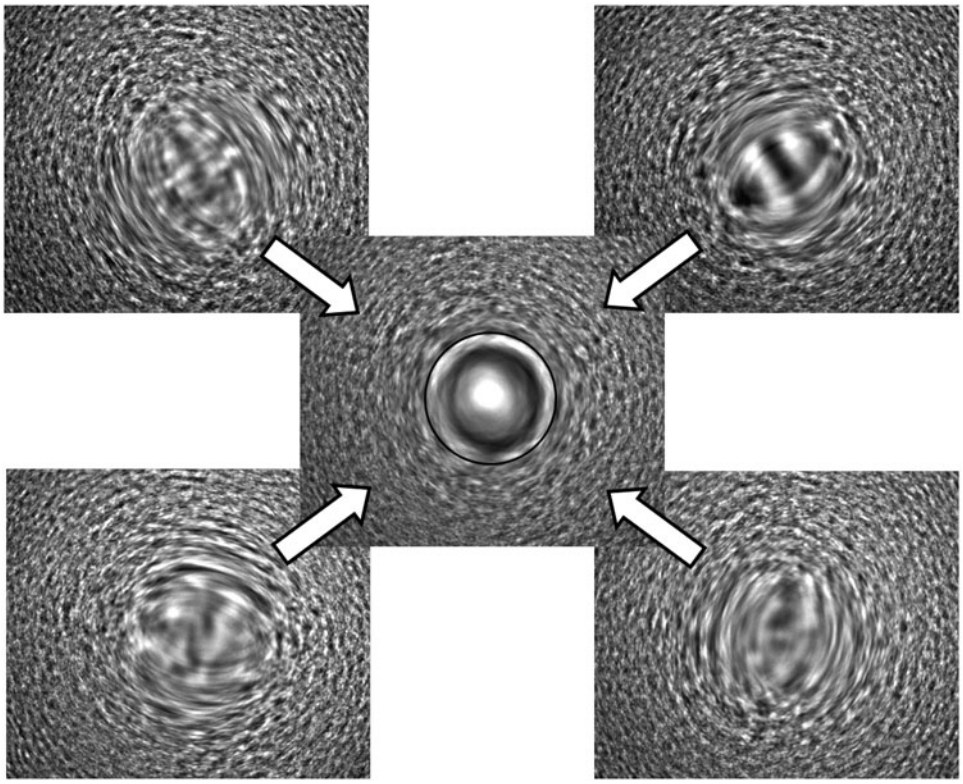

Fig. 18. A set of shadow images of an amorphous carbon film illustrates the use of shadow images to correct the astigmatism of the probe-forming lens, to find the coma-free optical axis, to determine the defocus value of the electron beam, and to auto-tune the aberration corrector settings. Reproduced from Liu (2005).

simulations (Lin & Cowley, 1986*a*, 1986*b*; Wong et al., 1992; Wang & Cowley, 1995; Ramasse & Bleloch, 2005; Yamazaki et al., 2006; Lupini & Pennycook, 2008; Kimoto & Ishizuka, 2017).

When an amorphous region is under STEM probe illumination, the angular distribution of the scattered electrons is mostly located within the transmitted disk (large or no probe-forming aperture) and diffraction beams are hardly discernible in the electron Ronchigram. When the electron beam is far out-of-focus, the projection image resembles a conventional BF TEM image of amorphous materials. As the defocus value is decreased, both the shadow-image magnification and distortion increases significantly. Explanations for these experimentally observed phenomena were discussed in detail (Cowley, 1979*a*, 1986; Lupini, 2011). The electron Ronchigram from an amorphous region provides a convenient approach to aligning STEM electron optical components, correcting for astigmatism and coma, adjusting probe defocus, and selecting/centering the probe-forming aperture (Cowley, 1979*b*; James & Browning, 1999; Dellby et al., 2001; Liu, 2005; Yamazaki et al., 2006; Fig. 18). A Ronchigram can be conveniently used to extract aberration parameters of the imaging system and/or to auto-tune the probe-forming lens system (Krivanek et al., 1999; Dellby et al., 2001; Lupini et al., 2010). By using autocorrelation function of a segmental Ronchigram to measure the aberration parameters, Sawada et al. developed a method to automatically determine lens aberrations up to the fifth order (Sawada et al., 2008). The electron Ronchigram method is extremely useful for fast searching sample regions of interest, for STEM alignment, for selecting and centering the probe-forming aperture, and for orienting crystalline specimens via the Kikuchi line method (Levine et al., 1966; Smith & Cowley, 1971).

When the probe-forming aperture allows diffraction disks to overlap, the probe may become small enough to resolve the corresponding lattice fringes in ADF images provided that lens aberrations are small enough. At each fixed probe position, the coherent CBED pattern contains all the information about the specimen. Lens aberrations, however, impose distortions on such CBED patterns (Cowley, 1984*a*, 1984*b*, 1984*c*, 1986; Lin & Cowley, 1986*a*, 1986*b*; Cowley & Ou, 1989). Without the use of aberration correctors, electron nanodiffraction patterns could be obtained using electron probes as small as 0.3 nm in diameter and such diffraction patters could be stored on a video tape at a rate of 30 patterns/s (Cowley, 1984*a*, 1984*b*, 1984*c*). Cowley proposed that by analyzing these coherent CBED patterns, which would change appreciably when the electron beam was translated by a small fraction of the probe diameter, information on the structure of the probed atoms within the electron beam with a resolution much smaller than the probe size would be obtainable. Cowley stated that a super-resolution down to 0.05 nm, with a 0.3 nm electron probe, would be achievable by properly processing the recorded nanodiffraction patterns. Theoretical calculations, via tracking the intensity of Patterson components in the nanodiffraction plane to determine the interatomic vectors corresponding to pairs of atoms under probe illumination, showed the feasibility of such an approach (Konnert & D'Antonio, 1986). Theoretical considerations and comparisons to experimental results demonstrated that an image resolution approaching 0.1 nm was achievable (Konnert et al., 1989). This approach, however, relied on having sufficient *a priori* information about the structure being examined. Although these earlier efforts demonstrated the feasibility for resolution improvement, the lack of appropriate high-quality electron detectors and data storage

Downloaded from https://www.cambridge.org/core. IP address: 68.98.49.119, on 04 Sep 2021 at 06:14:57, subject to the Cambridge Core terms of use, available at https://www.cambridge.org/core/terms. https://doi.org/10.1017/S1431927621012125

systems, faster computers, and better algorithms made such an approach not practical.

During the same time period when Cowley focused on improving image resolution via processing nanodiffraction patterns and in-line holograms (Cowley, 1979*a*, 1979*b*, 1979*c*, 1979*d*; Lin & Cowley, 1986*a*, 1986*b*; Cowley, 1990, 1992), Rodenburg emphasized extracting useful information on both crystalline and amorphous materials via analysis of nanodiffraction patterns by developing new algorithms (Rodenburg & McMullan, 1985; Rodenburg, 1988, 1989). Rodenburg and Bates (1992) published a paper on employing the Wigner-distribution deconvolution approach to achieving super-resolution. By use of the Wigner-distribution function, the instrument parameters were entirely separated from the specimen information. In theory, the extracted specimen function should possess a spatial resolution approaching the electron wavelength. The final reconstructed image was shown to be insensitive to specimen thickness and partial coherence of the electron beam, and tolerance to certain levels of noise. In this paper, the authors used the word "ptychography," following the earlier designation (Hegerl & Hoppe, 1970, 1972), to differentiate this approach from electron holography. With a TV rate CCD camera to record nanodiffraction patterns, Rodenburg and colleagues demonstrated the practicality and the feasibility of significantly improving image resolution via processing of coherent CBED (Rodenburg et al., 1993; Nellist et al., 1995). These authors were able to extract phase differences among all the neighboring pairs of diffracted beams in a coherent CBED, and an image resolution of <0.14 nm was achieved from an STEM instrument with a conventional point resolution of 0.42 nm. Further improvement in the phase retrieval algorithm made the ptychography approach more robust (Maiden & Rodenburg, 2009).

The next breakthrough in realizing significantly improved image resolution was detector development. Ideally, one desires an electron detector that possesses ultrahigh sensitivity (e.g., for low-dose applications), ultrafast speed readout, and ultrahigh dynamic range. The detector must read out fast to reduce adverse effects of sample drift, electron-beam-induced effects, and other types of disturbances. To reconstruct an image of a reasonable area of a specimen with high image resolution, the detector should possess a reasonable number of pixels (e.g., 512×512 or $1{,}024 \times 1{,}024$ pixels) and each coherent CBED should be acquired in a short time. The coupling of a scintillator with a CCD for digital readout has good electron sensitivity but suffers readout speed (about 30–60 frames/s for most applications) and has a limited dynamic range (Fan & Ellisman, 1993; De Ruijter, 1995). The development of monolithic active pixel sensors (APSs), employing complementary metal-oxide-semiconductor (CMOS) chips, made it possible to have very high sensitivity and fast readout speed (Mendis et al., 1997; McMullan et al., 2014). The disadvantage of the APS-based electron detectors is that they possess a relatively poor dynamic range. Another major advance in detector technology was the development of hybrid pixel array detector (PAD) which used arrays of photodiodes and application-specific integrated circuits (Ansari et al., 1989; Caswell et al., 2009), providing fast readout speed, high dynamic range, and single electron counting sensitivity (Tate et al., 2016).

With the use of these new types of electron detectors, robust algorithms for data processing, and faster computers, impressive results firmly established the power of ptychography approach to super-resolution imaging. For example, an image resolution of 39 pm was achieved (at 80 kV) on a 2D molybdenum disulfide (MoS_2) sample, far exceeding the conventional imaging resolution of 98 pm for these microscope parameters (Jiang et al., 2018; Fig. 19). With such an image resolution, the atomic arrangement of a crystal as well as defect structures within the crystal may become clearly discernible. The authors also conducted simulations and concluded that defocused-probe iterative ptychography outperforms both focused-probe iterative ptychography and the Wigner-distribution deconvolution method by approximately a factor of 2 in signal-to-noise improvement. The success of ptychography approach to ultrahigh-resolution imaging encouraged broad applications to solving various types of material problems (Yang et al., 2016, 2017*a*; Wang et al., 2017; dos Reis et al., 2018; Lozano et al., 2018; Fang et al., 2019).

With commercially available fast pixelated direct electron detectors, focused-probe ptychography can be routinely accomplished, although real-time ptychography is not possible yet. The high sensitivity of pixelated electron detectors makes it possible to practice low-dose electron microscopy which is critical to significantly expanding practical applications of ac-STEM to studying electron-beam-sensitive materials and systems. Determining the local atomic arrangement of complex nanostructures of electron-radiation-sensitive materials has always been a grand challenge. Generally speaking, the required illumination dose for electron optical imaging is approximately inversely proportional to the square of spatial resolution (Saxberg & Saxton, 1981). Therefore, much higher electron doses are needed to improve image resolution. For electron-beam-sensitive materials, however, higher electron doses may destroy the specimen structure before a reasonable quality image can even be acquired. Since electron ptychography utilizes the information contained in the whole diffraction pattern, it offers the possibility of extremely low-dose imaging of electron-beam-sensitive materials with atomic-resolution, rivaling that of cryo-TEM methods. It has been demonstrated that by using a mixed-state reconstruction algorithm, the mixed-state ptychographic approach could reduce electron doses by 50 times while still maintaining the image resolution and large field of view (Chen et al., 2020). With the use of a defocused electron probe, robust ptychography under low-dose conditions was realized (Song et al., 2019). Electron ptychography has significant potential for applications in structure determination of biological samples, especially when it is conducted on samples at cryogenic temperatures (Zhou et al., 2020).

The term "4D-STEM" is used to describe the collection of the whole diffraction pattern from each electron probe position over a specimen area, and the subsequent reconstruction of various types of images from the diffraction dataset (Fig. 20). In fact, as described in the section "Configured detectors for versatile STEM imaging," ideally one would like to add another dimension of data to the 4D-STEM: for each fixed probe position, each set of diffraction patterns should be recorded with a specific energy loss. The 5D-STEM dataset contains not only structure information in real and reciprocal space but also full information about inelastic scattering events in both real and momentum space. Since 4D-STEM dataset contains all structural information of the specimen virtual experiments can be performed on this dataset to yield all types of images, as discussed in the section "Configured detectors for versatile STEM imaging." In the late 1980s and early 1990s, Cowley constantly emphasized the rich information stored in each coherent CBED pattern, stored on video tapes, as he manually moved the electron probe across the sample of interest. However, the lack of high-performance electron detectors, data storage media, faster computers, and robust reconstruction

Downloaded from https://www.cambridge.org/core. IP address: 68.98.49.119, on 04 Sep 2021 at 06:14:57, subject to the Cambridge Core terms of use, available at https://www.cambridge.org/core/terms. https://doi.org/10.1017/S1431927621012125

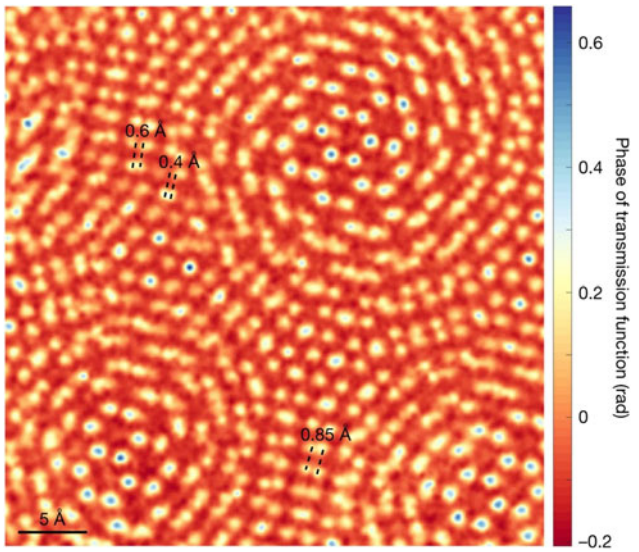

Fig. 19. Real-space resolution test of full-field ptychography using twisted bilayer MoS_2.The two sheets are rotated by 6.8° with respect to each other, and the misregistration of the molybdenum atoms provides a range of projected distances that vary from a full bond length down to complete overlap. Atoms are cleanly resolved at a separation of 85 ± 2 pm, with a small dip present between atoms separated by ~61 ± 2 pm. Atom-pair peaks at 42 ± 2 pm show a 6% dip at the midpoint, suggesting that the Sparrow limit lies just below 40 pm. The Raleigh resolution for the ADF STEM is 120 pm for these imaging conditions. Reproduced from Jiang et al. (2018).

algorithms prevented the successful implementation of his excellent ideas.

The rich information contained in a 4D-STEM dataset and its flexibility for providing various types of STEM images have made this method a preferred approach to characterizing a wide variety of materials systems including biological and soft materials. Ophus recently provided a detailed review of this technique including historical development and applications (Ophus, 2019). Since manipulation and processing of 4D-STEM datasets can provide phase-contrast, *Z*-contrast, strain-field-induced contrast, or other contrast mechanisms, and enable low-dose approach without compromising image resolution, it is expected that 4D-STEM will provide an unparalleled approach to atomic-resolution imaging of materials that previously could not be examined due to electron-beam-induced effects. With a 4D-STEM dataset, one has complete flexibility to apply a virtual mask of any shape or size to produce STEM images of interest (e.g., differential phase contrast or center-of-mass images) to extract relevant information of the specimen (Han et al., 2018; Bammes et al., 2019; Das et al., 2019; Fang et al., 2019; Gao et al., 2019; Müller-Caspary et al., 2019; Pekin et al., 2019; Wen et al., 2019; Londoño-Calderon et al., 2020; Wu et al., 2020; Mahr et al., 2021).

Quantitative Atomic-Resolution STEM Imaging

The measurement of the positions of individual atoms in materials with picometer-scale precision is required to understand the structure of surfaces, interfaces, and the various types of defects that control or influence a broad spectrum of materials behavior. X-ray-based methods can provide structural information with such a precision but are averaged over a large volume of the sample of interest. Local structural and chemical information of subnanometer- or nanometer-scale heterogeneities in a sample, however, requires much higher spatial resolution than X-ray-based techniques can provide. STEM-based imaging, spectroscopy, and diffraction techniques can provide atomic-scale information of the specimen with picometer precision provided that the various types of instrument-, specimen-, and environment-related artifacts are alleviated or completely eliminated. With the use of a modern ac-STEM instrument, sub-pm precision and standardless atom-counting with <1 atom uncertainty in STEM images of supported Pt nanoparticles have been realized (Yankovich et al., 2014). Such high-precision, atomic-resolution STEM images are critical to understanding the physicochemical properties of many nanostructured materials and systems. Precise atomic models of nanostructures and systems, based on high-precision STEM imaging, are the foundation for understanding structure–performance relationships and for designing novel nanostructures that possess unique physicochemical properties. For example, Nilsson Pingel et al. (2018), using an atomic-resolution, high-precision STEM imaging approach, experimentally measured the site-specific strain at interfaces, surfaces, and defects in Pt nanoparticles supported on alumina and ceria. These authors found that the largest strains occurred at the interfaces and were predominantly compressive. By combining the STEM measurements with first-principles kinetic Monte Carlo simulations of CO oxidation reaction, the authors concluded that the presence of only a fraction of strained surface atoms could influence the catalytic turnover frequency for CO oxidation, quantitatively demonstrating the relationship between strain and catalytic function of nanostructures and interfaces.

Correction of Image Distortions and Structural Measurement with Picometer Precision

Unlike parallel imaging systems (e.g., TEM), the formation of a scanning probe microscopy (e.g., STEM) image requires movement of a fine probe across a sample surface in order to form an image. This procedure can introduce various types of artifacts in the image due to the time delay between the signal measurements and the accumulative error in the probe position with respect to the specimen. Examples of such artifacts include linear distortions, random "jitter" of probe position due to various types of interferences, jump discontinuities due to sample instability, random drifting of specimen, and so on. All scanning probe images contain distortions and these distortions are frequently much larger than the atomic-scale features of interest. During the early periods of STEM development, image distortions due to environmental factors could become so severe that crystal lattice fringes looked like random waves in the recorded images. The imaging distortions may originate from mechanical and/or acoustic vibrations, instabilities in power supplies for the lenses or alignment coils, electric/magnetic fields within and/or around the microscope column, computer fans, and so on. In addition to disturbances due to environmental (acoustic, mechanical, and/or electromagnetic) factors, many instrumental factors also affect the accurate measurement of fine structures in an STEM image (von Harrach, 1995). For atomic-resolution STEM imaging, different parts in a recorded image may be distorted differently and image features may appear "torn" (feature rows shift horizontally), "sliced" (feature rows shift vertically), or "sheared" (image features elongate). The designs of modern ac-STEM instruments have been significantly improved with the goal of reducing the effects of instrument factors on image resolution. The ac-STEM instrument, especially in the shadow-image mode, is the most sensitive device to evaluate microscope- and building-related instabilities. As the spatial resolution of an STEM instrument improved, its

Downloaded from https://www.cambridge.org/core. IP address: 68.98.49.119, on 04 Sep 2021 at 06:14:57, subject to the Cambridge Core terms of use, available at https://www.cambridge.org/core/terms. https://doi.org/10.1017/S1431927621012125

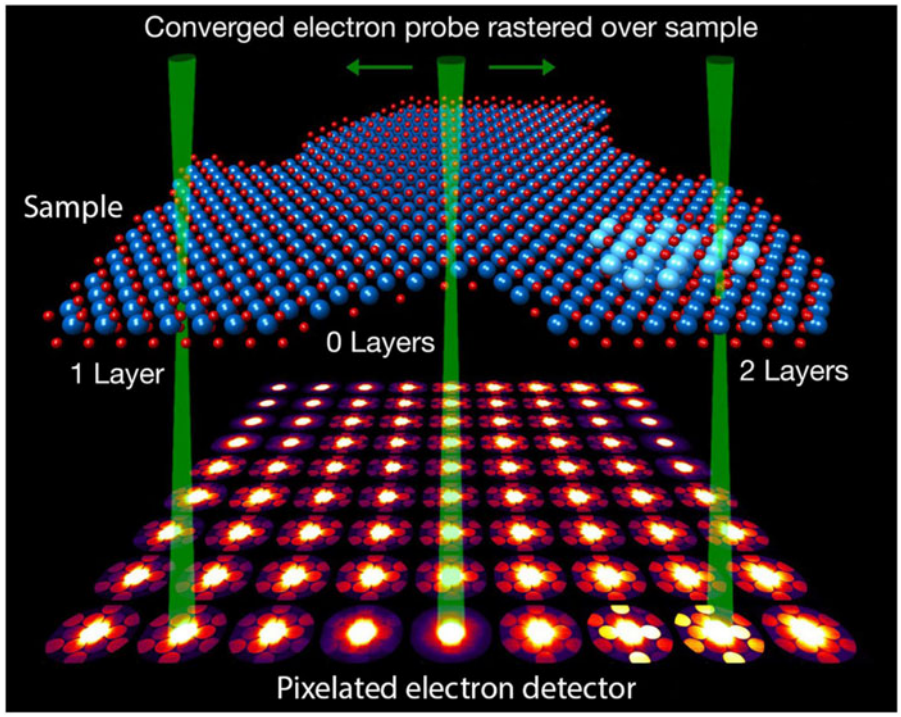

Fig. 20. Experimental 4D-STEM measurement of a dichalcogenide 2D material. The various types of real-space atomic-resolution images can be reconstructed from the diffraction dataset; each diffraction pattern represents an average of 7 × 7 experimental images. Green STEM probes are labeled for regions of the sample with one layer, vacuum, and two layers. The total dataset was acquired in 164 s and contains 420 GB data. The high-speed and efficient direct electron detectors, and the readily available computational power enable such experiments possible. Reproduced from Ophus (2019).

sensitivity to room environment became more noticeable and posed a severe limitation to achieving the microscope's high-resolution capabilities. Room design to reduce external interferences became an integral part of a successful installation of an ac-STEM with desired performances. Quantitative characterization of an STEM's response to magnetic, mechanical, acoustical, and thermal disturbances was discussed (Muller et al., 2006).

An approach to recovering a nondistorted STEM image is correction of scanning distortion with the goal of maintaining accuracy and resolution of the STEM images of interest. Such a post-processing approach proved to be extremely successful in significantly increasing the measurement precision of structural parameters to the picometer scale. Rečnik et al. (2005) used CTEM images as references to correct the corresponding STEM images. This method was applied to extracting compositional atomic-column data from HAADF-STEM images of crystals with local occupancy or chemistry fluctuations, stacking faults, special grain boundaries, or interfaces. Such an image-warp method, however, needs an available structural model. Sanchez et al. (2006) developed an algorithm for correcting time-invariant image distortions such as hysteresis effects during "fly back" between scan lines or systematic beam deflections due to external electromagnetic fields. They further successfully applied this method for local strain mapping of heterostructures. Braidy et al. (2012) proposed a method, based on phase analysis of streaks in Fourier space, for analyzing and subsequently correcting systematic row displacement errors in STEM images of periodic structures. Jones and Nellist (2013) investigated the sources, nature, and effects of imaging distortions and developed an image reconstruction code to restore the majority of detrimental distortion effects on atomic-resolution data. The image restoration protocol was developed on the assumption that the image drift rate and direction during the image acquisition process were constant. In addition to correcting image drift effects, these authors improved image resolution as well as the signal-to-noise ratio. Based on a real-space template matching technique, Zuo et al. (2014) developed a quantitative lattice analysis and a scanning distortion-correction protocol. This method uses the template of an atomic column or a group of atomic columns to transform the image into a lattice of correlation peaks. A reference lattice, however, is needed to correct for scan noise and scan distortions in the recorded images.

Berkels et al. (2014) proposed a methodology, based on a nonrigid pixel-wise registration method to cope with low signal-to-noise ratios in scanning images, for extracting useful information from a series of STEM images. The success of this strategy is based on: (1) replacing single-frame high-dose data acquisition by several low-dose short exposure frames and (2) properly synthesizing the information from such a series of frames by a novel cascading registration methodology. The multilevel nonrigid registration method, which accurately links the information carried by many sequentially acquired low-dose frames, is the essence of this proposed protocol. The authors applied quantitative objective-quality measures to illustrate the effectiveness of the proposed procedures and successfully applied the method to extract structural information on electron-beam-sensitive siliceous zeolite materials. Sang & LeBeau (2014) developed a protocol called RevSTEM to remove sample drift distortion from atomic-resolution images without the need for *a priori* crystal structure information. To measure and correct the distortion, a series of fast-acquisition STEM images with rotated scan coordinates need to be acquired. These authors demonstrated that the RevSTEM protocol simultaneously removed the need for *a priori* structure information to correct distortion, leading to a dramatically

Downloaded from https://www.cambridge.org/core. IP address: 68.98.49.119, on 04 Sep 2021 at 06:14:57, subject to the Cambridge Core terms of use, available at https://www.cambridge.org/core/terms. https://doi.org/10.1017/S1431927621012125

improved signal-to-noise ratio, and enabling picometer precision and accuracy regardless of a drift rate. Yankovich et al. (2014) developed a successful scheme, based on nonrigid registration and averaging over an image series, to achieve extremely high signal-to-noise ratio (SNR) STEM images, providing sub-pm precision in structure measurement and standardless atom-counting with <1 atom uncertainty in STEM images. The authors proved that the nonrigid registration approach achieved five to seven times better precision than the previous image distortion-correction approaches. Berkels & Liebscher (2019) reported a novel bias-corrected nonrigid registration approach that compensated for both fast and slow scan artifacts in STEM image series. The bias-correction method allows to reduce fast scan noise in an image series and slow scan distortions simultaneously. Such an image-correction process may have applications in atomic-resolution strain and elemental mapping.

During an STEM experiment, many types of samples may be sensitive to electron-beam-irradiation effects (Egerton et al., 2004; Egerton, 2013, 2019). Therefore, the use of low electron doses and as few measurements as possible to correct image distortions are highly desirable. With this expectation, Ophus et al. (2016*a*) designed a procedure to correct linear and nonlinear distortions by using orthogonal scan pairs to align each measurement line-by-line along the slow scan direction and fitting the contrast variations along the lines. The algorithm requires no *a priori* assumptions about image features and requires only two images as an input, minimizing acquisition time and electron dose. Bárcena-González et al. (2020) further proposed a CDrift algorithm for correcting linear drift from a single atomic-resolution STEM image. This method is based on angle measurements in the Fourier space and an iterative algorithm, based on successive rotation/drift correction steps, is required to remove drift distortions in atomic-resolution STEM images. The general applicability and robustness of this approach need to be evaluated and validated.

When the scanlines are misaligned, distortions occur that degrade the accuracy and precision of which a modern ac-STEM can provide. In general, the slow scan direction is more prone to various types of disturbances. Alternative scanning paths to form images may be used to reduce image distortions. Spiral scanning paths were investigated as an alternative approach to acquiring images at extremely high speed (Sang et al., 2016, 2017). Different scans with constant angular and linear velocity spirals were evaluated. These exotic scanning methods suffer nonuniform image quality over the scanned area. The sparse acquisition approach, with a goal of reducing electron dose/dose rate to a sample during imaging, can be employed to either alleviate image distortions or to significantly reduce electron dose and/or acquisition time (Kovarik et al., 2016). Other scanning approaches such as "snake" patterning, where the scan direction is reversed after each row, and Hilbert scan patterning that changes scan direction rapidly, were proposed and evaluated (Velazco et al., 2020). The authors demonstrated that the Hilbert scan patterning approach possessed certain advantages for faithfully representing the high-frequency content in an image in the presence of sample drift. Compared with the conventional raster scan with fly-back correction, both the "snake" and Hilbert scanning approach may reduce the required electron dose for similar quality of STEM images.

Quantification of STEM Image Intensities

Qualitative matching between simulated and experimental atomic-resolution images is routine practice with the goal of distinguishing material structures. To fully extract structural and chemical information, such as the number and types of atoms and the precise positions of each atomic species in the specimen of interest, however, requires quantitative comparisons between simulated and experimental STEM images. Since the HAADF signal carries both structural and chemical information of the probed area, it is expected that quantitative analysis of contrast variations and peak intensities in HAADF images may provide atomic-scale information for understanding and establishing structure–performance relationships (Klenov & Stemmer, 2006; Klenov et al., 2007).

Size Determination of Metal Clusters and Particles via Intensity Quantification

In examining heavy metal nanoparticles in supported metal catalysts, Treacy & Rice (1989) developed a method to determine the size of small metal particles by quantitatively evaluating the total intensity of a particle in an HAADF-STEM image. They showed that the number of atoms in a small metal cluster could be estimated from the HAADF signal strength and demonstrated that the method would be particularly useful for detecting and measuring particles in the subnanometer size range. The integrated particle intensity was proposed to be proportional to the number of atoms probed by the electron beam, weighted by their individual scattering cross-sections. They further verified, using experimental data, that a straight line would result when the square root of the imaged area ($A^{1/2}$) was plotted against the cubic root of intensity ($I^{1/3}$). Such plots provide the calibration of the intensity increment per atom without the need of external calibration. A high signal-to-noise ratio and optimum sampling of the specimen are highly desirable for this method to work. By using such an integrated intensity approach, the authors reliably detected Pt clusters of only three atoms even though the STEM probe size was ~0.35 nm. Such a method was applied to quantitative measurement of small Re particles and clusters (Singhal et al., 1997). Statistical measurement of absolute cross-sections of Re-6 clusters showed good agreement with theoretical cross-sections, within a ±2 atom random error. To reduce errors in quantitative measurement, the authors calibrated their ADF detector and paid special attention to reducing the sources of error in absolute intensity measurements. The authors speculated on the possibility of single-atom sensitivity and named this quantification method as STEM-based mass spectroscopy. Yang et al. (2000) developed a computer program to automatically find the locations of metal clusters in HAADF images and then to integrate the HAADF intensity of each cluster, leading to the determination of the number of atoms in each cluster. The use of automated analysis of image intensities made the STEM mass-spectroscopic technique statistically meaningful and robust. By analyzing the particle area–intensity relationships, the 3D shapes of small metal particles and clusters may be inferred (Treacy & Rice, 1989). Young et al. (2008), using size-selected nanoclusters as mass standards, quantified the masses and 3D shapes of supported metal nanoparticles. Through quantitative image intensity analysis, the authors found that the HAADF intensity displays a monotonic dependence on cluster size, even for as many as 6,500 atoms of Au supported on carbon, significantly extending the applicability of the STEM mass-spectrometry method.

Quantitative Atomic-Resolution STEM Imaging and Atom-Counting

In addition to correcting for image distortions, a quantitative evaluation of STEM images requires analysis of contrast

Downloaded from https://www.cambridge.org/core. IP address: 68.98.49.119, on 04 Sep 2021 at 06:14:57, subject to the Cambridge Core terms of use, available at https://www.cambridge.org/core/terms. https://doi.org/10.1017/S1431927621012125

variations, measurement of atom positions and peak intensities, and comparisons to calculations. The collected ADF signal, for example, may include Rutherford-scattered electrons, phonon-scattered electrons, electrons scattered by various types of defects, and inelastically scattered electrons. Further considerations in image simulations need to account for detector size, shape, and pixel response; specimen orientation, effects of amorphous layers and strain field; source size broadening and partial coherence; and electron optical parameters (probe size, convergence angle, electron energy, lens aberrations, defocus value, etc.). Among all the imaging modes available in an STEM instrument, the highly intuitive HAADF imaging mode is of special interest because it provides high chemical sensitivity with ultimate spatial resolution. The experimentally measured image intensity of an HAADF image is a function of atomic number and the number of atoms covered by the incident electron probe. A quantitative interpretation of this intensity requires an external calibration. If the intensities of experimental images are normalized with respect to the incident beam intensity, then a direct comparison with simulated images becomes meaningful (LeBeau & Stemmer, 2008; LeBeau et al., 2008, 2009*a*, 2009*b*; Rosenauer et al., 2009, 2011; Grieb et al., 2012).

Since the image contrast of ADF images depends sensitively on detector configurations, one should have a full understanding of the detector response function in order to reduce the degree of discrepancy between experimental and simulated images (LeBeau & Stemmer, 2008; Grillo, 2009*a*, 2009*b*; Rosenauer et al., 2009). Experimentally, one can simply scan an STEM probe over the ADF detector to obtain a response map and quantitatively evaluate the response function of each pixel by displaying its pixel intensity. For a standard ADF detector, Findlay & LeBeau (2013) attributed errors in image contrast of about 10% or more to the nonhomogeneous detector response, a nontrivial error for quantitative STEM. In addition to a full characterization of the detector response function, the authors discussed detector response normalization and how such a response function might be incorporated into image simulations for quantitative STEM. MacArthur et al. (2014) evaluated ADF detectors from various manufacturers by forming detector maps and found various types of asymmetries and nonuniformities in their response to high-energy electrons. The detector response at smaller scattering angles varied significantly from that at higher angles which could significantly modify ADF image contrast, especially for images obtained with small inner collection angles. The asymmetry of the detector response function may impose a distortion of the observed image contrast and probably introduce spurious image contrast due to the nonuniform detector response function. Incorporation of a detector sensitivity map into image simulations significantly reduced contrast discrepancies between experimentally acquired and simulated images (Rosenauer et al., 2011; Mehrtens et al., 2013; Martinez et al., 2014). Alternatively, one can use an effective scattering angle in simulated images to compensate for inhomogeneous response of a detector (Findlay & LeBeau, 2013). Since the quantification procedure becomes specific to each instrument and each experimental setting, extensive computation is required and one would not be able to compare results obtained on different instruments, posing a major limitation on practical applications of this approach.

A simulation-free approach was proposed to quantify ADF STEM images—the statistical parameter estimation theory (den Dekker et al., 2005, 2013; Van Aert et al., 2005, 2009, 2011, 2012, 2013; De Backer et al., 2016). These authors developed a statistical parameter estimation theory to construct an empirical incoherent imaging model to fit an experimental image. The goodness-of-fit approach was used as a criterion to evaluate the proposed model. From these estimated parameters, the scattering cross-sections of atomic columns could be obtained (Van Aert et al., 2009). Such a probe position integrated cross-section (PICS) for a single column of atoms provides an effective way to compare simulation and experimental HAADF images and was tested to be robust to parameters that affect probe size and shape such as defocus and source coherence (MacArthur et al., 2013). With such a quantification approach, the main imaging parameters are detector angle and electron beam voltage. It was demonstrated that the PICS approach could be applied to chemical identification of single atoms in a heterogeneous catalyst (MacArthur et al., 2013). This statistics-based model approach demonstrated sensitivity to chemical composition (Van Aert et al., 2009; Martinez et al., 2014) and the number of atoms under the probe illumination with single-atom sensitivity (Van Aert et al., 2011, 2013; De Backer et al., 2013). The effects of probe inaccuracies and electron dose on the statistics model-based analysis of HAADF images were evaluated and discussed (Martinez et al., 2013; De Backer et al., 2015). The atom counting method was applied to examining the 3D morphology of Pt nanoparticles and the results seemed to be better than the conventional tomographic approach (Altantzis et al., 2019; Fig. 21).

The atom-counting method discussed above was applied to investigating hetero-atom nanostructures by extending the above method to the atomic lensing model (van den Bos et al., 2016, 2019). This new approach allows an identification of scattering cross-section of mixed columns that possess 3D arrangements of different atoms. By taking nonlinear scattering cross-sections into account, via the assumption that dynamical diffraction effects could be considered as a superposition of individual atomic focusers, the authors demonstrated that the lensing effect of an atom was independent of defocus. Through such model-based calculations, intensities of columns of mixed atoms would be predicted, leading to differentiation of atomic columns with different degrees of atom mixing. The combination of the statistical parameter estimation with model-order selection proved to be useful for establishing maximum *a posteriori* (MAP) probability rule (Fatermans et al., 2018, 2019) which would allow structural determination of unknown structures in an automatic and objective manner and determination of atomic columns with high reliability and single-atom sensitivity. The MAP rule was extended to simultaneously acquired ABF and ADF images, enabling structural determination of both light and heavy elements in a crystalline sample (Fatermans et al., 2020). It is expected that such modeling processes are not limited to ADF and ABF detector configurations but may be extended to model-based analysis of all STEM imaging modes including 4D-STEM.

Atomic-Resolution Three-Dimensional Imaging and Elemental Mapping

Atomic-Resolution Electron Tomography

Understanding material properties and functionalities at the most fundamental level requires precise measurement of 3D positions of atoms with picometer or sub-picometer precision. Practical materials often contain surfaces/interfaces, defects, and/or nanoscale heterogeneities which can strongly influence their properties and performance. The 2D projection images that we discussed above do not fully represent the underlying 3D structures and

Downloaded from https://www.cambridge.org/core. IP address: 68.98.49.119, on 04 Sep 2021 at 06:14:57, subject to the Cambridge Core terms of use, available at https://www.cambridge.org/core/terms. https://doi.org/10.1017/S1431927621012125

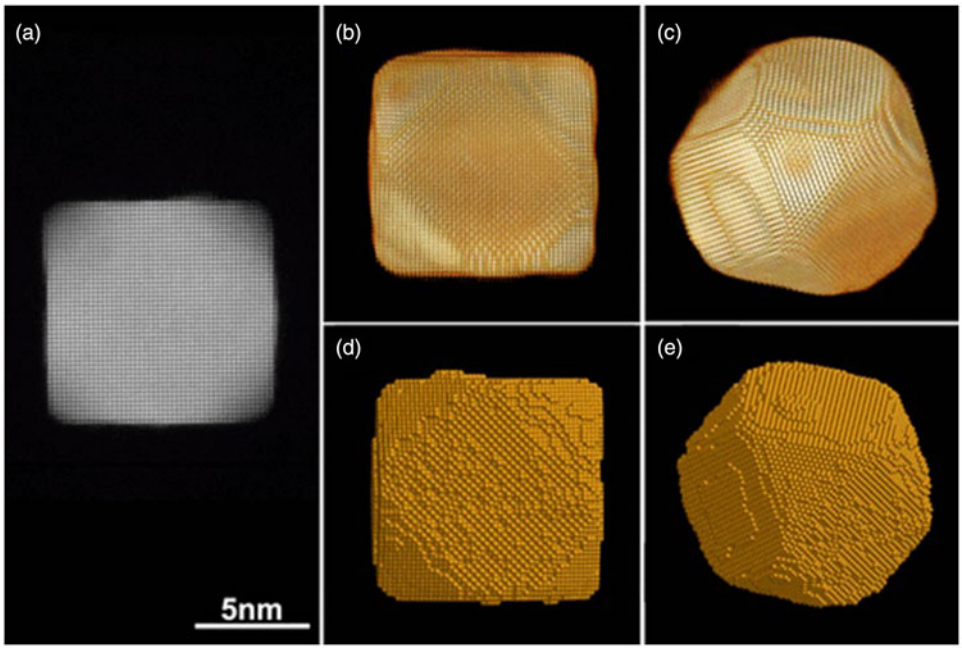

Fig. 21. Comparison of the 3D shapes obtained by the reconstruction of a high-resolution tomography series and by atom-counting, for the same Pt NP. (**a**) High-resolution HAADF STEM image of a Pt NP which was used for conventional high-resolution electron tomography and for atom-counting and relaxation. (**b**,**c**) Three-dimensional visualization of the reconstructed volume obtained by conventional high-resolution tomography, along different viewing directions. (**d**, **e**) Three-dimensional models of the same Pt NP obtained by using atom-counting and relaxation. Reproduced from Altantzis et al. (2019).

can lead to significant errors in assessing the true 3D structures of the specimen of interest. The tomographic approach is used for revealing hidden structures that are not directly accessible by 2D projection images. Radon mathematically worked out how to project a high-dimension object into a lower-dimension space (Radon, 1917). The inverse function of the Radon transform provides the mathematical foundation of tomographic techniques. Electron tomography, developed in the late 1960s (De Rosier & Klug, 1968), was successfully applied to imaging 3D structures of biological specimens at cryogenic temperatures (Unwin & Henderson, 1975; Dubochet et al., 1988). The method developed for biological specimens, however, may not be directly applicable for materials science applications. In biological and noncrystalline inorganic systems, the use of BF TEM imaging is appropriate because the mass-thickness contrast satisfies the "projection requirement" that the recorded signal should be a monotonic function of some physical property (Hawkes, 1992). If this requirement is not satisfied, then 3D reconstruction becomes too complicated and conventional real-space, back-projection method may not be approachable. For investigation of crystalline materials, the presence of diffraction contrast and Fresnel fringes in TEM images fails the projection requirement and can lead to serious artifacts in 3D reconstructions. The unique characteristics of the HAADF-STEM signal are, however, appropriate for tomographic imaging of crystalline materials provided that electron-beam-induced effects are alleviated or eliminated. The early development and applications of electron tomography in materials science have been reviewed (Midgley & Weyland, 2003; Midgley & Dunin-Borkowski, 2009).

Since incoherent ADF STEM imaging substantially suppresses the diffraction and phase contrast of crystalline regions of the sample and yields atomic number sensitivity with sub-Ångstrom spatial resolution, this imaging mode is particularly suited for achieving atomic-resolution tomography (Miao et al., 2016) (Fig. 22). The missing wedge problem can be overcome by using needle-shaped specimens, allowing a 360° rotation around the needle axis (Xu et al., 2015). Another problem in STEM tomography is electron-beam-induced effects on the specimen. Since many images of the same specimen region are required for atomic-resolution STEM tomography, electron-beam-induced damage to the specimen may become a major issue, especially for studies of electron-beam-sensitive materials. Appropriate electron energies need to be selected to reduce knock-on damage (Egerton et al., 2004, 2010). A dose-efficient STEM approach (Ophus et al., 2016*b*), employment of direct electron detectors (McMullan et al., 2014; Tate et al., 2016), and low-exposure acquisition scheme (Scott et al., 2012; Chen et al., 2013) all help alleviate electron-beam-induced effects. As discussed in the section "Correction of image distortions and structural measurement with picometer precision," various types of image distortions in each ADF STEM image of a tilt series should be corrected by the corresponding approaches and robust reconstruction algorithms should be used. Since as low dose of electrons as possible is highly desired to alleviate electron-beam effects, de-noising algorithms were developed and applied to improving image quality (Dabov et al., 2007). The center-of-mass method was applied to aligning tilt series of STEM imaging stacks (Scott et al., 2012). To achieve higher precision in defining atom positions, iterative refinement in image alignment should be implemented by initially computing a 3D reconstruction from the coarse-aligned tilt series. Then, the back-projected 2D image series, obtained from the initially reconstructed 3D image, are compared with the corresponding experimental 2D images of the same tilt angles to check for consistence. Quantitative comparison of the calculated and measured images and iterative algorithms allow fine-tuning of the reconstructed 3D image so that all the projected images match the experimental data.

In addition to establishing robust experimental protocols for atomic-resolution tomography, iterative tomographic reconstruction algorithms play the most critical role in achieving the desired

Downloaded from https://www.cambridge.org/core. IP address: 68.98.49.119, on 04 Sep 2021 at 06:14:57, subject to the Cambridge Core terms of use, available at https://www.cambridge.org/core/terms. https://doi.org/10.1017/S1431927621012125

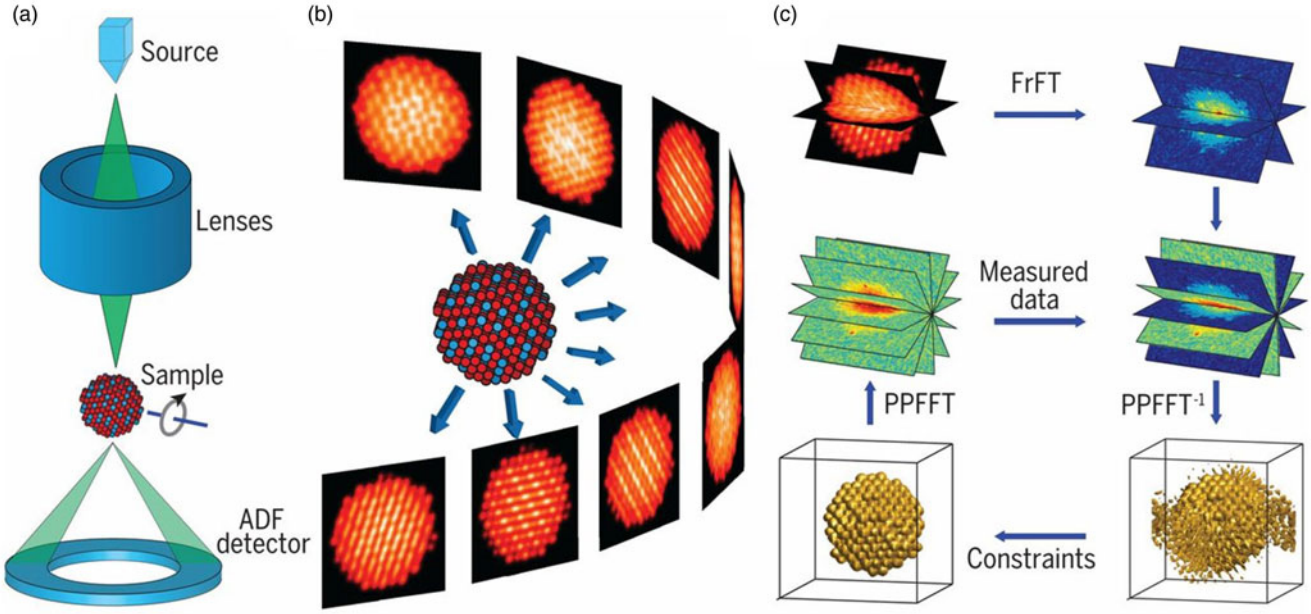

Fig. 22. Schematic illustration of an atomic-resolution electron tomography experiment. (**a**) An electron beam is focused on a small spot and scanned over a sample to form a 2D ADF image. (**b**) By rotating the sample around a tilt axis, a series of 2D ADF images is recorded at different tilt angles. (**c**) After preprocessing and alignment, the tilt series image dataset is inverted to Fourier slices by fractional Fourier transform (FrFT). A 3D reconstruction is computed by using an iterative algorithm based on pseudopopular fast Fourier (PPFFT). From the 3D reconstruction, the coordinates of individual atoms are traced and refined to produce the 3D atomic model of the specimen. Reproduced from Miao et al. (2016).

3D precision measurement. Real-space iterative algorithms compute a 3D reconstruction by iteratively solving a system of linear equations, in which positivity and mathematical regularization can be incorporated as constraints to reduce artifacts (Gordon et al., 1970; Gilbert, 1972; Andersen & Kak, 1984). The hybrid space algorithms rely on iterations between real and Fourier space. From an aligned tilt series, each image is inverted to a Fourier representation by fractional Fourier transform (Bailey & Swarztrauber, 1991). Detailed descriptions of the reconstruction algorithm with equal-slope tomography were described by Mao et al. (2010). Quantitative comparison with experimental data suggested that the equal-slope approach produced 3D reconstructions with higher resolution, better image contrast, and less distortion than real-space iterative algorithms. This approach, however, requires that the experimental tilt angles must be consistent with equal-slope increments (Miao et al., 2005).

By fitting atoms rigidly onto a crystal lattice, discrete tomography was developed to image the 3D atomic structure of a metal nanoparticle (Van Aert et al., 2011). Compressed sensing technique was applied to electron tomography with the expectation to significantly reduce electron-beam-induced effects and image distortions by sparse sampling (Leary et al., 2013). The compressed sensing electron tomography method was successfully applied to imaging localized surface plasmon resonances of a silver nanocube, providing atomic-scale information (Nicoletti et al., 2013). A design of sparse sampling domains and choice of adjustable parameters may prove challenging for noisy images (Leary et al., 2013).

The atomic-resolution tomography technique proved to be valuable for determining 3D structures of metal nanoparticles. Volume and iso-surface renderings of the 3D reconstruction of an Au nanoparticle showed the coordinates of individual surface atoms as well as the internal structures of the multiply-twinned Au icosahedral nanoparticle (Scott et al., 2012). In studying crystal defects in metal nanoparticles, Chen et al. (2013) investigated the internal 3D structure of Pt nanoparticles, revealing 3D atomic arrangements of screw dislocations and atomic steps at Pt twin boundaries. They further deduced that a strain relaxation mechanism was associated with multiply-twinned Pt decahedral nanoparticles. Such insights into the formation of crystal defects might not be extracted from conventional 2D projection images. By using a tungsten needle sample, Xu et al. (2015) conducted 3D measurements of individual atom coordinates, atomic displacements, and strain tensor parameters. By selecting nonchanneling conditions to minimize electron dynamical scattering effects and by measuring many images at various sample orientations, the authors were able to determine the coordinates of 3,769 individual atoms of the tungsten needle with a precision of about 10.5, 15, and 5.5 pm along the *x*-, *y*-, and *z*-axis, respectively. Such an approach enables 3D identification and localization of point defects in materials with high precision and without any prior knowledge. By comparing the coordinates of individual atoms with a model tungsten crystal lattice, the atomic displacement field and the strain tensor of the tungsten needle were determined. The ability of precisely determining 3D positions of individual atoms of nanostructures opens the door toward directly investigating the properties and functionalities of a plethora of nanoscale structures, systems, or devices.

Many nanostructures contain different types of elements, for example, bimetallic or multi-metallic alloy nanoparticles. Correlating the 3D atomic arrangements of chemical order/disorder and crystal defects with material properties becomes critical for designing nanostructured functional materials, especially when the structural data are combined with first-principles calculations. Yang et al. (2017*b*) determined the 3D coordinates of 6,569 iron and 16,627 platinum atoms in an iron–platinum nanoparticle, and correlated the chemical order/disorder and crystal defects with material properties at the single-atom level. They identified atomic composition, grain boundaries, anti-phase

Downloaded from https://www.cambridge.org/core. IP address: 68.98.49.119, on 04 Sep 2021 at 06:14:57, subject to the Cambridge Core terms of use, available at https://www.cambridge.org/core/terms. https://doi.org/10.1017/S1431927621012125

boundaries, anti-site point defects, and swap defects in 3D with a precision of ~20 pm. By using such structural and compositional information as direct input for DFT calculations, the authors were able to determine material properties such as atomic spin and orbital magnetic moments and local magneto-crystalline anisotropy, significantly advancing the fundamental understanding of structure–property relationships.

In polycrystalline materials, especially nanocrystalline materials, grain boundary (GB) structures and chemistry often play the most important role in determining materials properties. Design and engineering of GBs offer a route to developing nanostructured materials with novel properties. Atomic-resolution electron tomography proved to be valuable for extracting 3D atomic coordinates of general high-angle GBs (Wang et al., 2020). With atomic-resolution 3D imaging, the authors found that high-angle GBs completely lose translational symmetry due to undulated curvature related to the configurations of the structural units. Kinks and jogs at single-atom scale in dislocation-type GBs and their mobility were directly visualized in 3D at atomic resolution. Such understanding of GBs may bring deep insights into the understanding of GB behavior and in developing new material systems with desirable properties that are controlled by specific types of GBs.

Experimental investigation of dynamic events such as nucleation of clusters/nanoparticles or melting of nanocrystals faces significant challenges, especially when atomic-resolution 3D imaging of such dynamic events is required. By using an identical location STEM approach, Zhou et al. (2019) were able to evaluate nucleation processes of FePt nanoparticles in 3D. They captured the atomic-scale structure and dynamics of the same nuclei undergoing growth, fluctuation, dissolution, merging, and/or division, all of which are regulated by the order parameter distribution and its gradient. They further discovered that the early-stage nucleation process might not follow the classical nucleation theory. It is expected that with further improvement in methodology atomic-resolution 3D imaging with time resolution will provide new routes to understanding the fundamentals of phase transition, atomic diffusion, grain boundary dynamics, interface motion, defect dynamics, and surface reconstructions of nanoscale structures and systems. The atomic-resolution tomography method proved to be extremely powerful for studying 2D nanostructures with the goal of correlating their electronic, optical and chemical properties to 3D atomic positions of various elements and/or defects such as dopants and vacancies. Tian et al. (2020) determined the 3D atomic positions of Re-doped MoS_2 with a precision of ~4 pm. They measured the 3D bond distortion and local strain tensor, caused by the presence of dopant atoms. By using such 3D atomic coordinates of all the entities in the specimen as input for DFT calculations, the authors claimed to obtain more accurate electronic band structures, confirming direct correlation of 3D atomic structure to electronic properties.

As discussed in the section "Nanodiffraction, Ronchigram, ptychography, and 4D-STEM," electron ptychography efficiently utilizes scattered electrons to construct ultrahigh-resolution images and enables low-dose STEM imaging with sub-Ångstrom resolution. Atomic electron tomography, on the other hand, permits 3D imaging but requires relatively longer time of electron-beam irradiation of the specimen region of interest. Therefore, the combination of ultrahigh-resolution electron ptychography with atomic electron tomography may provide an effective approach to low-dose 3D imaging of both light and heavy elements in a crystalline specimen. Chang et al. (2020) applied this approach to the study of ZnO nanoparticles and WS_2/WSe_2 heterostructures. Since electron ptychography already requires 4D datasets and atomic electron tomography requires a series of tilt images, the data analysis algorithm becomes extremely critical to such experiments. The authors, however, determined the 3D atomic coordinates of individual zinc and oxygen atoms as well as defects within the ZnO nanoparticles. By comparing with image simulations, the authors resolved every layer, including the lightest sulfur layer, of the vertical WS_2/WSe_2 van der Waals heterostructure with atomic resolution. It is expected that with faster computers and robust reconstruction algorithms the ptychography-based atomic electron tomography may become a routinely accessible method for determining precise 3D atomic structures of radiation-sensitive systems and a plethora of practical materials such as catalysts, functional oxides, and glasses.

Atomic-Resolution STEM Depth Sectioning

Optical-sectioning microscopy, for example, achieved on a laser scanning confocal microscope, is a powerful technique for visualizing 3D structures of biological systems (Conchello & Lichtman, 2005). With the use of a large probe-forming aperture to form a sub-Ångstrom probe in an ac-STEM, the depth of field (DOF) should be significantly reduced, enabling depth sectioning meaningful by recording a series of images at different defocus values. In principle, similar to optical-sectioning microscopy, 3D images would be reconstructed from such a series of 2D projection images. A significant difference from confocal optical microscopy is that STEM imaging does not use a collection pin-hole, leading to degradation of depth sensitivity. Compared with tomography, the optical-sectioning process does not require specimen tilt, drastically reducing experimental complexity. This STEM sectioning technique, however, had not been frequently used prior to the ready availability of atomic-resolution *Z*-contrast imaging. The detection of individual Sb-dopant atoms within a crystalline Si by ADF STEM imaging (Voyles et al., 2002) invited the question on 3D localization of individual dopant atoms by a direct imaging technique. van Benthem et al. (2005) evaluated the optical-sectioning method with ADF signal (with a probe size of ~0.1 nm) to localize individual Hf atoms within an SiO_2 passivating layer of an $HfO_2/SiO_2/Si$ alternative gate dielectric stack. By acquiring a through-focal series of images, the 3D locations of dopant atoms within a crystal were realized with a lateral resolution <0.1 nm and a depth resolution of ~0.5 nm. The authors concluded that the through-focal series method was sensitive to detecting individual dopant/impurity atoms and proposed that the depth sectioning method would be applicable to spectroscopy experiments as well.

Borisevich et al. (2006) provided an evaluation of STEM depth sectioning approach, examined the resolution and contrast parameters, and demonstrated how 3D datasets could be collected and analyzed for several test systems including supported metal catalysts. The authors were able to localize nanometer-size particles and even single atoms. They conducted statistical analysis of the acquired dataset and quantified the effective focal depth, controlled by the size of the probe-forming aperture, sample parameters, signal-to-noise ratio, and image acquisition settings. By using a highly convergent electron probe, Ruben et al. (2012) investigated the depth-related features of layered heterostructures. The authors fixed the electron probe at an atomic column and monitored the variations in ADF signal strength with probe defocus. The authors were able to identify intensity peaks that were related to the heterojunctions and crystal surfaces,

Downloaded from https://www.cambridge.org/core. IP address: 68.98.49.119, on 04 Sep 2021 at 06:14:57, subject to the Cambridge Core terms of use, available at https://www.cambridge.org/core/terms. https://doi.org/10.1017/S1431927621012125

leading to an estimate of sample thickness and heterojunction locations. Channeling of incident electrons along atomic columns plays an important role, leading to reduced depth resolution. These authors demonstrated localization of crystal-vacuum surfaces to within 1 nm and buried interfaces to within 2 nm. Ishikawa et al. (2015) theoretically evaluated imaging of top/subsurface atomic structures and were able to identify depth location of single dopants, single vacancies, and other types of point defects by large-angle illumination STEM imaging. They proposed a method to measure specimen properties such as thickness or three-dimensional surface morphology using observations from a single crystallographic orientation. Imaging atomic displacements in screw dislocations are challenging because the associated atoms are predominantly displaced parallel to the dislocation line; screw displacements are parallel to the electron beam and become invisible when viewed end-on. By using the ADF sectioning approach, Yang et al. (2015) directly imaged screw displacements with the dislocation lying in a plane transverse to the electron beam. The authors reported direct imaging of a screw dissociation with a 1.65-nm dissociation distance in GaN, demonstrating an alternative approach to characterizing dislocation core structures.

Xin & Muller (2009) investigated the contrast transfer function of the ADF depth sectioning approach and found a missing-cone problem, similar to that of tilt-series tomography. They worked out the dependence of the elongation on the probe-forming convergence angle. The large elongation factor along the incident beam direction results in highly distorted shapes of 3D objects and unexpected artifacts due to loss of information. The authors further experimentally investigated the elongation effect and the missing-cone problem in real and reciprocal space. The performance limits of different S/TEM-based imaging modes were compared. Nellist (2017) discussed the contrast transfer function for 3D imaging, investigated the elongation factor, and concluded that, although sub-Ångstrom-scale lateral resolution could be achievable, the vertical probe size would be too large for differentiating individual atoms in a nanostructure. By combining depth-sectioning and precise atom-counting methods, Alania et al. (2017) reconstructed 3D atomic-resolution images of Au nanorods. Although the depth resolution was not good enough to allow precise determination of each atom within a column of atoms, this approach provided depth location of an entire atomic column as a whole, enabling 3D determination of the morphology of the nanostructure of interest. Significant challenges, however, remain to be overcome before 3D atomic-resolution imaging by optical depth sectioning can be realized in STEM.

Atomic-Resolution Elemental Mapping

Atomic-Resolution Chemical Mapping by EELS

Ever since the invention of the field-emission STEM by Crewe, EELS has played a major role in identifying composition or valence state of the probed region of interest with a spatial resolution determined by the electron probe size and an impact parameter (Ritchie & Howie, 1988; Colliex et al., 1999; García de Abajo, 2010). For core-loss edges, their shapes in EELS spectra reflect the underlying local partial density of states modified by the presence of a core hole (Colliex & Jouffrey, 1972). Such core-loss peaks not only carry element specific information but also the valence state or bonding of the probed atom or columns of atoms. Batson, using an improved HB501 STEM and a high-resolution electron spectrometer (Batson, 1986, 1988, 1993), resolved the different bonding states of silicon atoms (Si^0, Si^{2+}, Si^{4+}) across an Si–SiO_2 interface and the oxidation state of individual columns of unit cells, containing pairs of silicon atoms, firmly establishing STEM-EELS as a powerful tool for atomic-scale analysis of materials chemistry. By using an electron probe size of ~0.22 nm and a thin specimen, Browning et al. (1993), with the assistance of ADF STEM imaging to identify the atomic positions of an epitaxial $CoSi_2$–Si interface, demonstrated that an EELS signal could be used to obtain information about chemical composition at atomic-scale resolution. Browning et al. (1993) proposed the possibility of interpreting the observed fine structure of the EELS spectra in terms of chemical bonding on the atomic scale. Almost at the same time, Muller et al. (1993) reported spatial mapping of carbon sp^2 and sp^3 states with a subnanometer spatial resolution, clearly demonstrating the feasibility of 2D mapping of bonding states at buried interfaces with an image resolution approaching atomic level.

The detection limit of the EELS technique was predicted to be a single atom (Isaacson & Johnson, 1975). With the use of a modified Gatan PEELS 666 on a non-aberration-corrected VG HB501, Suenaga et al. (2000) not only analyzed Gd atoms inside a single chain of metallofullerene molecules (Gd@C82), which were encapsulated within a single-wall carbon nanotube, but also formed elemental maps of individual single Gd atoms. The carbon nanotubes facilitated stabilization of the Gd-containing molecular complexes, significantly alleviating electron-beam-induced effects. Even though the isolated Gd atoms were detected and spatially resolved, the spatial resolution was only ~0.6 nm but sufficient to resolve the widely spaced Gd atoms. By using an ac-STEM to significantly increase the intensity within a sub-Ångstrom electron probe, Varela et al. (2004) were able to conduct spectroscopic imaging of single atoms embedded within a bulk solid. Dynamical simulations confirmed that the spectroscopic information was spatially confined to the La atom within the $CaTiO_3$. The authors demonstrated the potential of locating the depth of La-dopant atoms within the crystal. Atomic-resolution EELS analysis and mapping on a single-atom level are now routinely available on ac-STEM instruments, opening up new opportunities for studying a variety of materials systems with single-atom chemical sensitivity (Suenaga et al., 2009; Suenaga & Koshino, 2010; Ramasse et al., 2012; Zhou et al., 2012*a*, 2012*b*; Lin et al., 2015). Electron-beam-induced effects, however, pose major limitations on the chemical and structural integrity of the specimen of interest. For example, metal adatoms on catalyst supports may not maintain their chemical environment under the conditions for single-atom STEM-EELS analysis.

Atomic-resolution chemical mapping of columns of elements require small probe sizes since the distances among the neighboring columns of atoms are usually <0.3 nm. The availability of an ac-STEM, which allows a large probe-forming aperture to produce a sub-Ångstrom electron probe with a significantly increased beam current (Batson et al., 2002), made it possible to obtain atomic-resolution EELS line profiles of Ti L-shell EELS in a $SrTiO_3$ crystal (Allen et al., 2003). Even with a non-aberration-corrected VG HB501 dedicated STEM, Bosman et al. (2007) were able to demonstrate the plausibility of 2D atomic-resolution chemical mapping of $Bi_{0.5}Sr_{0.5}MnO_3$ by using a probe-forming semi-angle and EEL detector semi-angle of ~24 mrad and a mapping acquisition time of ~10 min. With the use of an ac-STEM and stable environment/microscope, Kimoto et al. (2007) demonstrated 2D atomic-column imaging of a crystal specimen using localized inelastically scattered electrons.

Downloaded from https://www.cambridge.org/core. IP address: 68.98.49.119, on 04 Sep 2021 at 06:14:57, subject to the Cambridge Core terms of use, available at https://www.cambridge.org/core/terms. https://doi.org/10.1017/S1431927621012125

The atomic columns of La, Mn, and O in the layered manganite $La_{1.2}Sr_{1.8}Mn_2O_7$ were clearly visualized. These authors further investigated the dependence of delocalization on the energy of inelastically excited primary electrons. Oxley et al. (2007) theoretically investigated the origin of the atomic-resolution EELS signal and discovered that delocalization of inelastically scattered electrons would not preclude atomic-resolution but would reduce image contrast. They further discussed the appearance and origins of volcano-like features at the EELS edge peaks.

A 2D EELS chemical map that contains bonding information requires much higher beam current to significantly improve the signal-to-noise ratio. By using a Nion STEM with fifth-order correction (Krivanek et al., 2008) to further focus more electrons into a finer electron probe and a modified spectrometer (Krivanek et al., 2008) to extend EELS collection angles up to ~60 mrad, Muller et al. (2008) were able to obtain impressive atomic-resolution chemical bonding maps of a $La_{0.7}Sr_{0.3}MnO_3/SrTiO_3$ multilayer sample. Changes in the titanium bonding due to variations in the local environment helped distinguish chemical interdiffusion from imaging artifacts. The success of this work, because of the improved optics to significantly increase both the probe convergence and EELS collection angles, unambiguously proves that 2D chemical imaging at the atomic scale with simultaneous elemental identification and visualization of local bonding states can be readily achieved. Muller (2009) summarized the achievements in atomic-resolution 2D elemental and bonding mapping and assessed that there could be over a 100-fold difference between corrected and conventional STEM instruments in terms of probe current or spectrum acquisition speed. Further improvement in detector and detection configuration as well as the electron source could facilitate a significant increase in the collected EELS signals. Electron-beam-induced effects, however, may set the limit for useful electron probe currents and low-voltage approach might alleviate some of the electron-beam-induced effects. Wang et al. (2011) conducted atomic-scale chemical analysis of grain boundaries in polycrystalline materials and revealed the interplay between atomic defects and impurities at the grain boundaries. Through such investigations, one can gain deep insights in understanding grain boundary transformations and how they modify material properties. Applications of atomic-resolution chemical mapping to various material systems have greatly enhanced our understanding of the atomic-world of materials (Browning et al., 2001; Kourkoutis et al., 2010; Trasobares et al., 2011; Ishikawa et al., 2014; Zamani et al., 2018). Figure 23 shows a large-area atomic-resolution EELS map of oxide superlattices. Such atomic-resolution elemental maps aid the fundamental understanding of quantum many-body interactions (Monkman et al., 2012).

Watanabe et al. (2010) discussed practical aspects of acquiring atomic-resolution 2D chemical maps by collecting either EELS or X-ray energy-dispersive spectrometry (XEDS) signals. In addition to discussing forming appropriate probe sizes/currents, these authors emphasized the development of sophisticated approaches to data acquisition and analysis and provided examples of atomic-resolution chemical mapping of different types of materials. Cueva et al. (2012) discussed the importance of improving background estimation and increasing chemical sensitivity in atomic-resolution chemical maps by utilizing new algorithms to analyze dose-limited spectral maps. They proposed an analysis procedure by considering a linear combination of power laws and local background averaging. They identified potential issues with the principal component analysis approach and discussed alternative approaches to processing chemical maps. Localization/delocalization of inelastic electron scattering events, EELS signal strength, and the effects of elastic/diffuse scattering on the collected EELS signal were extensively investigated to understand the nature of atomic-resolution elemental maps (Dwyer, 2013; Lugg et al., 2014; Allen, 2017).

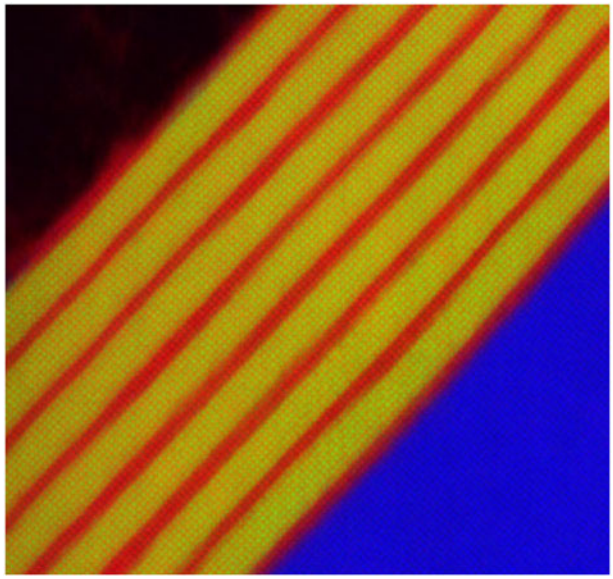

Fig. 23. EELS map over a wide field of view from an $n = 3$ $(LaMnO_3)2n/(SrMnO_3)n/SrTiO_3$ film measured, showing La in green, Mn in red, and Ti in blue. The irregularity of the topmost surface in this image is an artifact of the preparation procedure for EELS and HAADF-STEM measurements and does not reflect the topmost surface of the as-grown film. Adapted from Monkman et al. (2012).

Atomic-Resolution Chemical Mapping by XEDS

Atomic-resolution elemental mapping via XEDS was accomplished in 2010 (Chu et al., 2010; D'Alfonso et al., 2010; Watanabe et al., 2010) and was applied to qualitative study of various material systems (Klenov & Zide, 2011; Allen et al., 2012; Kotula et al., 2012; Itakura et al., 2013; Lu et al., 2013). A qualitative interpretation of atomic-resolution XEDS maps seems intuitive but quantitative analysis requires consideration of the effects of strong dynamical scattering (channeling) of the electron probe on the generation of XEDS signals. When a crystal is aligned with a zone-axis parallel to the incident beam direction (i.e., the condition for atomic-resolution imaging), the electron beam becomes localized around the columns of nuclei, generating X-ray signals. In this case, however, the relationship between the concentration of a particular element and the detected X-ray signal strength is generally nonlinear, significantly complicating the quantification of atomic-resolution XEDS maps. Forbes et al. (2012) investigated the contribution of thermally scattered electrons to the collected XEDS signal. Although the experimental results could not be directly interpretable, they demonstrated that first-principle simulations would be useful for understanding the intensity of atomic-resolution XEDS maps. Kothleitner et al. (2014) showed good quantitative agreement between experimental XEDS maps and electron-channeling-based simulations when they evaluated the relative signal strengths of different atomic columns. However, due to electron-channeling effects, the measured compositions might not represent the true stoichiometry of the probed region. The consequences of electron channeling include

Downloaded from https://www.cambridge.org/core. IP address: 68.98.49.119, on 04 Sep 2021 at 06:14:57, subject to the Cambridge Core terms of use, available at https://www.cambridge.org/core/terms. https://doi.org/10.1017/S1431927621012125

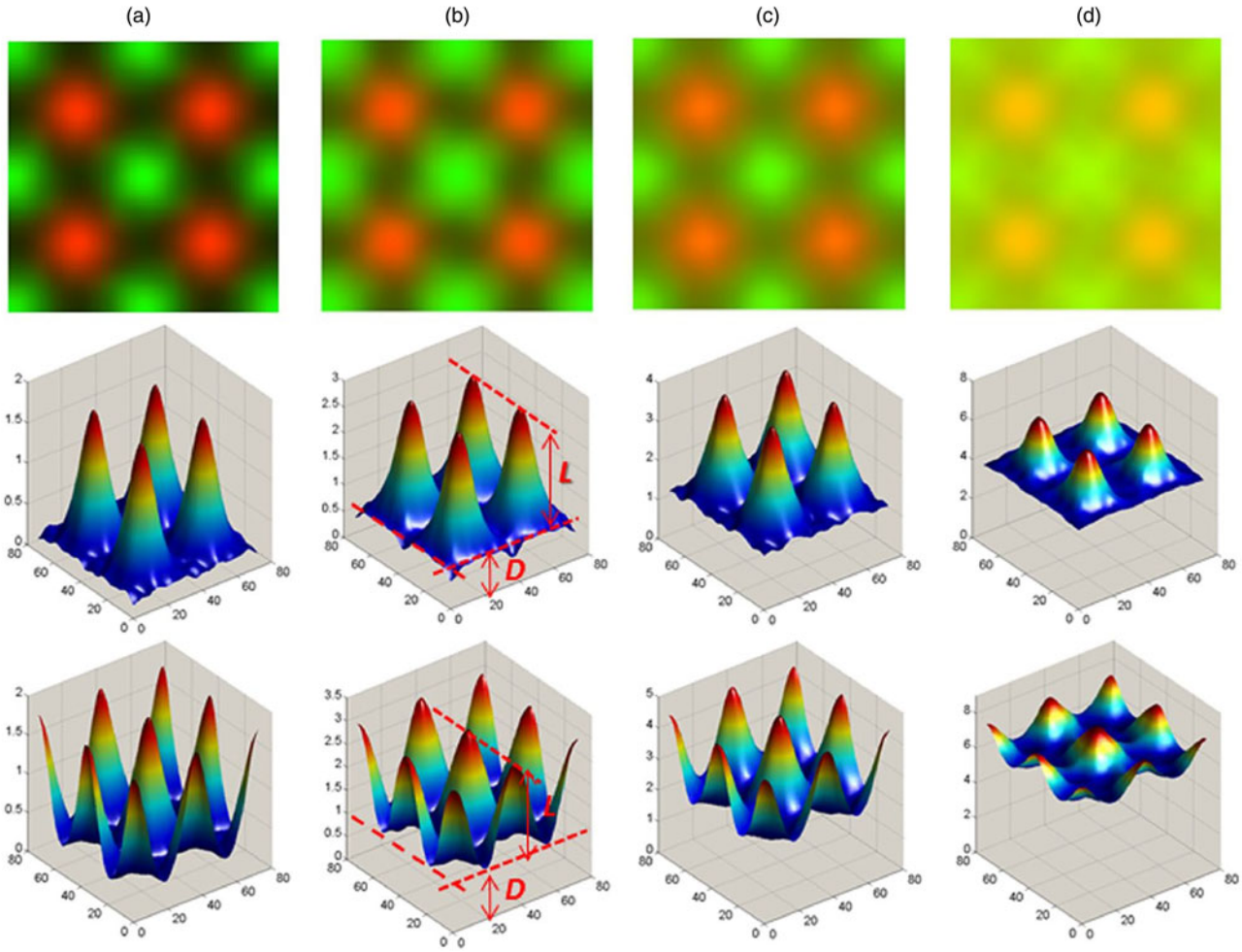

Fig. 24. Averaged 2 × 2 unit-cell XEDS maps (the top panel) (Ti K in red, Sr K + L in green) obtained by using the single-frame scanning method, along with the 3D plots for the Ti K map (the middle panel) and Sr K + L (the bottom panel) at several crystal thickness: (**a**) 16 nm, (**b**) 23 nm, (**c**) 42 nm, and (**d**) 106 nm. In the middle and bottom panel of (**b**), the localized (L) and delocalized (D) X-ray level are illustrated. The *x*- and *y*-axes in 3D plots are in a pixel number (a pixel size of 0.011 nm). Reproduced from Lu et al. (2018).

(1) changes in relative image contrast and (2) changes in absolute-scale intensity. Chen et al. (2015), using an atomic-scale electron probe and first-principle simulations, demonstrated good agreement between experiment and simulation in the total number of X-ray counts recorded for atomic-resolution maps of an $SrTiO_3$ specimen.

The use of multiple, large-area, silicon-drift detectors (SDDs) in an ac-STEM (Lu et al., 2013) enables a sufficient signal-to-noise ratio to produce high-quality atomic-resolution XEDS maps. The increased complexity of such detector geometries requires accurate numerical modeling to determine the effective detector solid-angle and X-ray absorption within the specimen and from the sample holder. Since electron-channeling effects could become significant in quantitative analysis of atomic-resolution XEDS maps, Dycus et al. (2016) investigated the influence of key experimental parameters on such XEDS maps. They studied the role of the probe-forming convergence semi-angle, sample thickness, lattice spacing, and dwell/collection time in determining the strength of the acquired XEDS signals. These authors found that an optimum specimen-dependent probe-forming convergence angle exists for maximizing the signal-to-noise ratio of atomically resolved XEDS maps. These practical considerations provided deeper insights into the selection of experimental parameters to acquire better, and to correctly interpret, atomic-resolution XEDS maps.

Even with multiple SDDs and aberration-corrected electron probes, the XEDS signal is still relatively weak when the specimen is very thin (e.g., 2D materials). For thicker specimens, both beam broadening and dynamic scattering effects can severely degrade image resolution and complicate quantitative interpretation of atomic-resolution XEDS maps. For each sample, there seems to exist a range of specimen thicknesses that give both a reasonable signal-to-noise ratio and a tolerable simple analysis of atoms column-by-column. A quantitative interpretation of atomic-resolution XEDS maps, however, require detailed simulations (Lugg et al., 2015*b*; Chen et al., 2016; MacArthur et al., 2017). Lu et al. (2018) used a single-frame scanning technique rather than an averaging multiple-frame approach to avoid peak broadening (Fig. 24). They showed that the localization of emitted X-rays to the atomic columns strongly depended on crystal thickness. They suggested the use of a thin crystal to improve spatial resolution in atomic-scale XEDS mapping. The quantitative analysis of atomic-resolution XEDS maps of interfaces is challenging and more complex because electrons may channel differently in different crystalline specimens (Spurgeon et al., 2017; Feng et al., 2018).

Downloaded from https://www.cambridge.org/core. IP address: 68.98.49.119, on 04 Sep 2021 at 06:14:57, subject to the Cambridge Core terms of use, available at https://www.cambridge.org/core/terms. https://doi.org/10.1017/S1431927621012125

By slightly tilting the specimen off-zone axis, the quantification of XEDS maps may become manageable but atomic resolution may not be achievable, especially for thicker samples.

Future Prospects

The practical realization of aberration corrector on the STEM has transformed the field of electron microscopy. Aberration-corrected STEM has found broad applications in characterizing materials, significantly enhancing our understanding of the micro- and nano-world of matter. With such an enabling tool, we can examine the complexities of structure and chemistry at the atomic scale that have never been achieved before. By conducting *in situ* or *operando* experiments within an ac-STEM instrument, we can now follow and understand the reaction or/and transformation pathways that reflect intrinsic material properties. Such atomic-scale understanding of materials behavior leads to crucial insights into developing new materials with desired properties, fabricating new devices with improved performance, or understanding the fundamental physics principles that govern the nano- or atomic-world. The combination of ac-STEM results (e.g., 3D atom coordinates, species, bonding distances, dynamic behavior, etc.) with first-principle calculations has already been, and will continue to be, a driving force for not only a fundamental understanding of material properties but also for enabling new discoveries in material systems and devices. It is anticipated that aberration-corrected electron microscopy, in combination with the related spectroscopy, diffraction, and *in situ* techniques, will play an indispensable role in the field of materials and engineering including quantum materials and information, energy materials and systems, catalysis and chemical transformation, sensing and detection, and so on.

Although the electron microscopy community has made significant strides in the past 50 years to achieve sub-Ångstrom image resolution (even at low voltages), we still have not developed a practical approach to routinely obtaining 3D atom maps of practical samples with picometer precision in determining atom coordinates (especially at defect sites) and single-atom chemical sensitivity. As discussed in the section "Atomic-resolution electron tomography," atomic-resolution electron tomography provides a route to resolving 3D atomic structure of materials, leading to investigations of grain boundaries, dislocations, stacking faults, point defects, chemical order/disorder, bond distortion, strain tensors, etc. Atomic-resolution electron tomography, conducted via 4D electron microscopy, significantly expands the application of this method to studying a plethora of materials problems including early-stage nucleation of crystals (Zhou et al., 2019). Yang et al. (2021) extended this powerful approach to determining the 3D atomic positions of an amorphous solid. The authors studied the short-range and medium-range order (SRO and MRO) in a multi-component glass-forming alloy. The combination of advanced computational imaging techniques (e.g., correction for image distortions, enhancement of signal-to-noise ratio, robust reconstruction algorithms, and so on) with a state-of-the-art microscope and accessories is critical to their success in solving a challenging materials problem. This work clearly demonstrates the power of 3D atomic-resolution imaging in addressing grand challenges that may fundamentally confirm or change our view of matter at the level of the most fundamental building block—3D coordinates of atoms.

In addition to further advances in hardware development, robust image calculations and processing algorithms, ultrafast and efficient electron detectors, and ultrafast computers are definitely needed. For example, would it be feasible to display 4D-STEM images on-the-fly when practical samples are examined? Would it be possible to conduct 3D atomic-resolution electron tomography on a large number of heterogeneous structures so that statistically meaningful data can be obtained? As discussed in this review, ultrafast computers and robust image processing algorithms played a critical role in successfully implementing aberration correctors on TEMs/STEMs. One would imagine an ideal scenario that outputs of DFT calculations based on inputs from ac-STEM results can be evaluated on-the-fly. To achieve such a high level of sophistication may require implementation of machine learning (ML) and artificial intelligence (AI)-assisted operation of electron microscopes equipped with ultrafast computers.

Electron microscopists have often faced the challenge of correlating microscopic observations with macro-scale property measurements. Since ultrahigh-resolution imaging experiments usually do not provide excellent statistical data, which is usually required for understanding structure–property relationships, it becomes crucial for developing robust approaches that provide statistically meaningful data. It is enticing to speculate that such a job may be implementable when ML and AI are integrated into routine operations of electron microscopes. The development of AI-assisted synthesis (Coley et al., 2019; Steiner et al., 2019; Burger et al., 2020) provided a good example. When electron microscopes can routinely provide statistically meaningful data, the ac-STEM will have a tremendous impact on nanoscience and nanotechnology, nanoscale systems and devices, heterogeneous catalysis, and so on. The breadth of data produced by current ac-STEM experiments, for example, 4D-STEM imaging of dynamic events plus statistical analysis, is already enormous and poses challenges to many aspects of advances in microscopy and materials research. It becomes critical and urgent to identify appropriate approaches to imaging informatics and data science in order to extract valuable structural and chemical information that is buried in massive datasets. Such complex, multilayer and iterative tasks (e.g., rapid segmentation, classification, augmented analysis, diagnosis and error correction, etc.) could not be accomplished without the assistance of ultrafast computers and robust algorithms. Fortunately, electron microscopists have realized this problem and have already started developing innovative approaches to solving such a data science problem (Kalinin et al., 2015; Voyles, 2017; Ziatdinov et al., 2017; Xu & LeBeau, 2018; Aguiar et al., 2019; Kalinin et al., 2019; Laanait et al., 2019; Spurgeon et al., 2021).

The interaction of an energetic electron beam with matter not only generates various types of signals that carry information about the specimen but also transfers energy/momentum to the specimen which may induce changes in local structure, break chemical bonds, or even cause diffusion/evaporation of atomic species in the probed region of interest (Egerton et al., 2004; Egerton, 2014, 2019). If the electron-beam-induced degradation effects are not properly accounted for, then erroneous conclusions may be drawn about the structure–property relationships. Electron-beam degradation effects are difficult to predict and should be quantitatively evaluated for each specific type of sample. Electron-beam-induced effects are known to include: (1) knock-on damage, (2) radiolysis, (3) electrostatic charging, and (4) thermal damage caused by electron-beam heating (Egerton et al., 2004; Egerton, 2019). The mitigation methods, however, are not well-developed especially for radiolysis effects. One usually

Downloaded from https://www.cambridge.org/core. IP address: 68.98.49.119, on 04 Sep 2021 at 06:14:57, subject to the Cambridge Core terms of use, available at https://www.cambridge.org/core/terms. https://doi.org/10.1017/S1431927621012125

uses low voltages to minimize the knock-on damage, but simultaneously the radiolysis effects may increase. Even for knock-on damage, we do not have a full understanding on how it occurs at surfaces/interfaces, dopants, adatoms, and various types of defects. For example, radiolytic damage in oxides may arise from excitation of oxygen, leading to bond breakage, desorption of oxygen atoms at the specimen surface, and finally reducing the valence state of the corresponding metallic cations (Jiang, 2016). Such electron-beam-induced radiolysis processes produce dynamic and stable defects, break/form chemical bonds, and displace atoms, resulting in atomic-resolution images that do not represent the original intact specimen at all. Such electron-beam-induced effects become more critical under gas or liquid environment. Therefore, it is critical for the electron microscopy community to quantitatively understand electron-beam-induced effects and to develop effective mitigation approaches. Low-dose electron microscopy approaches have been successfully and extensively used for examining biological systems. Chen et al. (2020) reported that compared with the conventional STEM imaging method, the use of the mixed-state electron ptychography approach not only achieved atomic-resolution with picometer precision but also reduced electron dose by ~50 times. Another approach to low-dose STEM imaging is sparse sampling (Kovarik et al., 2016; Stevens et al., 2018; Nicholls et al., 2020). Such a process tempo-spatially separates overlapping of electron-specimen interaction volume, and consequently, an "optimum distance" could be defined to form a scanning image. By using an inpainting method, atomic-resolution images can be reconstructed with an effective low-dose irradiation. High-resolution imaging with extremely low-dose conditions ($\leq$1 $e^{-}/Å^{2}$) was proposed and reported (Stevens et al., 2018).

Electron microscopy at cryo temperatures, with a goal to mitigate electron-beam-induced structural damage, was successfully utilized for studying biological molecules (Taylor & Glaeser, 1974; Fernandez-Leiro & Scheres, 2016; Frank, 2016; Vinothkumar & Henderson, 2016). The incorporation of direct electron detectors with unprecedented speed and sensitivity (McMullan et al., 2014) into modern electron microscopes started a "Resolution Revolution" in molecular biology (Kühlbrandt, 2014). By combining a highly coherent electron source (low-energy-spread) with energy filtering of inelastically scattered electrons and a high-quality direct electron detector, together with the use of robust reconstruction algorithms, Yip et al. (2020) and Nakane et al. (2020) obtained atomic-resolution structures of proteins, enabling the location of individual atoms in a protein to be determined for the first time. These developments are expected to help researchers gain a better understanding, at atomic resolution, of how proteins work in health and disease, leading to the design of better therapeutics. Such a strategy could be used to image inorganic materials or soft materials provided that the specimen holder and the sample are stable enough. The success in atomic-resolution imaging of sensitive battery materials and interfaces by cryo-electron microscopy was clearly a good example (Li et al., 2017; Wang et al., 2019*a*, 2019*b*). Savitzky et al. (2018) demonstrated that after registering all possible image pairs in a multi-image stack to enhance the signal-to-noise ratio and to correct stage shifts high-quality average images, with information transfer out to 0.07 nm, could be achieved at 300 kV at near liquid nitrogen temperature. The low-temperature mitigation approach provided atomic-resolution STEM images of electron-beam-sensitive metal-oxide nanoparticles with applications in fabricating Li-ion batteries (Tyukalova & Duchamp, 2020). High-resolution cryo-STEM imaging was used to detect isolated protein-bound metal ions (Elad et al., 2017) and to study the fundamental building blocks of enamel (DeRocher et al., 2020). Goodge et al. (2020), taking advantage of direct electron detection to enable low-signal experiments, reported atomic-resolution elemental mapping at cryogenic temperatures. It is anticipated that the construction of stable cryo-STEM instruments, in combination with low-dose 4D-STEM imaging, will significantly broaden applications of STEM imaging and associated techniques to research frontiers in physics, chemistry, biology, and materials science and engineering.

Going to extremely low temperatures (e.g., liquid helium temperature) will enable numerous research opportunities for quantum science and technology (Minor et al., 2019). Since quantum phenomena involve small energies any thermal and/or electron-beam-induced effects at room temperature would wash out the expected quantum behavior. STEM-associated spectroscopy methods at 1–2 meV (or sub-meV) energy resolution would be required for studying quantum phenomena related to small energy excitations. Directly imaging and spectroscopically analyzing quantum materials with atomic-resolution at extremely low temperatures are expected to be highly challenging but the reward could be tremendous. Going to cryo temperatures, however, does not solve other problems such as observing chemical reactions under reaction conditions. Although the ultrafast electron microscopy method (Zewail, 2010; Campbell et al., 2019) has not achieved atomic-resolution yet, future successful advances in developing atomic-resolution ultrafast electron microscopy would allow us to examine chemical reactions on solid surfaces with significantly suppressed electron-beam-induced effects, to study crystal nucleation and growth processes in liquid environments, to measure atomic diffusion processes at desired sample temperatures, or to explore the atomic configurations of biological molecules and how they control the functions of biological systems. The arrival of atomic-resolution femtosecond or attosecond electron microscopy (if it is achievable) will unlock the mysteries of the dynamic world of matter. Although electron microscopists have made tremendous advances since Ruska's first electron microscope, there are more exciting opportunities in the future to significantly expand the societal impact of atomic-resolution electron microscopy.

Acknowledgments. This work was supported by the National Science Foundation under Grant No. 1955474 (CHE-1955474). The author acknowledges use of the John M. Cowley Center for High-resolution Electron Microscopy at Arizona State University throughout his research career. The author is grateful to Professor David J. Smith of Arizona State University for careful editing of the manuscript and for providing relevant references.

References

Abbe E (1873). Beiträge zur Theorie des Mikroskops und der mikroskopischen Wahrnehmung. *Archiv f Mikrosk Anatomie* **9**, 413–468.

Aguiar J, Gong M, Unocic R, Tasdizen T & Miller B (2019). Decoding crystallography from high-resolution electron imaging and diffraction datasets with deep learning. *Sci Adv* **5**, eaaw1949.

Alania M, Altantzis T, De Backer A, Lobato I, Bals S & Van Aert S (2017). Depth sectioning combined with atom-counting in HAADF STEM to retrieve the 3D atomic structure. *Ultramicroscopy* **177**, 36–42.

Allen LJ (2017). Simulation in elemental mapping using aberration-corrected electron microscopy. *Ultramicroscopy* **180**, 142–149.

Allen LJ, D'Alfonso AJ, Freitag B & Klenov D (2012). Chemical mapping at atomic resolution using energy-dispersive X-ray spectroscopy. *MRS Bull* **37**, 47–52.

Allen LJ, Findlay SD, Lupini AR, Oxley MP & Pennycook SJ (2003). Atomic-resolution electron energy loss spectroscopy imaging in aberration

Downloaded from https://www.cambridge.org/core. IP address: 68.98.49.119, on 04 Sep 2021 at 06:14:57, subject to the Cambridge Core terms of use, available at https://www.cambridge.org/core/terms. https://doi.org/10.1017/S1431927621012125

corrected scanning transmission electron microscopy. *Phys Rev Lett* **91**, 105503.

Allen LJ, Findlay SD, Oxley MP, Witte C & Zaluzec NJ (2006). Channeling effects in high-angular-resolution electron spectroscopy. *Phys Rev B* **73**, 094104.

Allpress J, Sanders J & Wadsley A (1969). Multiple phase formation in the binary system Nb_2O_5–WO_3. VI. Electron microscopic observation and evaluation of non-periodic shear structures. *Acta Crystallogr B* **25**, 1156–1164.

Allpress JG & Sanders JV (1973). The direct observation of the structure of real crystals by lattice imaging. *J Appl Crystallogr* **6**, 165–190.

Almeida TP, McGrouther D, Temple R, Massey J, Li Y, Moore T, Marrows CH & McVitie S (2020). Direct visualization of the magnetostructural phase transition in nanoscale FeRh thin films using differential phase contrast imaging. *Phys Rev Mater* **4**, 034410.

Altantzis T, Lobato I, De Backer A, Béché A, Zhang Y, Basak S, Porcu M, Xu Q, Sánchez-Iglesias A, Liz-Marzán LM, Van Tendeloo G, Van Aert S & Bals S (2019). Three-dimensional quantification of the facet evolution of Pt nanoparticles in a variable gaseous environment. *Nano Lett* **19**, 447–481.

Amali A & Rez P (1997). Theory of lattice resolution in high-angle annular dark-field images. *Microsc Microanal* **3**, 28–46.

Amali A, Rez P & Cowley JM (1997). High angle annular dark field imaging of stacking faults. *Micron* **28**, 89–94.

Andersen AH & Kak AC (1984). Simultaneous algebraic reconstruction technique (SART): A superior implementation of the art algorithm. *Ultrason Imaging* **6**, 81–94.

Ansari R, Beuville E, Borer K, Cenci P, Clark AG, Federspiel A, Gildemeister O, Gössling C, Hara K, Heijne EHM, Jarron P, Lariccia P, Lisowski B, Munday DJ, Pal T, Parker MA, Redaelli N, Scampoli P, Simak V, Singh SL, Vallon-Hulth T & Wells PS (1989). The silicon detectors in the UA2 experiment. *Nucl Instrum Methods Phys Res A* **279**, 388–395.

Anstis GR, Cai DQ & Cockayne DCH (2003). Limitations on the s-state approach to the interpretation of sub-angstrom resolution electron microscope images and microanalysis. *Ultramicroscopy* **94**, 309–327.

Aronova MA & Leapman RD (2012). Development of electron energy-loss spectroscopy in the biological sciences. *MRS Bull* **37**, 53–62.

Aso R, Kan D, Shimakawa Y & Kurata H (2013). Atomic level observation of octahedral distortions at the perovskite oxide heterointerface. *Sci Rep* **3**, 2214.

Aso R, Kan D, Shimakawa Y & Kurata H (2014). Control of structural distortions in transition-metal oxide films through oxygen displacement at the heterointerface. *Adv Funct Mater* **24**, 5177–5184.

Bailey DH & Swarztrauber PN (1991). The fractional Fourier transform and applications. *SIAM Rev* **33**, 389–404.

Bain A (1843). Electric time-pieces and telegraphs. British Patent No 9745, filed 27 May 1843.

Bammes B, Ramachandra R, Mackey MR, Bilhorn R & Ellisman M (2019). Multi-color electron microscopy of cellular ultrastructure using 4D STEM. *Microsc Microanal* **25**, 1060–1061.

Bárcena-González G, Guerrero-Lebrero MP, Guerrero E, Yañez A, Nuñez-Moraleda B, Fernández-Reyes D, Real P, González D & Galindo PL (2020). CDrift: An algorithm to correct linear drift from a single high-resolution STEM image. *Microsc Microanal* **26**, 913–920.

Batson PE (1986). High-energy resolution electron spectrometer for 1-nm spatial analysis. *Rev Sci Instrum* **57**, 43–48.

Batson PE (1988). Parallel detection for high-resolution electron energy loss studies in the scanning transmission electron microscope. *Rev Sci Instrum* **59**, 1132–1138.

Batson PE (1993). Simultaneous STEM imaging and electron energy-loss spectroscopy with atomic-column sensitivity. *Nature* **366**, 727–728.

Batson PE, Dellby N & Krivanek OL (2002). Sub-ångstrom resolution using aberration corrected optics. *Nature* **418**, 617–620.

Beck V & Crewe AV (1974). A quadrupole octupole corrector for a 100 kV STEM. *Proc Annu Meet EMSA* **32**, 426–427.

Beck V & Crewe AV (1975). High-resolution imaging properties of STEM. *Ultramicroscopy* **1**, 137–144.

Beck VD (1979). Aberration correction in the STEM. *Optik* **53**, 241–255.

Berkels B, Binev P, Blom DA, Dahmen W, Sharpley RC & Vogt T (2014). Optimized imaging using non-rigid registration. *Ultramicroscopy* **138**, 46–56.

Berkels B & Liebscher CH (2019). Joint non-rigid image registration and reconstruction for quantitative atomic resolution scanning transmission electron microscopy. *Ultramicroscopy* **198**, 49–57.

Betzig E (1995). Proposed method for molecular optical imaging. *Opt Lett* **20**, 237–239.

Betzig E & Chichester RJ (1993). Single molecules observed by near-field scanning optical microscopy. *Science* **262**, 1422–1425.

Betzig E, Patterson GH, Sougrat R, Lindwasser OW, Olenych S, Bonifacino JS, Davidson MW, Lippincott-Schwartz J & Hess HF (2006). Imaging intracellular fluorescent proteins at nanometer resolution. *Science* **313**, 1642–1645.

Betzig E & Trautman JK (1992). Near-field optics: Microscopy, spectroscopy, and surface modification beyond the diffraction limit. *Science* **257**, 189–195.

Black G & Linfoot EH (1957). Spherical aberration and the information content of optical images. *Proc R Soc Lond A* **239**, 522–540.

Borisevich AY, Lupini AR & Pennycook SJ (2006). Depth sectioning with the aberration-corrected scanning transmission electron microscope. *Proc Natl Acad Sci USA* **103**, 3044–3048.

Bosman M, Keast VJ, García-Muñoz JL, D'Alfonso AJ, Findlay SD & Allen LJ (2007). Two-dimensional mapping of chemical information at atomic resolution. *Phys Rev Lett* **99**, 086102.

Bradley SA, Cohn MJ & Pennycook SJ (1994). Z-contrast imaging of supported Pt and Pd clusters. *Microsc Res Tech* **28**, 427–429.

Bradley SA, Sinkler W, Blom DA, Bigelow W, Voyles PM & Allard LF (2012). Behavior of Pt atoms on oxide supports during reduction treatments at elevated temperatures, characterized by aberration corrected STEM imaging. *Catal Lett* **142**, 176–182.

Braidy N, Le Bouar Y, Lazar S & Ricolleau C (2012). Correcting scanning instabilities from images of periodic structures. *Ultramicroscopy* **118**, 67–76.

Brown HG, Ishikawa R, Sanchez-Santolino G, Lugg NR, Ikuhara Y, Allen LJ & Shibata N (2017). A new method to detect and correct sample tilt in scanning transmission electron microscopy bright-field imaging. *Ultramicroscopy* **173**, 76–83.

Brown HG, Ishikawa R, Sánchez-Santolino G, Shibata N, Ikuhara Y, Allen LJ & Findlay SD (2019). Large angle illumination enabling accurate structure reconstruction from thick samples in scanning transmission electron microscopy. *Ultramicroscopy* **197**, 112–121.

Browning ND, Arslan I, Ito Y, James EM, Klie RF, Moeck P, Topuria T & Xin Y (2001). Application of atomic scale STEM techniques to the study of interfaces and defects in materials. *J Electron Microsc* **50**, 205–218.

Browning ND, Chisholm MF & Pennycook SJ (1993). Atomic-resolution chemical analysis using a scanning transmission electron microscope. *Nature* **336**, 143–146.

Buerger J, Riedl T & Lindner JKN (2020). Influence of lens aberrations, specimen thickness and tilt on differential phase contrast STEM images. *Ultramicroscopy* **219**, 113118.

Burge RE & Dainty JC (1976). Partially coherent image-formation in the scanning-transmission electron-microscope (STEM). *Optik* **46**, 229–240.

Burger B, Maffettone PM, Gusev VV, Aitchison CM, Bai Y, Wang X, Li X, Alston BM, Li B, Clowes B, Rankin N, Harris B, Sprick RS & Cooper AI (2020). A mobile robotic chemist. *Nature* **583**, 237–241. doi:10.1038/s41586-020-2442-2

Busch H (1926). Berechnung der Bahn von Kathodenstrahlen im axialsymmetrischen elektromagnetischen Felde. *Ann Phys* **81**, 974–993. doi:10.1002/andp.19263862507

Butler JH & Cowley JM (1983–1984). Phase contrast imaging using a scanning transmission electron microscope. *Ultramicroscopy* **12**, 39–50.

Butler JW (1966). Digital computer techniques in electron microscopy. *Proceedings of the 6th International Congress on Electron Microscopy*, Kyoto, vol. **1**, pp. 191–192, Maruzen, Tokyo.

Campbell GH, McKeown JT & Santala MK (2019). High-speed electron microscopy. In *Springer Handbook of Microscopy*, Hawkes PW & Spence JCH (Eds.). Cham: Springer Handbooks. Springer.

Caswell TA, Ercius P, Tate MW, Ercan A, Gruner SM & Muller DA (2009). A high-speed area detector for novel imaging techniques in a scanning transmission electron microscope. *Ultramicroscopy* **109**, 304–311.

Chang DJ, Kim DS, Rana A, Tian X, Zhou J, Ercius P & Miao J (2020). Ptychographic atomic electron tomography: Towards three-dimensional imaging of individual light atoms in materials. *Phys Rev B* **102**, 174101.

Downloaded from https://www.cambridge.org/core. IP address: 68.98.49.119, on 04 Sep 2021 at 06:14:57, subject to the Cambridge Core terms of use, available at https://www.cambridge.org/core/terms. https://doi.org/10.1017/S1431927621012125

Chapman JN, Batson PE, Waddell EM & Ferrier RP (1978). The direct determination of magnetic domain wall profiles by differential phase contrast electron microscopy. *Ultramicroscopy* **3**, 203–214.

Chen CC, Zhu C, White ER, Chiu CY, Scott MC, Regan BC, Marks LD, Huang Y & Miao J (2013). Three-dimensional imaging of dislocations in a nanoparticle at atomic resolution. *Nature* **496**, 74–77.

Chen Z, D'Alfonso AJ, Weyland M, Taplin DJ, Findlay SD & Allen LJ (2015). Absolute scale energy dispersive X-ray analysis in scanning transmission electron microscopy. *Ultramicroscopy* **157**, 21–26.

Chen Z, Odstrcil M, Jiang Y, Han Y, Chiu M-H, Li L-J & Muller DA (2020). Mixed-state electron ptychography enables sub-angstrom resolution imaging with picometer precision at low dose. *Nat Commun* **11**, 2994.

Chen Z, Weyland M, Sang X, Xu W, Dycus JH, LeBeau JM, D'Alfonso AJ, Allen LJ & Findlay SD (2016). Quantitative atomic resolution elemental mapping via absolute-scale energy dispersive X-ray spectroscopy. *Ultramicroscopy* **168**, 7–16.

Chisholm MF & Pennycook SJ (1991). Structural origin of reduced critical currents at $YBa_2Cu_3O_{7-\Delta}$ grain-boundaries. *Nature* **351**, 47–49.

Chu M-W, Liou SC, Chang C-P, Choa S-F & Chen CH (2010). Emergent chemical mapping at atomic-column resolution by energy-dispersive X-ray spectroscopy in an aberration-corrected electron microscope. *Phys Rev Lett* **104**, 196101.

Coates DG (1967). Kikuchi-like reflection patterns observed in the SEM. *Philos Mag* **16**, 1179–1184.

Cockayne DJH, Goodman P, Mills JC & Moodie AF (1967). Design and operation of an electron diffraction camera for the study of small crystalline regions. *Rev Sci Instrum* **38**, 1097–1102.

Coley CW, Thomas III DA, Lummiss JAM, Jaworski JN, Breen CP, Schultz V, Hart T, Fishman JS, Rogers L, Gao H, Hicklin RW, Plehiers PP, Byington J, Piotti JS, Green WH, Hart AJ, Jamison TF & Jensen KF (2019). A robotic platform for flow synthesis of organic compounds informed by AI planning. *Science* **365**, eaax1566 (p1–p9).

Colliex C, Imhoff D, Perez-Omil JA, Stéphan O, Suenaga K & Tence M (1999). Electron energy-loss spectroscopy (EELS) on nano-dimensional structures. *J Electron Microsc* **48**, 995–1003.

Colliex C, Cosslett VE, Leapman RD & Trebbia P (1976). Contribution of electron energy loss spectroscopy to the development of analytical electron microscopy. *Ultramicroscopy* **1**, 301–315.

Colliex C & Jouffrey B (1972). Inelastic-scattering of electrons in a solid by excitation of deep atomic levels. 1. Energy-loss spectra. *Philos Mag* **25**, 491–511.

Colliex C & Mory C (1994). Scanning transmission electron microscopy of biological structures. *Biol Cell* **80**, 175–180.

Conchello JA & Lichtman J (2005). Optical sectioning microscopy. *Nat Methods* **2**, 920–931.

Cosgriff EC & Nellist PD (2006). A Bloch wave analysis of optical sectioning in aberration-corrected STEM. *Ultramicroscopy* **107**, 626–634.

Cosslett VE (1965). Possibilities and limitations for the differentiation of elements in the electron microscope. *Lab Invest* **14**, 1009–1019.

Cowley JM (1969). Image contrast in a transmission scanning electron microscope. *Appl Phys Lett* **15**, 58–59.

Cowley JM (1970). High-voltage transmission scanning electron microscopy. *J Appl Crystallogr* **3**, 49–59.

Cowley JM (1973*a*). High-resolution dark-field electron microscopy. I. Useful approximations. *Acta Crystallogr A* **29**, 529–536.

Cowley JM (1973*b*). High resolution dark-field electron microscopy. II. Short-range order in crystals. *Acta Crystallogr A* **29**, 537–540.

Cowley JM (1975). Coherent and incoherent imaging in the scanning transmission electron microscope. *J Phys D: Appl Phys* **8**, L77–L79.

Cowley JM (1976). Scanning transmission electron microscopy of thin specimens. *Ultramicroscopy* **2**, 3–16.

Cowley JM (1979*a*). Coherent interference in convergent beam electron diffraction and shadow imaging. *Ultramicroscopy* **4**, 435–450.

Cowley JM (1979*b*). Adjustment of STEM instrument by use of shadow images. *Ultramicroscopy* **4**, 413–418.

Cowley JM (1979*c*). High resolution studies of crystals using STEM. *Chem Scr* **14**, 33–38.

Cowley JM (1979*d*). Interference effects in a STEM instrument. *Micron* **11**, 229–233.

Cowley JM (1980). Interference effects in a STEM instrument. *Micron* **11**, 229–233.

Cowley JM (1981*a*). Coherent interference effects in STEM and CBED. *Ultramicroscopy* **7**, 19–26.

Cowley JM (1981*b*). Electron microdiffraction studies of the potential field at crystal surfaces. *Ultramicroscopy* **7**, 181–188.

Cowley JM (1982). Microdiffraction, STEM imaging and ELS at crystal surfaces. *Ultramicroscopy* **9**, 231–236.

Cowley JM (1983). The STEM approach to the imaging of surfaces and small particles. *J Microsc* **129**, 253–261.

Cowley JM (1984*a*). Microdiffraction and STEM of interfaces. *Ultramicroscopy* **14**, 27–36.

Cowley JM (1984*b*). Scanning transmission electron microscopy and microdiffraction techniques. *Bull Mater Sci* **6**, 477–490.

Cowley JM (1984*c*). The use of scanning transmission electron microscopes to study surfaces and small particles. *ACS Symp Ser* **248**, 353–366.

Cowley JM (1986). Electron diffraction phenomena observed with a high resolution STEM instrument. *J Electron Microsc Tech* **3**, 25–44.

Cowley JM (1990). High resolution side-band holography with a STEM instrument. *Ultramicroscopy* **34**, 293–297.

Cowley JM (1992). Twenty forms of electron holography. *Ultramicroscopy* **41**, 335–348.

Cowley JM (1993). Configured detectors for STEM imaging of thin specimens. *Ultramicroscopy* **49**, 4–13.

Cowley JM (1999). Electron nanodiffraction. *Microsc Res Tech* **46**, 75–97.

Cowley JM (2000). Electron holography with atomic focusers. *Phys Rev Lett* **84**, 3618–3621.

Cowley JM (2001). STEM imaging with a thin annular detector. *J Electron Microsc* **50**, 147–155.

Cowley JM (2004). Applications of electron nanodiffraction. *Micron* **35**, 345–360.

Cowley JM & Au AY (1978). Image signals and detector configurations in STEM. In *Scanning Electron Microscopy, 1978*, vol. **I**, Johari O (Ed.), pp. 53–60. Chicago (Illinois): Scanning Electron Microscopy, Inc.

Cowley JM, Hansen MS & Wang S-Y (1995). Imaging modes with an annular detector in STEM. *Ultramicroscopy* **58**, 18–24.

Cowley JM & Huang Y (1992). De-channelling contrast in annular dark-field STEM. *Ultramicroscopy* **40**, 171–180.

Cowley JM & Hudis JB (2000). Atomic-focuser imaging by graphite crystals in carbon nanoshells. *Microsc Microanal* **6**, 429–436.

Cowley JM & Iijima S (1972). Electron microscope image contrast for thin crystals. *Z Naturforsch A* **27a**, 445–451.

Cowley JM & Liu J (1993). Contrast and resolution in REM, SEM and SAM. *Surface Science* **298**, 456–467.

Cowley JM, Massover WH & Jap BK (1974). The focusing of high resolution dark-field electron microscope images. *Optik* **40**, 42–54.

Cowley JM & Moodie AF (1957). Fourier images: I - The point source. *Proc Phys Soc B* **70**, 486–496.

Cowley JM & Ou HJ (1989). Observation of microdiffraction patterns with a dedicated STEM instrument. *J Electron Microsc Tech* **11**, 143–154.

Cowley JM & Pogany AP (1968). Diffuse scattering in electron diffraction patterns. I. General theory and computational methods. *Acta Crystallogr A* **24**, 109–116.

Cowley JM, Smith DJ & Sussex GA (1970). Application of a high voltage transmission scanning electron microscope. In *Scanning Electron Microscopy, 1970. Proceedings of the 3rd Annual Scanning Electron Microscope Symposium*, IIT Research Institute, pp. 13–16.

Cowley JM & Spence JCH (1979). Innovative imaging and microdiffraction in STEM. *Ultramicroscopy* **3**, 433–438.

Cowley JM, Spence JCH & Smirnov VV (1997). The enhancement of electron microscope resolution by use of atomic focusers. *Ultramicroscopy* **68**, 135–148.

Cowley JM & Strojnik A (1968). A 600 kV transmission scanning electron microscope. In *Electron Microscopy, 1968. Proceedings of the 4th European Regional Conference on Electron Microscopy*, Rome, pp. 71–72.

Cowley JM & Strojnik A (1969). A 600 kV transmission scanning electron microscope. In *Scanning Electron Microscopy, 1969. Proceedings of the 2nd Annual Scanning Electron Microscopy Symposium*, IIT Research Institute, pp. 13–17.

Downloaded from https://www.cambridge.org/core. IP address: 68.98.49.119, on 04 Sep 2021 at 06:14:57, subject to the Cambridge Core terms of use, available at https://www.cambridge.org/core/terms. https://doi.org/10.1017/S1431927621012125

Cowley JM & Walker DJ (1981). Reconstruction from in-line holograms by digital processing. *Ultramicroscopy* **6**, 71–76.
Cremer C & Cremer T (1978). Considerations on a laser-scanning-microscope with high resolution and depth of field. *Microsc Acta* **81**, 31–44.
Crewe AV (1963). A new kind of scanning microscope. *J Microsc* **2**, 369–371.
Crewe AV (1966). Scanning electron microscopes-is high resolution possible? *Science* **154**, 729–738.
Crewe AV (1971). High resolution scanning microscopy of biological specimens. *Philos Trans R Soc B* **261**, 61–70.
Crewe AV (1974). Scanning-transmission electron-microscopy. *J Microsc* **100**, 247–259.
Crewe AV (1979). Direct imaging of single atoms and molecules using the STEM. *Chem Scr* **14**, 17–20.
Crewe AV (1980). The sextupole as corrector. *Electron Microsc* **1**, 36–37.
Crewe AV (1982). A system for the correction of axial aperture aberrations in electron lenses. *Optik* **60**, 271–281.
Crewe AV (1983*a*). High-resolution scanning-transmission electron-microscopy. *Science* **221**, 325–330.
Crewe AV (1983*b*). Multiple sextupole system for the correction of third and higher order aberration. US Patent 4,389,571.
Crewe AV (1995). Limits of electron probe formation. *J Microsc* **178**, 93–100.
Crewe AV (2004). Some Chicago aberrations. *Microsc Microanal* **10**, 414–419.
Crewe AV (2009). The work of Albert Victor Crewe on the scanning transmission electron microscope and related topics. *Adv Imaging Electron Phys* **159**, 1–61.
Crewe AV, Cohen D & Meads P (1968*a*). A multipole element for the correcting of spherical aberration. *Proc. 4th Reg. Conf. Electron. Microsc. I*, p. 183.
Crewe AV, Eggenberger DN, Wall J & Welter LM (1968*b*). Electron gun using a field emission source. *Rev Sci Inst* **39**, 576–583.
Crewe AV, Isaacson M & Johnson D (1969). A simple scanning electron microscope. *Rev Sci Instrum* **40**, 241–246.
Crewe AV, Isaacson M & Johnson D (1971*a*). A high resolution electron spectrometer for use in transmission scanning electron microscopy. *Rev Sci Instrum* **42**, 411–420.
Crewe AV, Isaacson M & Johnson D (1971*b*). Electron energy loss spectra of nucleic acid bases. *Nature* **231**, 262–263.
Crewe AV & Jiye X (1985). Correction of spherical and coma aberrations with a sextupole–round lens–sextupole system. *Optik* **69**, 141–146.
Crewe AV, Langmore JP & Isaacson MS (1975). Resolution and contrast in the STEM. In *Physical Aspects of Electron Microscopy and Microbeam Analysis*, Siegel BM & Beaman DR (Eds.), pp. 47–62. New York, NY: John Wiley & Sons.
Crewe AV & Wall J (1970). A scanning microscope with 5 Å resolution. *J Mol Biol* **48**, 375–393.
Crewe AV, Wall J & Langmore J (1970). Visibility of single atoms. *Science* **168**, 1338–1340.
Crewe AV, Wall J & Welter LM (1968*c*). A high-resolution scanning transmission electron microscope. *J Appl Phys* **39**, 5861–5868.
Cueva P, Hovden R, Mundy JA, Xin HL & Muller DA (2012). Data processing for atomic resolution electron energy loss spectroscopy. *Microsc Microanal* **18**, 667–675.
Cui J, Yao Y, Wang YG, Shen X & Yu RC (2017). The origin of atomic displacements in HAADF images of the tilted specimen. *Ultramicroscopy* **182**, 156–162.
Daberkow I, Herrmann KH & Lenz F (1993). A configurable angle-resolving detector system in STEM. *Ultramicroscopy* **50**, 75–82.
Dabov K, Foi A, Katkovnik V & Egiazarian K (2007). Image denoising by sparse 3-D transform-domain collaborative filtering. *IEEE Trans Image Process* **16**, 2080–2095.
D'Alfonso AJ, Freitag B, Klenov D & Allen LJ (2010). Atomic-resolution chemical mapping using energy-dispersive X-ray spectroscopy. *Phys Rev B* **81**, 100101(R).
Das S, Tang YL, Hong Z, Gonçalves MAP, McCarter MR, Klewe C, Nguyen KX, Gómez-Ortiz F, Shafer P, Arenholz E, Stoica VA, Hsu S-L, Wang B, Ophus C, Liu JF, Nelson CT, Saremi S, Prasad B, Mei AB, Schlom DG, Íñiguez J, García-Fernández P, Muller DA, Chen LQ, Junquera J, Martin LW & Ramesh R (2019). Observation of room-temperature polar skyrmions. *Nature* **568**, 368–372.
Davidovits P & Egger MD (1969). Scanning laser microscope. *Nature* **223**, 831.
Davidovits P & Egger MD (1971). Scanning laser microscope for biological investigations. *Appl Opt* **10**, 1615–1619.
Davisson C & Germer LH (1927). The scattering of electrons by a single crystal of nickel. *Nature* **119**, 558–560.
De Backer A, Martinez GT, MacArthur KE, Jones L, Béché A, Nellist PD & Van Aert S (2015). Dose limited reliability of quantitative annular dark field scanning transmission electron microscopy for nano-particle atom-counting. *Ultramicroscopy* **151**, 56–61.
De Backer A, Martinez GT, Rosenauer A & Van Aert S (2013). Atom counting in HAADF STEM using a statistical model-based approach: Methodology, possibilities, and inherent limitations. *Ultramicroscopy* **134**, 23–33.
De Backer A, van den Bos KHW, Van den Broek W, Sijbers J & Van Aert S (2016). StatSTEM: An efficient approach for accurate and precise model-based quantification of atomic resolution electron microscopy images. *Ultramicroscopy* **171**, 104–116.
de Broglie L (1923). Waves and quanta. *Nature* **112**, 540.
de Broglie L (1924). A tentative theory of light quanta. *Philos Mag* **47**, 446–458.
de Graaf S, Momand J, Mitterbauer C, Lazar S & Kooi BJ (2020). Resolving hydrogen atoms at metal-metal hydride interfaces. *Sci Adv* **6**, eaay4312.
de Jonge N, Peckys DB, Kremers GJ & Piston DW (2009). Electron microscopy of whole cells in liquid with nanometer resolution. *Proc Natl Acad Sci USA* **106**, 2159–2164.
Dekkers NH & De Lang H (1974). Differential phase contrast in a STEM. *Optik* **41**, 452–456.
Dellby N, Bacon NJ, Hrncirik P, Murfitt MF, Skone GS, Szilagyi ZS & Krivanek OL (2011). Dedicated STEM for 200 to 40 keV operation. *Eur Phys J Appl Phys* **54**, 33505 (p1–p11).
Dellby N, Krivanek OL, Nellist PD, Batson PE & Lupini AR (2001). Progress in aberration-corrected scanning transmission electron microscopy. *J Electron Microsc* **50**, 177–185.
den Dekker AJ, Gonnissen J, De Backer A, Sijbers J & Van Aert S (2013). Estimation of unknown structure parameters from high-resolution (S) TEM images: What are the limits? *Ultramicroscopy* **134**, 34–43.
den Dekker AJ, Van Aert S, van den Bos A & Van Dyck D (2005). Maximum likelihood estimation of structure parameters from high resolution electron microscopy images. Part I: A theoretical framework. *Ultramicroscopy* **104**, 83–106.
DeRocher KA, Smeets PJM, Goodge BH, Zachman MJ, Balachandran PV, Stegbauer L, Cohen MJ, Gordon LM, Rondinelli JM, Kourkoutis LF & Joester D (2020). Chemical gradients in human enamel crystallites. *Nature* **583**, 66–71.
De Rosier DJ & Klug A (1968). Reconstruction of three dimensional structures from electron micrographs. *Nature* **217**, 130–134.
De Ruijter W (1995). Imaging properties and applications of slow-scan charge-coupled device cameras suitable for electron microscopy. *Micron* **26**, 247–275.
Dickson RM, Cubitt AB, Tsien RY & Moerner WE (1997). On/off blinking and switching behavior of single molecules of Green fluorescent protein. *Nature* **388**, 355–358.
Dinges C, Kohl H & Rose H (1994). High-resolution imaging of crystalline objects by hollow-cone illumination. *Ultrmicroscopy* **55**, 91–100.
dos Reis R, Yang H, Ophus C, Ercius P, Bizarri G, Perrodin D, Shalapska T, Bourret E, Ciston J & Dahmen U (2018). Determination of the structural phase and octahedral rotation angle in halide perovskites. *Appl Phys Lett* **112**, 071901.
Dowell WCT (1963). Das elektronenmikroskopische Bild von Netzbenenscharen und sein Kontrast. *Optik* **20**, 535–568.
Drake, S (2003). *Galileo at Work: His Scientific Biography*. Mineola (N.Y.): Dover Publications.
Dubochet J, Adrian M, Chang JJ, Homo JC, Lepault J, McDowall AW & Schultz P (1988). Cryo-electron microscopy of vitrified specimens. *Q Rev Biophys* **21**, 129–228.
Dunin-Borkowski RE & Cowley JM (1999). Simulations for imaging with atomic focusers. *Acta Crystallogr A* **55**, 119–126.
Dwyer C (2013). Atomic-resolution core-level spectroscopy in the scanning transmission electron microscope. *Adv Imaging Electron Phys* **175**, 145–199.

Downloaded from https://www.cambridge.org/core. IP address: 68.98.49.119, on 04 Sep 2021 at 06:14:57, subject to the Cambridge Core terms of use, available at https://www.cambridge.org/core/terms. https://doi.org/10.1017/S1431927621012125

Dwyer C (2017). Prospects of spatial resolution in vibrational electron energy loss spectroscopy: Implications of dipolar scattering. *Phys Rev B* **96**, 224102.
Dycus JH, Xu W, Sang X, D'Alfonso AJ, Chen Z, Weyland M, Allen LJ, Findlay SD & LeBeau JM (2016). Influence of experimental conditions on atom column visibility in energy dispersive X-ray spectroscopy. *Ultramicroscopy* **171**, 1–7.
Dyke WP, Trolan JK, Dolan WW & Barnes G (1953). The field emitter: Fabrication, electron microscopy, and electric field calculations. *J Appl Phys* **5**, 570–576.
Earney JJ (1971). Phonon scattering of fast electrons by crystals. *Philos Mag* **23**, 577–583.
Egerton RF (2013). Control of radiation damage in the TEM. *Ultramicroscopy* **127**, 100–108.
Egerton RF (2014). Choice of operating voltage for a transmission electron microscope. *Ultramicroscopy* **145**, 85–93.
Egerton RF (2019). Radiation damage to organic and inorganic specimens in the TEM. *Micron* **119**, 72–87.
Egerton RF, Li P & Malac M (2004). Radiation damage in the TEM and SEM. *Micron* **35**, 399–409.
Egerton RF, McLeod R, Wang F & Malac M (2010). Basic questions related to electron-induced sputtering in the TEM. *Ultramicroscopy* **110**, 991–997.
Elad N, Bellapadrona G, Houben L, Sagi I & Elbaum M (2017). Detection of isolated protein-bound metal ions by single-particle cryo-STEM. *Proc Natl Acad Sci USA* **114**, 11139–11144.
Engel A (2009). Scanning transmission electron microscopy: Biological applications. *Adv Imaging Electron Phys* **159**, 357–387.
Engel A, Wiggins JW & Woodruff DC (1974). Comparison of calculated images generated by 6 modes of transmission electron-microscopy. *J Appl Phys* **45**, 2739–2747.
Erni R (2014). *Aberration-Corrected Imaging in Transmission Electron Microscopy: An Introduction*, 2nd ed. London: Imperial College Press.
Erni R, Rossell MD, Kisielowski C & Dahmen U (2009). Atomic-resolution imaging with a sub-50-pm electron probe. *Phys Rev Lett* **102**, 096101.
Everhart TE & Thornley RFM (1960). Wide-band detector for micro-microampere low-energy electron currents. *J Sci Instrum* **37**, 246–248.
Fan G & Ellisman MH (1993). High-sensitivity lens-coupled slow-scan CCD camera for transmission electron microscopy. *Ultramicroscopy* **52**, 21–29.
Fang S, Wen Y, Allen C, Ophus C, Han G, Kirkland A, Kaxiras E & Warner J (2019). Atomic electrostatic maps of 1D channels in 2D semiconductors using 4D scanning transmission electron microscopy. *Nat Commun* **10**, 1127.
Fatermans J, den Dekker AJ, Müller-Caspary K, Gauquelin N, Verbeeck J & Van Aert S (2020). Atom column detection from simultaneously acquired ABF and ADF STEM images. *Ultramicroscopy* **219**, 113046.
Fatermans J, den Dekker AJ, Müller-Caspary K, Lobato I, O'Leary CM, Nellist PD & Van Aert S (2018). Single atom detection from low contrast-to-noise ratio electron microscopy images. *Phys Rev Lett* **121**, 056101.
Fatermans J, Van Aert S & den Dekker AJ (2019). The maximum a posteriori probability rule for atom column detection from HAADF STEM images. *Ultramicroscopy* **201**, 81–91.
Feng B, Lugg NR, Kumamoto A, Shibata N & Ikuhara Y (2018). On the quantitativeness of grain boundary chemistry using STEM EDS: A ZrO_2 Σ9 model grain boundary case study. *Ultramicroscopy* **193**, 33–38.
Fernandez-Leiro R & Scheres SHW (2016). Unravelling biological macromolecules with cryo-electron microscopy. *Nature* **537**, 339–346.
Fertig J & Rose H (1977). A reflection on partial coherence in electron-microscopy. *Ultramicroscopy* **2**, 269–279.
Fertig J & Rose H (1979). On the theory of image formation in the electron microscope. *Optik* **54**, 165–174.
Fertig J & Rose H (1981). Resolution and contrast of crystalline objects in high-resolution scanning transmission electron microscopy. *Optik* **59**, 407–429.
Findlay SD, Huang R, Ishikawa R, Shibata N & Ikuhara Y (2017). Direct visualization of lithium via annular bright field scanning transmission electron microscopy: A review. *Microscopy* **66**, 3–14.
Findlay SD, Kohno Y, Cardamone LA, Ikuhara Y & Shibata N (2014). Enhanced light element imaging in atomic resolution scanning transmission electron microscopy. *Ultramicroscopy* **136**, 31–41.
Findlay SD & LeBeau JM (2013). Detector non-uniformity in scanning transmission electron microscopy. *Ultramicroscopy* **124**, 52–60.
Findlay SD, Saito T, Shibata N, Sato Y, Matsuda J, Asano K, Akiba E, Hirayama T & Ikuhara Y (2010*a*). Direct imaging of hydrogen within a crystalline environment. *Appl Phys Express* **3**, 116603.
Findlay SD, Shibata N, Sawada H, Okunishi E, Kondo Y & Ikuhara Y (2010*b*). Dynamics of annular bright field imaging in scanning transmission electron microscopy. *Ultramicroscopy* **110**, 903–923.
Findlay SD, Shibata N, Sawada H, Okunishi E, Kondo Y, Yamamoto T & Ikuhara Y (2009). Robust atomic resolution imaging of light elements using scanning transmission electron microscopy. *Appl Phys Lett* **95**, 191913.
Forbes BD, D'Alfonso AJ, Williams REA, Srinivasan R, Fraser HL, McComb DW, Freitag B, Klenov DO & Allen LJ (2012). Contribution of thermally scattered electrons to atomic resolution elemental maps. *Phys Rev B* **86**, 024108.
Forbes BD, Martin AV, Findlay SD, D'Alfonso AJ & Allen LJ (2010). Quantum mechanical model for phonon excitation in electron diffraction and imaging using a Born-Oppenheimer approximation. *Phys Rev B* **82**, 104103.
Fowler RH & Nordheim L (1928). Electron emission in intense electric fields. *Proc R Soc Lond A* **119**, 173–181.
Frank J (2016). Generalized single-particle cryo-EM — A historical perspective. *Microscopy* **65**, 3–8.
Gajdardziska-Josifovska M, Weiss JK & Cowley JM (1995). Studies of Mo/Si multilayers with coherent electron beams. *Ultramicroscopy* **58**, 65–78.
Gao P, *et al.* (2018). Picometer-scale atom position analysis in annular bright-field STEM imaging. *Ultramicroscopy* **184**, 177–187.
Gao P, Kumamoto A, Ishikawa R, Lugg NR, Shibata N & Ikuhara Y (2016*a*). Misalignment induced artifacts in quantitative annular bright-field imaging. *Microsc Microanal* **22**, 888–889.
Gao P, Liu H-J, Huang Y-L, Chu Y-H, Ishikawa R, Feng B, Jiang Y, Shibata N, Wang E-G & Ikuhara Y (2016*b*). Atomic mechanism of polarization-controlled surface reconstruction in ferroelectric thin films. *Nat Commun* **7**, 11318.
Gao W, Addiego C, Wang H, Yan X, Hou Y, Ji D, Heikes C, Zhang Y, Li L, Huyan H, Blum T, Aoki T, Nie Y, Schlom DG, Wu R & Pan X (2019). Real-space charge-density imaging with sub-Ångström resolution by four-dimensional electron microscopy. *Nature* **575**, 480–484.
García de Abajo FJ (2010). Optical excitations in electron microscopy. *Rev Mod Phys* **82**, 209.
Gemmell DS (1974). Channeling and related effects in the motion of charged particles through crystals. *Rev Mod Phys* **46**, 129227.
Gilbert P (1972). Iterative methods for the three-dimensional reconstruction of an object from projections. *J Theor Biol* **36**, 105–117.
Gomer R (1961). *Field Emission and Field Ionization*. New York: Oxford Univ. Press.
Goodge BH, Baek DJ & Kourkoutis LF (2020). Atomic-resolution elemental mapping at cryogenic temperatures enabled by direct electron detection. arXiv:200709747.
Gordon R, Bender R & Herman GT (1970). Algebraic reconstruction techniques (ART) for three-dimensional electron microscopy and X-ray photography. *J Theor Biol* **29**, 471–481.
Grieb T, Mueller K, Fritz R, Schowalter M, Neugebohrn N, Knaub N, Volz K & Rosenauer A (2012). Determination of the chemical composition of GaNAs using STEM HAADF imaging and STEM strain state analysis. *Ultramicroscopy* **117**, 15–23.
Grieb T, Müller K, Fritz R, Grillo V, Schowalter M, Volz K & Rosenauer A (2013). Quantitative chemical evaluation of dilute GaNAs using ADF STEM: Avoiding surface strain induced artifacts. *Ultramicroscopy* **129**, 1–9.
Grillo V (2009*a*). An advanced study of the response of ADF detector. *J Phys: Conf Ser* **326**, 012036.
Grillo V (2009*b*). The effect of surface strain relaxation on HAADF imaging. *Ultramicroscopy* **109**, 1453–1464.
Grillo V, Mueller K, Volz K, Glas F, Grieb T & Rosenauer A (2011). Strain, composition and disorder in ADF imaging of semiconductors. *J Phys: Conf Ser* **326**, 012006.
Gu L, Xiao D, Hu Y-S, Li H & Ikuhara Y (2015). Atomic-scale structure evolution in a quasi-equilibrated electrochemical process of electrode materials for rechargeable batteries. *Adv Mater* **27**, 2134–2149.

Downloaded from https://www.cambridge.org/core. IP address: 68.98.49.119, on 04 Sep 2021 at 06:14:57, subject to the Cambridge Core terms of use, available at https://www.cambridge.org/core/terms. https://doi.org/10.1017/S1431927621012125

Gu L, Zhu C, Li H, Yu Y, Li C, Tsukimoto S, Maier J & Ikuhara Y (2011). Direct observation of lithium staging in partially delithiated $LiFePO_4$ at atomic resolution. *J Am Chem Soc* **133**, 4661–4663.

Hachtel JA, Huang J, Popovs I, Jansone-Popova S, Keum JK, Jakowski J, Lovejoy TC, Dellby N, Krivanek OL & Idrobo JC (2019). Identification of site-specific isotopic labels by vibrational spectroscopy in the electron microscope. *Science* **363**, 525–528.

Hachtel JA, Lupini AR & Idrobo JC (2018). Exploring the capabilities of monochromated electron energy loss spectroscopy in the infrared regime. *Sci Rep* **8**, 5637. doi:10.1038/s41598-018-23805-5

Hage FS, Kepaptsoglou DM, Ramasse QM & Allen LJ (2019). Phonon spectroscopy at atomic resolution. *Phys Rev Lett* **122**, 016103.

Hage FS, Radtke G, Kepaptsoglou DM, Lazzeri M & Ramasse QM (2020*a*). Single-atom vibrational spectroscopy in the scanning transmission electron microscope. *Science* **367**, 1124–1127.

Hage FS, Ramasse QM & Allen LJ (2020*b*). Contrast reversal in atomic-scale phonon spectroscopic imaging. *Phys Rev B* **102**, 214111.

Haider M, Braunshausen G & Schwan E (1995). Correction of the spherical aberration of a 200 kV TEM by means of a hexapole-corrector. *Optik* **99**, 167–179.

Haider M, Epstein A, Jarron P & Boulin C (1994). A versatile, software configurable multichannel STEM detector for angle-resolved imaging. *Ultramicroscopy* **54**(1), 41–59.

Haider M, Uhlemann S, Schwan E & Kabius B (1997). Development of a spherical corrected 200 kV TEM: Current state of the project and results obtained so far. *Optik* **106**, S7.

Haider M, Uhlemann S, Schwan E, Rose H, Kabius B & Urban K (1998). Electron microscopy image enhanced. *Nature* **392**, 768–769.

Haider M, Uhlemann S & Zach J (2000). Upper limits for the residual aberrations of a high-resolution aberration-corrected STEM. *Ultramicroscopy* **81**, 163–175.

Hainfeld JF (1987). A small gold-conjugated antibody label: Improved resolution for electron microscopy. *Science* **236**, 450–453.

Hall CR (1965). Scattering of high energy electrons by thermal vibrations of crystals. *Philos Mag* **12**, 815–826.

Hall CR & Hirsch PB (1965). Effect of thermal diffuse scattering on propagation of high energy electrons through crystals. *Proc R Soc Lond A* **286**, 158–177.

Hammel M & Rose H (1995). Optimum rotationally symmetric detector configurations for phase-contrast imaging in scanning transmission electron microscopy. *Ultramicroscopy* **58**, 403–415.

Han Y, Nguyen K, Cao M, Cueva P, Xie S, Tate MW, Purohit P, Gruner SM, Park J & Muller DA (2018). Strain mapping of two-dimensional heterostructures with subpicometer precision. *Nano Lett* **18**, 3746–3751.

Hawkes PW (1980). Methods of computing optical properties and combating aberrations for low-intensity beams. *Adv Electron Electron Phys Suppl* **13A**, 45–157.

Hawkes PW (2009*a*). Aberration correction past and present. *Philos Trans R Soc A* **367**, 3637–3664.

Hawkes PW (2009*b*). Two commercial STEMs: The Siemens ST100 F and the AEI STEM-1. *Adv Imaging Electron Opt* **159**, 187–219.

Hawkes PW (2015). The correction of electron lens aberrations. *Ultramicroscopy* **156**, A1–64.

Hawkes PW (1992). *The Electron Microscope as a Structure Projector. In* Electron Tomography: Three-Dimensional Imaging with the Transmission Electron Microscope, Frank, J (Ed.), pp. 17–39. New York (N.Y.): Plenum.

Hawkes PW & Krivanek OL (2019). Aberration correctors, monochromators, spectrometers. In *Springer Handbook of Microscopy*. Hawkes, PW and Spence, JCH (eds). New York (N.Y.): Springer.

Hegerl R & Hoppe W (1970). Dynamic theory of crystalline structure analysis by electron diffraction in inhomogeneous primary wave field. *Ber Bunsenges Phys Chem* **74**, 1148–1154.

Hegerl R & Hoppe W (1972). Phase evaluation in generalized diffraction (ptychography). In *Proc. Fifth Congress in Electron Microscopy (Manchester). Inst Phys Conf Ser*., vol. **14**, Glauert AM (Ed.), pp. 628–629. London and Bristol: Institute of Physics.

Heinemann K & Poppa H (1970). High-resolution electron microscope images of crystal lattice planes using conical illumination. *Appl Phys Lett* **16**, 515–516.

Heinemann K & Poppa H (1972). Selected-zone dark-field electron microscopy. *Appl Phys Lett* **20**, 122–125.

Hell SW (2003). Toward fluorescence nanoscopy. *Nat Biotechnol* **21**, 1347–1355.

Hell SW & Wichmann J (1994). Breaking the diffraction resolution limit by stimulated emission: Stimulated-emission-depletion fluorescence microscopy. *Opt Lett* **19**, 780–782.

Hillier J & Baker RF (1944). Microanalysis by means of electrons. *J Appl Phys* **15**, 663–675.

Hillyard S, Loane RF & Silcox J (1993). Annular dark-field imaging – Resolution and thickness effects. *Ultramicroscopy* **49**, 14–25.

Hillyard S & Silcox J (1993). Thickness effects in ADF STEM zone-axis images. *Ultramicroscopy* **52**, 325–334.

Hooke R (1665). *Micrographia: Or Some Physiological Descriptions of Minute Bodies Made by Magnifying Glasses, with Observations and Inquiries Thereupon*. North Chelmsford (MA): Courier Corporation.

Howie A (1979). Image-contrast and localized signal selection techniques. *J Microsc* **117**, 11–23.

Howie A, Lunington P & Tomlinson PN (1971). Channeling effects in high resolution scanning electron microscopy. *Philos Mag* **23**, 1559–1565.

Huang B, Bates M & Zhuang X (2009). Super-resolution fluorescence microscopy. *Annu Rev Biochem* **78**, 993–1016.

Huang K (1947). X-ray reflexions from dilute solid solutions. *Proc R Soc Lond Ser A Math Phys Sci* **190**, 102–117.

Huang R, Ding HC, Liang WI, Gao YC, Tang XD, He Q, Duan CG, Zhu ZQ, Chu JH, Fisher CAJ, Hirayama T, Ikuhara Y & Chu YH (2014). Atomic-scale visualization of polarization pinning and relaxation at coherent $BiFeO_3/LaAlO_3$ interfaces. *Adv Funct Mater* **24**, 793–799.

Huang R, Hitosugi T, Findlay SD, Fisher CAJ, Ikuhara YH, Moriwake H, Oki H & Ikuhara Y (2011). Real-time direct observation of Li in $LiCoO_2$ cathode material. *Appl Phys Lett* **98**, 1–4.

Hyun JK, Ercius P & Muller DA (2008). Beam spreading and spatial resolution in thick organic specimens. *Ultramicroscopy* **109**, 1–7.

Idrobo JC, Lupini AR, Feng T, Unocic RR, Walden FS, Gardiner DS, Lovejoy TC, Dellby N, Pantelides ST & Krivanek OL (2018). Temperature measurement by a nanoscale electron probe using energy gain and loss spectroscopy. *Phys Rev Lett* **120**, 095901.

Iijima S (1971). High-resolution electron microscopy of crystal lattice of titanium niobium oxide. *J Appl Phys* **42**, 5891–5893.

Inada H, Kakibayashi H, Isakozawa S, Hashimoto T, Yaguchi T & Nakamura K (2009). Cold field emission and the scanning transmission electron microscope. *Adv Imaging Electron Phys* **159**, 123–186.

Isaacson M (1972). Interaction of 25 keV electrons with the nucleic acid bases, adenine, thymine, and uracil. I. Outer shell excitation. *J Chem Phys* **56**, 1803–1812.

Isaacson M & Johnson D (1975). The microanalysis of light elements using transmitted energy loss electrons. *Ultramicroscopy* **1**, 33–52.

Isaacson M, Kopf D, Ohtsuki M & Utlaut M (1979). Atomic imaging using the dark-field annular detector in the STEM. *Ultramicroscopy* **4**, 101–104.

Isaacson M, Kopf D, Utlaut M, Parker NW & Crewe AV (1977). Direct observations of atomic diffusion by scanning transmission electron microscopy. *Proc Natl Acad Sci USA* **74**, 1802–1806.

Ishikawa R, Lupini AR, Findlay SD, Taniguchi T & Pennycook SJ (2014). Three-dimensional location of a single dopant with atomic precision by aberration-corrected scanning transmission electron microscopy. *Nano Lett* **14**, 1903–1908.

Ishikawa R, Lupini AR, Hinuma Y & Pennycook SJ (2015). Large-angle illumination STEM: Toward three-dimensional atom-by-atom imaging. *Ultramicroscopy* **151**, 122–129.

Ishikawa R, Okunishi E, Sawada H, Kondo Y, Hosokawa F & Abe E (2011). Direct imaging of hydrogen-atom columns in a crystal by annular bright-field electron microscopy. *Nat Mater* **10**, 278–281.

Ishikawa R, Pennycook SJ, Lupini AR, Findlay SD, Shibata N & Ikuhara Y (2016). Single atom visibility in STEM optical depth sectioning. *Appl Phys Lett* **109**, 163102.

Itakura M, Watanabe N, Nishida M, Daio T & Matsumura S (2013). Atomic-resolution X-ray energy-dispersive spectroscopy chemical mapping of substitutional Dy atoms in a high-coercivity neodymium magnet. *Jpn J Appl Phys* **52**, 050201.

Downloaded from https://www.cambridge.org/core. IP address: 68.98.49.119, on 04 Sep 2021 at 06:14:57, subject to the Cambridge Core terms of use, available at https://www.cambridge.org/core/terms. https://doi.org/10.1017/S1431927621012125

James EM & Browning ND (1999). Practical aspects of atomic resolution imaging and analysis in STEM. *Ultramicroscopy* **78**, 125–139.

James EM, Browning ND, Nicholls AW, Kawasaki M, Xin Y & Stemmer S (1998). Demonstration of atomic resolution Z-contrast imaging by a JEOL JEM-2010F scanning transmission electron microscope. *J Electron Microsc* **47**, 561–574.

Jeong JS, Song H, Held JT & Mkhoyan KA (2019). Subatomic channeling and helicon-type beams in $SrTiO_3$. *Phys Rev Lett* **122**, 075501.

Jesson DE & Pennycook SJ (1993). Incoherent imaging of thin specimens using coherently scattered electrons. *Proc R Soc A* **441**, 261–281.

Jesson DE & Pennycook SJ (1995). Incoherent imaging of crystals thermally scattered electrons. *Proc R Soc A* **449**, 273–293.

Jesson DE, Pennycook SJ, Baribeau JM & Houghton DC (1993*a*). Direct imaging of surface cusp evolution during strained-layer epitaxy and implications for strain relaxation. *Phys Rev Lett* **71**, 1744–1747.

Jesson DE, Pennycook SJ, Tischler JZ, Budai JD, Baribeau JM & Houghton DC (1993*b*). Interplay between evolving surface-morphology, atomic-scale growth modes, and ordering during $SixGe_{1-X}$ epitaxy. *Phys Rev Lett* **70**, 2293–2296.

Jiang N (2016). Electron beam damage in oxides: A review. *Rep Prog Phys* **79**, 016501.

Jiang Y, Chen Z, Han Y, Deb P, Gao H, Xie S, Purohit P, Tate MW, Park J, Gruner SM, Elser V & Muller DA (2018). Electron ptychography of 2D materials to deep sub-Ångström resolution. *Nature* **559**, 343–349.

Johnson JM, Im S, Windl W & Hwang J (2017). Three-dimensional imaging of individual point defects using selective detection angles in annular dark field scanning transmission electron microscopy. *Ultramicroscopy* **172**, 17–29.

Jones L & Nellist PD (2013). Identifying and correcting scan noise and drift in the scanning transmission electron microscope. *Microsc Microanal* **19**, 1050–1060.

Jones L & Nellist PD (2014). Three-dimensional optical transfer functions in the aberration-corrected scanning transmission electron microscope. *J Microsc* **254**, 47–64.

Joy DC, Newbury DE & Davidson DL (1982). Electron channeling patterns in the scanning electron microscope. *J Appl Phys* **53**, R81–122.

Kalinin SV, Lupini AR, Dyck O, Jesse S, Ziatdinov M & Vasudevan RK (2019). Lab on a beam—Big data and artificial intelligence in scanning transmission electron microscopy. *MRS Bull* **44**, 565–575.

Kalinin SV, Sumpter BG & Archibald RK (2015). Big–deep–smart data in imaging for guiding materials design. *Nat Mater* **14**, 973–980.

Kambe K (1982). Visualization of Bloch waves of high-energy electrons in high-resolution electron-microscopy. *Ultramicroscopy* **10**, 223–227.

Kambe K, Lehmpfuhl G & Fujimoto F (1974). Interpretation of electron channeling by the dynamical theory of electron diffraction. *Z Naturforschung* **29**, 1034–1044.

Kim Y-J, Tao R, Klie RF & Seidman DN (2013). Direct atomic-scale imaging of hydrogen and oxygen interstitials in pure niobium using atom-probe tomography and aberration-corrected scanning transmission electron microscopy. *ACS Nano* **7**, 732–739.

Kim Y-M, Pennycook SJ & Borisevich AY (2017). Quantitative comparison of bright field and annular bright field imaging modes for characterization of oxygen octahedral tilts. *Ultramicroscopy* **181**, 1–7.

Kimoto K (2014). Practical aspects of monochromators developed for transmission electron microscopy. *Microscopy* **63**, 337–344.

Kimoto K, Asaka T, Nagai T, Saito M, Matsui Y & Ishizuka K (2007). Element-selective imaging of atomic columns in a crystal using STEM and EELS. *Nature* **450**, 702–704.

Kimoto K & Ishizuka K (2017). Rapid measurement of low-order aberrations using Fourier transforms of crystalline Ronchigrams. *Ultramicroscopy* **180**, 59–65.

Kirkland EJ (2011). On the optimum probe in aberration corrected ADF-STEM. *Ultramicroscopy* **111**, 1523–1530.

Kirkland EJ, Loane RF & Silcox J (1987). Simulation of annular dark field STEM images using a modified multislice method. *Ultramicroscopy* **23**, 77–96.

Klar TA, Jakobs S, Dyba M, Egner A & Hell SW (2000). Fluorescence microscopy with diffraction resolution barrier broken by stimulated emission. *Proc Natl Acad Sci USA* **97**(15), 8206–8210.

Klenov DO, Findlay SD, Allen LJ & Stemmer S (2007). Influence of orientation on the contrast of high-angle annular dark-field images of silicon. *Phys Rev B* **76**, 014111.

Klenov DO & Stemmer S (2006). Contributions to the contrast in experimental high-angle annular dark-field images. *Ultramicroscopy* **106**, 889–901.

Klenov DO & Zide MO (2011). Structure of the InAlAs/InP interface by atomically resolved energy dispersive spectroscopy. *Appl Phys Lett* **99**, 141904.

Knoll M (1935). Aufladepotentiel und Sekundäremission elektronenbestrahlter Körper. *Z Tech Phys* **16**, 467–475.

Knoll M (1941). Nachweiss aufgewachsener Oxydschichten des Eisens mit dem Elektronenabtaster. *Phys Z* **42**, 120–122.

Kobayashi S, Findlay SD, Shibata N, Mizoguchi T, Sato Y, Okunishi E, Ikuhara Y & Yamamoto T (2012). Simultaneous visualization of oxygen vacancies and the accompanying cation shifts in a perovskite oxide by combining annular imaging techniques. *Appl Phys Lett* **100**, 193112.

Komaki K & Fujimoto F (1974). Quantized rosette motion of energetic electron around an atomic row in crystal. *Phys Lett A* **49**, 445–446.

Komoda T (1966). Electron microscopic observation of crystal lattices on the level with atomic dimension. *Jpn J Appl Phys* **5**, 603–607.

Komoda T & Saito S (1972). Experimental resolution limit in the secondary electron mode for a field emission source scanning electron microscope. *Proc. 5th Annual Scanning Electron Microsc. Symp.*, Chicago, p. 129.

Komoda T, Tonomura A, Ohkura A & Minamikawa Y (1972). A scanning transmission electron microscope using a field emission electron gun. *Proc. 6th Int. Conf. on X-ray Optics and Microanalysis*, pp. 483–488.

Konnert J & D'Antonio P (1986). Image reconstruction using electron microdiffraction patterns from overlapping regions. *Ultramicroscopy* **19**, 267–277.

Konnert J, D'Antonio P, Cowley JM, Higgs A & Ou HJ (1989). Determination of atomic positions using electron nanodiffraction patterns from overlapping regions: Si [110]. *Ultramicroscopy* **30**, 371–384.

Kothleitner G, Neish MJ, Lugg NR, Findlay SD, Grogger W, Hofer F & Allen LJ (2014). Quantitative elemental mapping at atomic resolution using X-ray spectroscopy. *Phys Rev Lett* **112**, 085501.

Kotula PG, Klenov DO & Von Harrach HS (2012). Challenges to quantitative multivariate statistical analysis of atomic-resolution X-ray spectral. *Microsc Microanal* **18**, 691–698.

Kourkoutis LF, Xin H , Higuchi T, Hotta Y, Lee JH, Hikita Y, Schlom DG, Hwang HY & Muller DA (2010). Atomic-resolution spectroscopic imaging of oxide interfaces. *Philos Mag* **90**, 4731–4749.

Kourkoutis LF, Parker MK, Vaithyanathan V, Schlom DG & Muller DA (2011). Direct measurement of electron channeling in a crystal using scanning transmission electron microscopy. *Phys Rev B* **84**, 075485.

Kovarik L, Stevens A, Liyu A & Browning ND (2016). Implementing an accurate and rapid sparse sampling approach for low-dose atomic resolution STEM imaging. *Appl Phys Lett* **109**, 164102.

Kreiner HJ, Bell F, Sizmann R, Harder D & Hüttl W (1970). Rosette motion in negative particle channelling. *Phys Lett A* **33**, 135–136.

Krivanek OL, Corbin GJ, Dellby N, Elston BF, Keyse RJ, Murfitt MF, Own CS, Szilagyi ZS & Woodruff JW (2008). An electron microscope for the aberration-corrected era. *Ultramicroscopy* **108**, 179–195.

Krivanek OL, Chisholm MF, Nicolosi V, Pennycook TJ, Corbin GJ, Dellby N, Murfitt MF, Own CS, Szilagyi ZS, Oxley MP, Pantelides ST & Pennycook SJ (2010*a*). Atom-by-atom structural and chemical analysis by annular dark-field electron microscopy. *Nature* **464**, 571–574.

Krivanek OL, Dellby N, Hachtel JA, Idrobo J-C, Hotz MT, Plotkin-Swing B, Bacon NJ, Bleloch AL, Corbin GJ, Hoffman MV, Meyer CE & Lovejoy TC (2019). Progress in ultrahigh energy resolution EELS. *Ultramicroscopy* **203**, 60–67.

Krivanek OL, Dellby N & Lupini AR (1999). Towards sub-Angstrom electron beams. *Ultramicroscopy* **78**, 1–11.

Krivanek OL, Dellby N, Murfitt MF, Chisholm MF, Pennycook TJ, Suenaga K & Nicolosi V (2010*b*). Gentle STEM: ADF imaging and EELS at low primary energies. *Ultramicroscopy* **110**, 935–945.

Krivanek OL, Dellby N, Spence AJ & Brown LM (1998). Spherical aberration correction in dedicated STEM. In *Electron Microscopy, 1998. Proceedings of ICEM 14*, vol. **1**, pp. 55–56.

Krivanek OL, Dellby N, Spence AJ, Camps A & Brown LM (1997*a*). Aberration correction in the STEM. *Inst Phys Conf Ser* **153**, 35–40.

Downloaded from https://www.cambridge.org/core. IP address: 68.98.49.119, on 04 Sep 2021 at 06:14:57, subject to the Cambridge Core terms of use, available at https://www.cambridge.org/core/terms. https://doi.org/10.1017/S1431927621012125

Krivanek OL, Dellby N, Spence AJ, Camps A & Brown LM (1997*b*). On-line aberration measurement and correction in STEM. *Microsc Microanal* **3** (Suppl. 2), 1171–1172.

Krivanek OL, Lovejoy TC, Dellby N, Aoki T, Carpenter RW, Rez P, Soignard E, Zhu J, Batson PE, Lagos MJ, Egerton RF & Crozier PA (2014*a*). Vibrational spectroscopy in the electron microscope. *Nature* **514**, 209–212.

Krivanek OL, Lovejoy TC, Dellby N & Carpenter RW (2013). Monochromated STEM with a 30 meV-wide, atom-sized electron probe. *Microscopy* **62**, 3–21.

Krivanek OL, Lovejoy TC, Murfitt MF, Skone G, Batson PE & Dellby N (2014*b*). Towards sub-10 meV energy resolution STEM-EELS. *J Phys Conf Ser* **522**, 012023.

Krivanek OL, Nellist PD, Dellby N, Murfitt MF & Szilagyi Z (2003). Towards sub-0.5 Å beams. *Ultramicroscopy* **96**, 229–237.

Krivanek OL, Ursin JP, Bacon NJ, Corbin GJ, Dellby N, Hrncirik P, Murfitt MF, Own CS & Szilagyi ZS (2009). High-energy-resolution monochromator for aberration-corrected scanning transmission electron microscopy/electron energy-loss spectroscopy. *Philos Trans R Soc A* **367**, 3683–3697.

Kruit P & Venables JA (1988). High spatial resolution surface sensitive electron spectroscopy using a magnetic parallelizer. *Ultramicroscopy* **25**, 183–194.

Kühlbrandt W (2014). The resolution revolution. *Science* **343**, 1443–1444.

Laanait N, He Q & Borisevich AY (2019). Reconstruction of 3-D atomic distortions from electron microscopy with deep learning. arXiv:190206876.

Lagos MJ, Trügler A, Hohenester U & Batson PE (2017). Mapping vibrational surface and bulk modes in a single nanocube. *Nature* **543**, 529–532.

Lane N (2015). The unseen world: Reflections on leeuwenhoek (1677) 'concerning little animal'. *Philos Trans R Soc Lond B Biol Sci* **370**(1666), 20140344.

Langmore JP, Wall J & Isaacson MS (1973). Collection of scattered electrons in dark field electron-microscopy. I. Elastic-scattering. *Optik* **38**, 335–350.

Lazić I, Bosch EGT & Lazar S (2016). Phase contrast STEM for thin samples: Integrated differential phase contrast. *Ultramicroscopy* **160**, 265–280.

Leapman RD (2003). Detecting single atoms of calcium and iron in biological structures by electron energy-loss spectrum-imaging. *J Microsc* **210**, 5–15.

Leapman RD & Andrews SB (1992). Characterization of isolated macromolecules by combined mass mapping and electron energy loss spectroscopy. *J Microsc* **165**, 225–238.

Leapman RD & Ornberg RL (1988). Quantitative electron energy loss spectroscopy in biology. *Ultramicroscopy* **24**, 251–268.

Leary R, Saghi Z, Midgley PA & Holland DJ (2013). Compressed sensing electron tomography. *Ultramicroscopy* **131**, 70–91.

LeBeau JM, D'Alfonso AJ, Findlay SD, Stemmer S & Allen LJ (2009*a*). Quantitative comparisons of contrast in experimental and simulated bright-field scanning transmission electron microscopy images. *Phys Rev B* **80**, 214110.

LeBeau JM, Findlay SD, Allen LJ & Stemmer S (2008). Quantitative atomic resolution scanning transmission electron microscopy. *Phys Rev Lett* **100**, 206101.

LeBeau JM, Findlay SD, Wang X, Jacobson AJ, Allen LJ & Stemmer S (2009*b*). High-angle scattering of fast electrons from crystals containing heavy elements: Simulation and experiment. *Phys Rev B* **79**, 214110.

LeBeau JM & Stemmer S (2008). Experimental quantification of annular dark-field images in scanning transmission electron microscopy. *Ultramicroscopy* **108**, 1653–1658.

Lee S, Oshima Y, Hosono E, Zhou H & Takayanagi K (2013). Reversible contrast in focus series of annular bright field images of a crystalline $LiMn_2O_4$ nanowire. *Ultramicroscopy* **125**, 43–48.

Lee S, Oshima Y, Niitaka S, Takagi H, Tanishiro Y & Takayanagi K (2012). In-situ annular bright-field imaging of structural transformation of spinel LiV_2O_4 crystals into defective $Li_xV_2O_4$. *Jap J Appl Phys* **51**, 020202.

Levine E, Bell WL & Thomas G (1966). Further applications of Kikuchi diffraction patterns: Kikuchi maps. *J Appl Phys* **37**, 2141–2148.

Li Y, Li Y, Pei A, Yan K, Sun Y, Wu C-L, Joubert L-M, Chin R, Koh AL, Yu Y, Perrino J, Butz B, Chu S & Cui Y (2017). Atomic structure of sensitive battery materials and interfaces revealed by cryo-electron microscopy. *Science* **358**, 506–510.

Liberti E, Lozano JG, Osorio MP, Roberts MR, Bruce PG & Kirkland AI (2020). Quantifying oxygen distortions in lithium-rich transition-metal-oxide cathodes using ABF STEM. *Ultramicroscopy* **210**, 112914.

Lilburne M, Herd JS & Stuart LEH (1970). A pulse control circuit for use in the preparation of field emitter tips. *J Phys E: Sci Instrum* **3**, 936–937.

Lin B, Wu X, Xie L, Kang Y, Du H, Kang F, Li J & Gan L (2020). Atomic imaging of subsurface interstitial hydrogen and insights into surface reactivity of palladium hydrides. *Angew Chem Int Ed* **59**, 20348–20352.

Lin JA & Cowley JM (1986*a*). Reconstruction from in-line electron holograms by digital processing. *Ultramicroscopy* **19**, 179–190.

Lin JA & Cowley JM (1986*b*). Calibration of the operating parameters for an HB5 STEM instrument. *Ultramicroscopy* **19**, 31–42.

Lin YC, Teng P-O, Chiu P-W & Suenaga K (2015). Exploring the single atom spin state by electron spectroscopy. *Phys Rev Lett* **115**, 206803.

Lindhard J (1965). Influence of crystal lattice on the motion of energetic charged particles. *Mat Fys Medd Dan Vid Selsk* **34**, 14. (1–64).

Liu J (1990). Atomic resolution imaging in the STEM. *Proc. XII Int. Conf. Elec. Microsc.*, vol. **1**, pp. 33–34.

Liu J (2004). Advanced electron microscopy characterization of nanostructured heterogeneous catalysts. *Microsc Microanal* **10**, 55–76.

Liu J (2005). Scanning transmission electron microscopy and its application to the study of nanoparticles and nanoparticle systems. *J Electron Microsc* **54**, 251–278.

Liu J (2011). Advanced electron microscopy of metal–support interactions in supported metal catalysts. *ChemCatChem* **3**, 934–948.

Liu J (2017*a*). Aberration-corrected scanning transmission electron microscopy in single-atom catalysis: Probing the catalytically active centers. *Chin J Catal* **38**, 1460–1472.

Liu J (2017*b*). Catalysis by supported single metal atoms. *ACS Catal* **7**, 34–59.

Liu J & Allard LF (2010). Surface channeling in aberration-corrected scanning transmission electron microscopy of nanostructures. *Microsc Microanal* **16**, 425–433.

Liu J & Cowley JM (1990). High-angle ADF and high resolution SE imaging of supported catalyst clusters. *Ultramicroscopy* **34**, 119–128.

Liu J & Cowley JM (1991). Imaging with high-angle scattered electrons and secondary electrons in the STEM. *Ultramicroscopy* **37**, 50–71.

Liu J & Cowley JM (1992). Imaging dislocations with an annular dark-field detector. In *Proc. 50th Annual EMSA Meeting*, Bailey GW, Bentley J & Small JA (Eds.), pp. 1224–1225. San Francisco: San Francisco Press.

Liu J & Cowley JM (1993). High-resolution scanning transmission electron microscopy. *Ultramicroscopy* **52**, 335–346.

Liu J, Hembree GG, Sinnler GE & Venables JA (1992). High resolution auger electron spectroscopy and microscopy of a supported metal catalyst. *Surf Sci Lett* 262, 111–117.

Liu J, Hembree GG, Sinnler GE & Venables JA (1993*a*). Nanometer-resolution surface analysis with Auger electrons. *Ultramicroscopy* **52**, 369–376.

Liu J, Pan M & Spinnler GE (1993*b*). Coherent electron nanodiffraction from clean silver nano particles in a UHV STEM. *Proceedings of the 51st Annual Meeting Microscopy Society of America*, pp. 1058–1059.

Liu J, Spinnler GE, Pan P & Cowley JM (1990). STEM characterization of supported catalyst clusters. *Proc. XII Int. Conf. Elec. Microsc.*, vol. **4**, pp. 294–295.

Liu RJ & Cowley JM (1996). Dark-field and marginal imaging with a thin-annular detector in STEM. *Microsc Microanal* **2**, 9–19.

Loane RF, Kirkland EJ & Silcox J (1988). Visibility of single heavy-atoms on thin crystalline silicon in simulated annular dark-field STEM images. *Acta Crystallogr A* **44**, 912–927.

Loane RF, Xu P & Silcox J (1991). Thermal vibrations in convergent-beam electron-diffraction. *Acta Crystallogr A* **47**, 267–278.

Loane RF, Xu P & Silcox J (1992). Incoherent imaging of zone axis crystals with ADF STEM. *Ultramicroscopy* **40**, 121–138.

Lohr M, Schregle R, Jetter M, Wächter C, Müller-Caspary K, Mehrtens T, Rosenauer A, Pietzonka I, Strassburg M & Zweck J (2016). Quantitative measurements of internal electric fields with differential phase contrast microscopy on InGaN/GaN quantum well structures. *Phys Status Solidi B* **253**, 140–144.

Londoño-Calderon A, Williams DJ, Ophus C & Pettes MT (2020). 1D to 2D transition I tellurium observed by 4D electron microscopy. *Small* **16**, 2005447.

Lozano JG, Martinez GT, Jin L, Nellist PD & Bruce PG (2018). Low-dose aberration-free imaging of Li-rich cathode materials at various states of charge using electron ptychography. *Nano Lett* **18**, 6850–6855.

Downloaded from https://www.cambridge.org/core. IP address: 68.98.49.119, on 04 Sep 2021 at 06:14:57, subject to the Cambridge Core terms of use, available at https://www.cambridge.org/core/terms. https://doi.org/10.1017/S1431927621012125

Lu P, Moya JM, Yuan R & Zuo JM (2018). Studies of X-ray localization and thickness dependence in atomic-scale elemental mapping by STEM energy-dispersive X-ray spectroscopy using single-frame scanning method. *Ultramicroscopy* **186**, 23–29.

Lu P, Xiong J, Van Benthem M & Jia Q (2013). Atomic-scale chemical quantification of oxide interfaces using energy-dispersive X-ray spectroscopy. *Appl Phys Lett* **102**, 173111.

Lubkin GB (1974). High-voltage, high-resolution electron microscopes. *Phys Today* **27**, 17–18.

Lugg NR, Forbes BD, Findlay SD & Allen LJ (2015*a*). Atomic resolution imaging using electron energy-loss phonon spectroscopy. *Phys Rev B* **91**, 144108.

Lugg NR, Kothleitner G, Shibata N & Ikuhara Y (2015*b*). On the quantitativeness of EDS STEM. *Ultramicroscopy* **151**, 150–159.

Lugg NR, Neish MJ, Findlay SD & Allen LJ (2014). Practical aspects of removing the effects of elastic and thermal diffuse scattering from spectroscopic data for single crystals. *Microsc Microanal* **20**, 1078–1089.

Lupini AR (2011). The electron Ronchigram. In *Scanning Transmission Electron Microscopy, Imaging and Analysis*, Pennycook SJ & Nellist PD (Eds.), pp. 117–482. New York: Springer.

Lupini AR & Pennycook SJ (2008). Rapid autotuning for crystalline specimens from an inline hologram. *J Electron Microsc* **57**, 195–201.

Lupini AR, Wang P, Nellist PD, Kirkland AI & Pennycook SJ (2010). Aberration measurement using the Ronchigram contrast transfer function. *Ultramicroscopy* **110**, 891–898.

Lyman CE, Goldstein JI, Williams DB, Ackland DW, Von Harrach S, Nicholls AW & Statham PJ (1994). High-performance X-ray detection in a new analytical electron microscope. *J Microsc* **176**, 85–98.

MacArthur KE, Brown HG, Findlay SD & Allen LJ (2017). Probing the effect of electron channeling on atomic resolution energy dispersive X-ray quantification. *Ultramicroscopy* **182**, 264–275.

MacArthur KE, Jones LB & Nellist PD (2014). How flat is your detector? Non-uniform annular detector sensitivity in STEM quantification. *J Phys: Conf Ser* **522**, 012018.

MacArthur KE, Pennycook TJ, Okunishi E, D'Alfonso AJ, Lugg NR, Allen LJ & Nellist PD (2013). Probe integrated scattering cross sections in the analysis of atomic resolution HAADF STEM images. *Ultramicroscopy* **133**, 109–119.

Maccagnano-Zacher SE, Mkhoyan KA, Kirkland EJ & Silcox J (2008). Effects of tilt on high-resolution ADF-STEM imaging. *Ultramicroscopy* **108**, 718–726.

Mahr C, Müller-Caspary K, Grieb T, Krause FF, Schowalter M & Rosenauer A (2021). Accurate measurement of strain at interfaces in 4D-STEM: A comparison of various methods. *Ultramicroscopy* **221**, 113196.

Maiden AM & Rodenburg JM (2009). An improved ptychographical phase retrieval algorithm for diffractive imaging. *Ultramicroscopy* **109**, 1256–1262.

Mao Y, Fahimian BP, Osher SJ & Miao J (2010). Development and optimization of regularized tomographic reconstruction algorithms utilizing equally-sloped tomography. *IEEE Trans Image Process* **19**, 1259–1268.

Marko M & Rose H (2010). The contributions of Otto Scherzer (1909–1982) to the development of the electron microscope. *Microsc Microanal* **16**, 366–374.

Martin EE, Trolan JK & Dyke WP (1960). Stable, high density field emission cold cathode. *J Appl Phys* **31**, 782–789.

Martinez GT, De Backer A, Rosenauer A, Verbeeck J & Van Aert S (2013). The effect of probe inaccuracies on the quantitative model-based analysis of high angle annular dark field scanning transmission electron microscopy images. *Micron* **63**, 57–63.

Martinez GT, Rosenauer A, De Backer A, Verbeeck J & Van Aert S (2014). Quantitative composition determination at the atomic level using model-based high-angle annular dark field scanning transmission electron microscopy. *Ultramicroscopy* **137**, 12–19.

Mathews WW (1953). The use of hollow-cone illumination for increasing image contrast in microscopy. *Trans Am Microsc Soc* **2**, 190–195.

Matsumoto T, So Y, Kohno Y, Sawada H, Ikuhara Y & Shibata N (2016). Direct observation of Σ7 domain boundary core structure in magnetic skyrmion lattice. *Sci Adv* **2**, e1501280.

McMullan D (1989). SEM-past, present and future. *J Microsc* **155**, 373–392.

McMullan D (1990). The prehistory of scanned image microscopy, Part 1: Scanned optical microscopes. *Proc R Microsc Soc* **25**, 127–131.

McMullan D (1995). Scanning electron microscopy 1928–1965. *Scanning* **17**, 175–185.

McMullan G, Faruqi AR, Clare D & Henderson R (2014). Comparison of optimal performance at 300 keV of three direct electron detectors for use in low dose electron microscopy. *Ultramicroscopy* **147**, 156–163.

Mehrtens T, Schowalter M, Tytko D, Choi P, Raabe D, Hoffmann L, Jönen H, Rossow U, Hangleiter A & Rosenauer A (2013). Measurement of the indium concentration in high indium content InGaN layers by scanning transmission electron microscopy and atom probe tomography. *Appl Phys Lett* **102**, 132112.

Mendis SK, Kemeny SE, Gee RC, Pain B, Staller CO, Kim Q & Fossum ER (1997). CMOS active pixel image sensors for highly integrated imaging systems. *IEEE J Solid-State Circuits* **32**, 187–197.

Menter J (1956). The direct study by electron microscopy of crystal lattices and their imperfections. *Proc R Soc Lond A* **236**, 119–135.

Miao J, Ercius P & Billinge SJL (2016). Atomic electron tomography: 3D structures without crystals. *Science* **353**, aaf2157 (p1–p9).

Miao J, Förster F & Levi O (2005). Equally sloped tomography with oversampling reconstruction. *Phys Rev B* **72**, 052103.

Midgley PA & Dunin-Borkowski RE (2009). Electron tomography and holography in materials science. *Nat Mater* **8**, 271–280.

Midgley PA & Weyland M (2003). 3D electron microscopy in the physical sciences: The development of Z-contrast and EFTEM tomography. *Ultramicroscopy* **96**, 413–431.

Minor AM, Denes P & Muller DA (2019). Cryogenic electron microscopy for quantum science. *MRS Bull* **44**, 961–966.

Minsky M (1957). Microscopy apparatus. US Patent 3.013.467, filed 7 November 1957, granted 19 December 1961.

Minsky M (1988). Memoir on inventing the confocal scanning microscope. *Scanning* **10**, 128–138.

Misell DL, Stroke GW & Halioua M (1974). Coherent and incoherent imaging in scanning-transmission electron-microscope. *J Phys D* **7**, L113–L117.

Mitsuishi K, Takeguchi M, Yasuda H & Furuya K (2001). New scheme of calculation of annular dark-field STEM image including both elastically diffracted and TDS waves. *J Electron Microsc* **50**, 157–162.

Moerner WE & Kador L (1989). Optical detection and spectroscopy of single molecules in a solid. *Phys Rev Lett* **62**, 2535–2538.

Monkman EJ, Adamo C, Mundy JA, Shai DE, Harter JW, Shen D, Burganov B, Muller DA, Schlom DG & Shen KM (2012). Quantum many-body interactions in digital oxide superlattices. *Nat Mater* **11**, 855–885.

Morishita S, Ishikawa R, Kohno Y, Sawada H, Shibata N & Ikuhara Y (2018). Attainment of 40.5 pm spatial resolution using 300 kV scanning transmission electron microscope equipped with fifth-order aberration corrector. *Microscopy* **67**, 46–50.

Muller DA, Kourkoutis LF, Murfitt M, Song JH, Hwang HY, Silcox J, Dellby N & Krivanek OL (2008). Atomic-scale chemical imaging of composition and bonding by aberration-corrected microscopy. *Science* **319**, 1073–1076.

Muller DA (2009). Structure and bonding at the atomic scale by scanning transmission electron microscopy. *Nat Mater* **8**, 263–270.

Muller DA, Edwards B, Kirkland EJ & Silcox J (2001). Simulation of thermal diffuse scattering including a detailed phonon dispersion curve. *Ultramicroscopy* **86**, 371–380.

Muller DA, Kirkland EJ, Thomas MG, Grazul JL, Fitting L & Weyland M (2006). Room design for high-performance electron microscopy. *Ultramicroscopy* **106**, 1033–1040.

Muller DA, Tzou Y, Raj R & Silcox J (1993). Mapping sp^2 and sp^3 states of carbon at sub-nanometre spatial resolution. *Nature* **366**, 725–727.

Müller-Caspary K, Krause FF, Winkler F, Béché A, Verbeeck J, Van Aert S & Rosenauer A (2019). Comparison of first moment STEM with conventional differential phase contrast and the dependence on electron dose. *Ultramicroscopy* **203**, 95–104.

Müller-Caspary K, Oppermann O, Grieb T, Krause FF, Rosenauer A, Schowalter M, Mehrtens T, Beyer A, Volz K & Potapov P (2016). Materials characterization by angle-resolved scanning transmission electron microscopy. *Sci Rep* **6**, 37146.

Downloaded from https://www.cambridge.org/core. IP address: 68.98.49.119, on 04 Sep 2021 at 06:14:57, subject to the Cambridge Core terms of use, available at https://www.cambridge.org/core/terms. https://doi.org/10.1017/S1431927621012125

Nakane T, Kotecha A, Sente A, McMullan G, Masiulis S, Brown PMGE, Grigoras IT, Malinauskaite L, Malinauskas T, Miehling J, Uchański T, Yu L, Karia D, Pechnikova EV, de Jong E, Keizer J, Bischoff M, McCormack J, Tiemeijer P, Hardwick SW, Chirgadze DY, Murshudov G, Aricescu AR & Scheres SHW (2020). Single-particle cryo-EM at atomic resolution. *Nature* **587**, 152–156.

Nellist PD (2007). Scanning transmission electron microscopy. *Sci Microsc* **1**, 65–132.

Nellist PD (2011). The principles of STEM imaging. In *Scanning Transmission Electron Microscopy*, Pennycook SJ & Nellist PD (Eds.), pp. 91–115. Berlin: Springer.

Nellist PD (2017). Electron-optical sectioning for three-dimensional imaging of crystal defect structures. *Mater Sci Semicond Process* **65**, 18–23.

Nellist PD (2019). Scanning transmission electron microscopy. In *Springer Handbook of Microscopy. Springer Handbooks*, Hawkes PW & Spence JCH (Eds.). Cham: Springer.

Nellist PD, Chisholm MF, Dellby N, Krivanek OL, Murfitt MF, Szilagyi ZS, Lupini AR, Borisevich A, Sides WH & Pennycook SJ (2004). Direct sub-Ångstrom imaging of a crystal lattice. *Science* **305**, 1741–1742.

Nellist PD, McCallum B & Rodenburg JM (1995). Resolution beyond the "information limit" in transmission electron microscopy. *Nature* **374**, 630–632.

Nellist PD & Pennycook SJ (1996). Direct imaging of the atomic configuration of ultradispersed catalysts. *Science* **274**, 413–415.

Nellist PD & Pennycook SJ (1999). Incoherent imaging using dynamically scattered coherent electrons. *Ultramicroscopy* **78**, 111–124.

Nellist PD, Pennycook SJ, *et al.* (2000). The principles and interpretation of annular dark-field Z-contrast imaging. In *Advances in Imaging and Electron Physics*, vol. **113**, Kazan B (Ed.), pp. 147–203. New York: Elsevier.

Nicholls D, Lee J, Amari H, Stevens AJ, Mehdi BL & Browning ND (2020). Minimizing damage in high resolution scanning transmission electron microscope images of nanoscale structures and processes. *Nanoscale* **12**, 21248–21254.

Nicoletti O, de la Peña F, Leary RK, Holland DJ, Ducati C & Midgley PA (2013). Three-dimensional imaging of localized surface plasmon resonances of metal nanoparticles. *Nature* **502**, 80–84.

Norton DP, Lowndes DH, Pennycook SJ & Budai JD (1991). Depression and broadening of the superconducting transition in superlattices based on $YBa_2Cu_3O_{7-\delta}$ – Influence of the barrier layers. *Phys Rev Lett* **67**, 1358–1361.

Oatley CW (1982). The early history of the scanning electron microscope. *J Appl Phys* **53**, R1–R13.

Oatley CW, Nixon WC & Pease RFW (1965). Scanning electron microscopy. *Adv Electronics Electron Phys* **21**, 181–247.

Ohtsuka M, Yamazaki T, Kotaka Y, Hashimoto I & Watanabe K (2012). Imaging of light and heavy atomic columns by spherical aberration corrected middle-angle bright-field STEM. *Ultramicroscopy* **120**, 48–55.

O'Keefe M (1992). Resolution in high-resolution electron microscopy. *Ultramicroscopy* **47**, 282–297.

O'Keefe MA & Allard LF (2004). A standard for sub-Ångström metrology of resolution in aberration-corrected transmission electron microscopes. *Microsc Microanal* **10**(Suppl. 2), 1002–1003.

O'Keefe MA, Allard LF & Blom DA (2005). HRTEM imaging of atoms at sub-Ångström resolution. *J Electron Microsc* **54**, 169–180.

Okunishi E, Ishikawa I, Sawada H, Hosokawa F, Hori M & Kondo Y (2009). *Visualization of light elements at ultrahigh resolution by STEM annular bright field microscopy. Microsc Microanal* **15**, 164–165.

Ooe K, Seki T, Ikuhara Y & Shibata N (2019). High contrast STEM imaging for light elements by an annular segmented detector. *Ultramicroscopy* **202**, 148–155.

Ooe K, Seki T, Ikuhara Y & Shibata N (2021). Ultra-high contrast STEM imaging for segmented/pixelated detectors by maximizing the signal-to-noise ratio. *Ultramicroscopy* **220**, 113133.

Ophus C (2019). Four-dimensional scanning transmission electron microscopy (4D STEM): From scanning nanodiffraction to ptychography and beyond. *Microsc Microanal* **25**, 563–582.

Ophus C, Ciston J & Nelson CT (2016*a*). Correcting nonlinear drift distortion of scanning probe and scanning transmission electron microscopies from image pairs with orthogonal scan directions. *Ultramicroscopy* **162**, 1–9.

Ophus C, Ciston J, Pierce J, Harvey TR, Chess J, McMorran BJ, Czarnik C, Rose HH & Ercius P (2016*b*). Efficient linear phase contrast in scanning transmission electron microscopy with matched illumination and detector interferometry. *Nat Commun* **7**, 10719.

Orchard G & Nation B (2014). *Cell Structure & Function*. Oxford, UK: Oxford University Press.

Oshima Y, Sawada H, Hosokawa F, Okunishi E, Kaneyama T, Kondo Y, Niitaka S, Takagi H, Tanishiro Y & Takayanagi K (2010). Direct imaging of lithium atoms in LiV_2O_4 by spherical aberration-corrected electron microscopy. *J Electron Microsc* **59**, 457–461.

Ottensmeyer FP & Andrew JW (1980). High-resolution microanalysis of biological specimens by electron energy-loss spectroscopy and by electron spectroscopic imaging. *J Ultrastruct Res* **72**, 336–348.

Oveisi E, Spadaro MC, Rotunno E, Grillo V & Hébert C (2019). Insights into image contrast from dislocations in ADF-STEM. *Ultramicroscopy* **200**, 139–148.

Oxley MP, Varela M, Pennycook TJ, van Benthem K, Findlay SD, D'Alfonso AJ, Allen LJ & Pennycook SJ (2007). Interpreting atomic-resolution spectroscopic images. *Phys Rev B* **76**, 064303.

Pan M, Cowley JM & Chan IY (1990). Study of highly dispersed Pt in Y-zeolites by STEM and electron microdiffraction. *Ultramicroscopy* **34**, 93–101.

Pease RFW & Nixon WJ (1965). High resolution scanning electron microscopy. *J Sci Instrum* **42**, 81–85.

Pekin TC, Ding J, Gammer C, Ozdol B, Ophus C, Asta M, Ritchie RO & Minor AM (2019). Direct measurement of nanostructural change during in situ deformation of a bulk metallic glass. *Nat Commun* **10**, 2445.

Peng Y, Oxley MP, Lupini AR, Chisholm MF & Pennycook SJ (2008). Spatial resolution and information transfer in scanning transmission electron microscopy. *Microsc Microanal* **14**, 36–47.

Pennycook SJ (1989*a*). Z-contrast STEM for materials science. *Ultramicroscopy* **30**, 58–69.

Pennycook SJ (1989*b*). High-resolution imaging with large-angle elastically scattered electrons. *EMSA Bull* **19**, 67–74.

Pennycook SJ (2017). The impact of STEM aberration correction on materials science. *Ultramicroscopy* **180**, 22–33.

Pennycook SJ & Boatner LA (1988). Chemically sensitive structure-imaging with a scanning-transmission electron-microscope. *Nature* **336**, 565–567.

Pennycook SJ & Jesson DE (1990). High-resolution incoherent imaging of crystals. *Phys Rev Lett* **64**, 938–941.

Pennycook SJ & Jesson DE (1991). High-resolution Z-contrast imaging of crystals. *Ultramicroscopy* **37**, 14–38.

Pennycook SJ & Jesson DE (1992). Atomic resolution Z-contrast imaging of interfaces. *Acta Metall Mater* **40**, S149–S159.

Pennycook SJ & Narayan J (1985). Atom location by axial-electron-channeling analysis. *Phys Rev Lett* **54**, 1543–1546.

Pennycook SJ & Nellist PD (Eds.) (2011). *Scanning Transmission Electron Microscopy: Imaging and Analysis*. New York: Springer.

Perovic DD, Howie A & Rossouw CJ (1993*a*). On the image contrast from dislocations in high-angle annular dark-field scanning transmission electron microscopy. *Philos Mag Lett* **67**, 261–272.

Perovic DD, Rossouw CJ & Howie A (1993*b*). Imaging elastic strains in high-angle annular dark field scanning transmission electron microscopy. *Ultramicroscopy* **52**, 353–359.

Phillips PJ, De Graef M, Kovarik L, Agrawal A, Windl W & Mills MJ (2012). Atomic-resolution defect contrast in low angle annular dark-field STEM. *Ultramicroscopy* **116**, 47–55.

Nilsson Pingel T, Jørgensen M, Yankovich AB, Grönbeck H & Olsson E (2018). Influence of atomic site-specific strain on catalytic activity of supported nanoparticles. *Nat Commun* **9**, 2722.

Plotkin-Swing B, Corbin GJ, De Carlo S, Delby N, Hoermann C, Hoffman MV, Lovejoy TC, Meyer CE, Mittelberger A, Pantelic R, Piazza L & Krivanek OL (2020). Hybrid pixel detector for electron energy loss spectroscopy. *Ultramicroscopy* **217**, 113067.

Pogany AP & Turner PS (1968). Reciprocity in electron diffraction and microscopy. *Acta Crystallogr A* **24**, 103–109.

Pujals S, Feiner-Gracia N, Delcanale P, Voets I & Albertazzi L (2019). Super-resolution microscopy as a powerful tool to study complex synthetic materials. *Nat Rev Chem* **3**, 68–84.

Downloaded from https://www.cambridge.org/core. IP address: 68.98.49.119, on 04 Sep 2021 at 06:14:57, subject to the Cambridge Core terms of use, available at https://www.cambridge.org/core/terms. https://doi.org/10.1017/S1431927621012125

Qiao B, Wang A, Yang X, Allard LF, Jiang Z, Cui Y, Liu J, Li J & Zhang T (2011). Single-atom catalysis of CO oxidation using Pt_1/FeO_x. *Nat Chem* **3**, 634–641.

Radon J (1917). (Translated by PC Parks in 1986). On the determination of functions from their integral values along certain manifolds. *IEEE Trans Med Imaging* **5**, 170–176.

Rafferty B, Nellist PD & Pennycook SJ (2001). On the origin of transverse incoherence in Z-contrast STEM. *J Electron Microsc* **50**, 227–233.

Ramasse QM, Seabourne CR, Kepaptsoglou D-M, Zan R, Bangert U & Scott AJ (2012). Probing the bonding and electronic structure of single atom dopants in graphene with electron energy loss spectroscopy. *Nano Lett* **13**, 4989–4995.

Ramasse QM & Bleloch AL (2005). Diagnosis of aberrations from crystalline samples in scanning transmission electron microscopy. *Ultramicroscopy* **106**, 37–56.

Rayleigh L (1879). Investigations in optics, with special reference to the spectroscope. *Philos Mag* **8**(5), 261–274.

Rayleigh L (1896). On the theory of optical images, with special reference to the microscope. *Philos Mag* **42**(5), 167–195.

Rečnik A, Möbus G & Šturm S (2005). Image-warp: A real-space restoration method for high-resolution stem images using quantitative HRTEM analysis. *Ultramicroscopy* **103**, 285–301.

Retsky M (1974). Observed single atom elastic cross-sections in a scanning electron microscope. *Optik* **41**, 127–142.

Rez P, Humphreys CJ & Whelan MJ (1977). The distribution of intensity in electron diffraction patterns due to phonon scattering. *Philos Mag* **35**, 81–96.

Rez P & Singh A (2021). Lattice resolution of vibrational modes in the electron microscope. *Ultramicroscopy* **220**, 113162.

Rice SB, Koo JY, Disko MM & Treacy MMJ (1990). On the imaging of Pt atoms in zeolite frameworks. *Ultramicroscopy* **34**, 108–118.

Ritchie RH & Howie A (1988). Inelastic scattering probabilities in scanning transmission electron microscopy. *Philos Mag A* **58**, 753–767.

Robinson MT & Oen OS (1963). The channeling of energetic atoms in crystal lattices. *Appl Phys Lett* **2**, 30–32.

Rodenburg JM (1988). Properties of electron microdiffraction patterns from amorphous materials. *Ultramicroscopy* **25**, 329–344.

Rodenburg JM (1989). The phase problem, microdiffraction and wavelength-limited resolution - A discussion. *Ultramicroscopy* **27**, 413–422.

Rodenburg JM & Bates R (1992). The theory of super-resolution electron microscopy via Wigner-distribution deconvolution. *Philos Trans R Soc Lond A* **339**, 521–553.

Rodenburg JM, McCallum B & Nellist P (1993). Experimental tests on double-resolution coherent imaging via STEM. *Ultramicroscopy* **48**, 304–314.

Rodenburg JM & McMullan D (1985). The recording of microdiffraction patterns in scanning transmission electron microscopy. *J Phys E* **18**, 949–953.

Ronchi V (1964). Forty years of history of a grating interferometer. *Appl Opt* **3**, 437–451.

Rose H (1974). Phase-contrast in scanning-transmission electron-microscopy. *Optik* **39**, 416–436.

Rose H (1976). Image-formation by inelastically scattered electrons in electron microscopy. *Optik* **45**, 139–158.

Rose H (1977). Nonstandard imaging methods in electron microscopy. *Ultramicroscopy* **2**, 251–267.

Rose H (1990). Outline of a spherically corrected semiaplanatic medium-voltage transmission electron-microscope. *Optik* **85**, 19–24.

Rose H (2009). Historical aspects of aberration correction. *J Electron Microsc* **58**, 77–85.

Rose H, Haider M, Urban K & Krivanek OL (2020). Recipients of the 2020 Kavli Prize in Nanoscience "for subangstrom resolution imaging and chemical analysis using electron beams". https://kavliprize.org/.

Rose HH (2008). Optics of high-performance electron microscopes. *Sci Technol Adv Mater* **9**, 014107.

Rosenauer A, Gries K, Mueller K, Pretorious A, Schowalter M, Avramescu A, Engl K & Lutgen S (2009). Measurement of specimen thickness and composition in $Al_xGa_{1-x}N$/GaN using high-angle annular dark field images. *Ultramicroscopy* **109**, 1171–1182.

Rosenauer A, Krause FF, Müller K, Schowalter M & Mehrtens T (2014). Conventional transmission electron microscopy imaging beyond the diffraction and information limits. *Phys Rev Lett* **113**, 096101.

Rosenauer A, Mehrtens T, Mueller K, Gries K, Schowalter M, Satyam P, Bley S, Tessarek C, Hommel D, Sebald K, Seyfried M, Gutowski J, Avramescu A, Engl K & Lutgen S (2011). Composition mapping in InGaN by scanning transmission electron microscopy. *Ultramicroscopy* **111**, 1316–1327.

Rossouw CJ, Allen LJ, Findlay SD & Oxley MP (2003). Channeling effects in atomic resolution STEM. *Ultramicroscopy* **96**, 299–312.

Ruben G, Cosgriff EC, D'Alfonso AJ, Findlay SD, LeBeau JM & Allen LJ (2012). Interface location by depth sectioning using a low-angle annular dark field detector. *Ultramicroscopy* **113**, 131–138.

Ruska E (1987). The development of the electron-microscope and of electron-microscopy. *Rev Mod Phys* **59**, 627–638.

Ruska E & Knoll M (1931). Die magnetische Sammelspule für schnelle Elektronenstrahlen. *Z Tech Phys* **12**, 389–400 und 448.

Rust MJ, Bates M & Zhuang X (2006). Sub-diffraction-limit imaging by stochastic optical reconstruction microscopy (STORM). *Nat Methods* **3**, 793–795.

Sanchez AM & Cowley JM (1998). The imaging properties of atomic focusers. *Ultramicroscopy* **72**, 213–222.

Sanchez AM, Galindo PL, Kret S, Falke M, Beanland R & Goodhew PJ (2006). An approach to the systematic distortion correction in aberration-corrected HAADF images. *J Microsc* **221**, 1–7.

Sang X, Lupini A, Ding J, Kalinin SV, Jesse S & Unocic RR (2017). Precision controlled atomic resolution scanning transmission electron microscopy using spiral scan pathways. *Sci Rep* **7**, 43585.

Sang X, Lupini AR, Unocic RR, Chi M, Borisevich AY, Kalinin SV, Endeve E, Archibald RK & Jesse S (2016). Dynamic scan control in STEM: Spiral scans. *Adv Struct Chem Imaging* **2**, 6.

Sang XH & LeBeau JM (2014). Revolving scanning transmission electron microscopy: Correcting sample drift distortion without prior knowledge. *Ultramicroscopy* **138**, 28–35.

Sasaki T, Sawada H, Okunishi E, Hosokawa F, Kaneyama T, Kondo Y, Kimoto K & Suenaga K (2012). Evaluation of probe size in STEM imaging at 30 and 60 kV. *Micron* **43**, 551–556.

Sasaki T, Sawada H, Hosokawa F, Kohno Y, Tomita T, Kaneyama T, Kondo Y, Kimoto K, Sato Y & Suenaga K (2010). Performance of low-voltage STEM/TEM with delta corrector and cold field emission gun. *J Electron Microsc* **59**, S7–S13.

Savitzky BH, Baggari IE, Clement CB, Waite E, Goodge BH, Baek DJ, Sheckelton JP, Pasco C, Nair H, Schreiber NJ, Hoffman J, Admasu AS, Kim J, Cheong S-W, Bhattacharya A, Schlom DG, McQueen TM, Hovden R & Kourkoutis LF (2018). Image registration of low signal-to-noise cryo-STEM data. *Ultramicroscopy* **191**, 56–65.

Sawada H, Hosokawai F, Kaneyama T, Ishizawa T, Terao M, Kawazoe M, Sannomiya T, Tomita T, Kondo Y, Tanaka T, Oshima Y, Tanishiro Y, Yamamoto N & Takayanagi K (2007). Achieving 63 pm resolution in scanning transmission electron microscope with spherical aberration corrector. *Jpn J Appl Phys* **46**, L568–L570.

Sawada H, Sannomiya T, Hosokawa F, Nakamichi T, Kaneyama T, Tomita T, Kondo Y, Tanaka T, Oshima Y, Tanishiro Y & Takayanagi K (2008). Measurement method of aberration from Ronchigram by autocorrelation function. *Ultramicroscopy* **108**, 1467–1475.

Sawada H, Shimura N, Hosokawa F, Shibata N & Ikuhara Y (2015). Resolving 45-pm-separated Si–Si atomic columns with an aberration-corrected STEM. *Microscopy* **64**, 213–217.

Sawada H, Tanishiro Y, Ohashi N, Tomita T, Hosokawa F, Kaneyama T, Kondo Y & Takayanagi K (2009). STEM imaging of 47 pm-separated atomic columns by a spherical aberration-corrected electron microscope with a 300 kV cold field emission gun. *J Electron Microsc* **58**, 357–361.

Saxberg BEH & Saxton WO (1981). Quantum noise in 2D projections and 3D reconstructions. *Ultramicroscopy* **6**, 85–89.

Saxton WO, Jenkins WK, Freeman LA & Smith D (1978). TEM observations using bright field hollow cone illumination. *Optik (Jena)* **49**, 505–510.

Scherzer O (1936). Über einige Fehler von Elektronenlinsen. *Z Phys* **101**, 593–603.

Scherzer O (1947). Sphärische und chromatische Korrektur von Elektronenlinsen. *Optik* **2**, 114–132.

Downloaded from https://www.cambridge.org/core. IP address: 68.98.49.119, on 04 Sep 2021 at 06:14:57, subject to the Cambridge Core terms of use, available at https://www.cambridge.org/core/terms. https://doi.org/10.1017/S1431927621012125

Scherzer O (1949). The theoretical resolution limit of the electron microscope. *J Appl Phys* **20**, 20–29.

Scott MC, Chen CC, Mecklenburg M, Zhu C, Xu R, Ercius P, Dahmen U, Regan BC & Miao J (2012). Electron tomography at 2.4-ångström resolution. *Nature* **483**, 444–447.

Senga R, Suenaga K, Barone P, Morishita S, Mauri F & Pichler T (2019). Position and momentum mapping of vibrations in graphene nanostructures. *Nature* **573**, 247–250.

Septier A (2017). The struggle to overcome spherical aberration in electron optics. *Adv Imaging Electron Phys* **202**, 75–147.

Shao Z (1988). On the fifth-order aberration in a sextupole-corrected probe forming system. *Rev Sci Instrum* **59**, 2429–2437.

Sheppard JCR & Wilson T (1978). Image formation in scanning microscopes with partially coherent source and detector. *Opt Acta* **25**, 315–325.

Shibata N, Findlay SD, Kohno Y, Sawada Y, Kondo Y & Ikuhara Y (2012). Differential phase-contrast microscopy at atomic resolution. *Nat Phys* **8**, 611–615.

Shibata N, Kohno Y, Findlay SD, Sawada H, Kondo Y & Ikuhara Y (2010). New area detector for atomic-resolution scanning transmission electron microscopy. *J Electron Microsc* **59**, 473–479.

Shibata N, Seki T, Sánchez-Santolino G, Findlay SD, Kohno Y, Matsumoto T, Ishikawa R & Ikuhara Y (2017). Electric field imaging of single atoms. *Nat Commun* **8**, 15631.

Shin DH, Kirkland EJ & Silcox J (1989). Annular dark field electron-microscope images with better than 2 Å resolution at 100 kV. *Appl Phys Lett* **55**, 2456–2458.

Singhal A, Yang JC & Gibson JM (1997). STEM-based mass spectroscopy of supported Re clusters. *Ultramicroscopy* **67**, 191–206.

Smirnov VV & Cowley JM (2002). In-line electron holography with an atomic focuser source. *Phys Rev B Condens Matter Mater Phys* **65**, 641091–641099.

Smith DJ (2008). Ultimate resolution in the electron microscope? *Mater Today* **11**, 30–38.

Smith DJ & Cowley JM (1971). Line patterns in wide-angle convergent beam electron diffraction. *J Appl Crystallogr* **4**, 482–487.

Smith DJ & Cowley JM (1975). Aperture contrast in thick amorphous specimens using scanning transmission electron microscopy. *Ultramicroscopy* **1**, 127–136.

So Y-G & Kimoto K (2012). Effect of specimen misalignment on local structure analysis using annular dark-field imaging. *J Electron Microsc* **61**, 207–215.

Song J, Allen CS, Gao S, Huang C, Sawada H, Pan X, Warner J, Wang P & Kirkland AI (2019). Atomic resolution defocused electron ptychography at low dose with a fast, direct electron detector. *Sci Rep* **9**, 3919.

Sousa AA, Hohmann-Marriott M, Aronova MA, Zhang G & Leapman RD (2008). Determination of quantitative distributions of heavy-metal stain in biological specimens by annular dark-field STEM. *J Struct Biol* **162**, 14–28.

Sousa AA & Leapman RD (2012). Development and application of STEM for the biological sciences. *Ultramicroscopy* **123**, 38–49.

Sparrow CM (1916). On spectroscopic resolving power. *Astrophys J* **44**, 76–86.

Spence JCH (2013). *High-Resolution Electron Microscopy*, 4th ed. John C.H. Spence, Oxford: Oxford University Press.

Spence JCH & Cowley JM (1978). Lattice imaging in STEM. *Optik* **50**, 129–142.

Spence JCH & Tafto J (1983). ALCHEMI: A new technique for locating atoms in small crystals. *J Microsc* **130**, 147–154.

Spencer J, Humphreys CJ & Hirsch PB (1972). A dynamical theory for the contrast of perfect and imperfect crystals in the scanning electron microscope using backscattered electrons. *Philos Mag* **26**, 193–213.

Spurgeon SR, Du Y & Chambers SA (2017). Measurement error in atomic-scale scanning transmission electron microscopy—Energy-dispersive X-ray spectroscopy (STEM-EDS) mapping of a model oxide interface. *Microsc Microanal* **23**, 513–517.

Spurgeon SR, Ophus C, Jones L, Petford-Long A, Kalinin SV, Olszta MJ, Dunin-Borkowski RE, Salmon N, Hattar K, Yang W-CD, Sharma R, Du Y, Chiaramonti A, Zheng H, Buck EC, Kovarik L, Penn RL, Li D, Zhang X, Murayama M & Taheri ML (2021). Towards data-driven next-generation transmission electron microscopy. *Nat Mater* **20**, 274–279.

Steiner S, Wolf J, Glatzel S, Andreou A, Granda JM, Keenan G, Hinkley T, Aragon-Camarasa G, Kitson PJ, Angelone D & Cronin L (2019). Organic synthesis in a modular robotic system driven by a chemical programming language. *Science* **363**, eaav2211 (p1–p8).

Stevens A, Luzi L, Yang H, Kovarik L, Mehdi BL, Liyu A, Gehm ME & Browning ND (2018). A sub-sampled approach to extremely low-dose STEM. *Appl Phys Lett* **112**, 043104.

Stintzing H (1929). Verfahren und Einrichtung zum automatischen Nachweiss, Messung und Zählung von Einzellteilchen beliebiger Art, Form und Grösse. German patent No 485155 (Patent applied for on 14-06-1927, patent granted on 10-10-1929).

Suenaga K, Tence M, Mory C, Colliex C, Kato H, Okazaki T, Shinohara H, Hirahara K, Bandow S & Iijima S (2000). Element-selective single atom imaging. *Science* **290**, 2280–2282.

Suenaga K, Iizumi Y & Okazaki T (2011). Single atom spectroscopy with reduced delocalization effect using a 30 kV-STEM. *Eur Phys J Appl Phys* **54**, 33508 (p1–p4).

Suenaga K & Koshino M (2010). Atom-by-atom spectroscopy at graphene edge. *Nature* **468**, 1088–1090.

Suenaga K, Sato Y, Liu Z, Kataura H, Okazaki T, Kimoto K, Sawada H, Sasaki T, Omoto K, Tomita T, Kaneyama T & Kondo Y (2009). Visualizing and identifying single atoms using electron energy-loss spectroscopy with low accelerating voltage. *Nat Chem* **1**, 415–418.

Synge EH (1928). A suggested method for extending microscopic resolution into the ultra-microscopic region. *Philos Mag* **6**, 356–362.

Synge EH (1931). A microscopic method. *Philos Mag* **11**, 65–80.

Synge EH (1932). An application of piezo-electricity to microscopy. *Philos Mag* **13**, 297–300.

Tanaka N (2014). *Scanning Transmission Electron Microscopy of Nanomaterials: Basics of Imaging and Analysis*. London: Imperial College Press.

Tate MW, Purohit P, Chamberlain D, Nguyen KX, Hovden R, Chang CS, Deb P, Turgut E, Heron JT, Schlom DG, Ralph DC, Fuchs GD, Shanks KS, Philipp HT, Muller DA & Gruner SM (2016). High dynamic range pixel array detector for scanning transmission electron microscopy. *Microsc Microanal* **22**, 237–249.

Taylor KA & Glaeser RM (1974). Electron diffraction of frozen, hydrated protein crystals. *Science* **186**, 1036–1037.

Thomas D, Schultz P, Steven AC & Wall JS (1994). Mass analysis of biological macromolecular complexes by STEM. *Biol Cell* **80**, 181–192.

Thomson MGR (1973). Resolution and contrast in conventional and scanning high-resolution transmission electron-microscopes. *Optik* **39**, 15–38.

Thon F & Willasch D (1972). Imaging of heavy atoms in dark-field electron microscopy using hollow cone illumination. *Optik* **36**, 55–58.

Tian X, Kim DS, Yang S, Ciccarino CJ, Gong Y, Yang Y, Yang Y, Duschatko B, Yuan Y, Ajayan PM, Idrobo JC, Narang P & Miao J (2020). Correlating the three-dimensional atomic defects and electronic properties of two-dimensional transition metal dichalcogenides. *Nat Mater* **19**, 867–873.

Toyama S, Seki T, Anada S, Sasaki H, Yamamoto K, Ikuhara Y & Shibata N (2020). Quantitative electric field mapping of a p-n junction by DPC STEM. *Ultramicroscopy* **216**, 113033.

Trasobares S, López-Haro M, Kociak M, March K, de La Peña F, Perez-Omil JA, Calvino JJ, Lugg NR, D'Alfonso AJ, Allen LJ & Colliex C (2011). Chemical imaging at atomic resolution as a technique to refine the local structure of nanocrystals. *Angew Chem Int Ed* **50**, 868–872.

Treacy MMJ (1982). Optimizing atomic number contrast in annular dark field images of thin films in the scanning transmission electron microscope. *J Microsc Spectrosc Electron* **7**, 511–523.

Treacy MMJ (2011). Z dependence of electron scattering by single atoms into annular dark-field detectors. *Microsc Microanal* **17**, 847–858.

Treacy MMJ & Gibson JM (1993). Coherence and multiple-scattering in "Z-contrast" images. *Ultramicroscopy* **52**, 31–53.

Treacy MMJ, Howie A & Pennycook SJ (1980). Contrast effects in the transmission electron-microscopy of supported crystalline catalyst particles. In *J Inst Phys Conf Ser No. 52*, Mulvey T (Ed.), pp. 261–265. London: The Institute of Physics.

Treacy MMJ, Howie A & Wilson CJ (1978). Z-contrast of platinum and palladium catalysts. *Philos Mag A* **38**, 569–585.

Treacy MMJ & Rice SB (1989). Catalyst particle sizes from Rutherford scattered intensities. *J Microsc* **156**, 211–234.

Tsuno K (2011). Monochromators in electron microscopy. *Nucl Instrum Methods Phys Res A* **645**, 12–19.

Downloaded from https://www.cambridge.org/core. IP address: 68.98.49.119, on 04 Sep 2021 at 06:14:57, subject to the Cambridge Core terms of use, available at https://www.cambridge.org/core/terms. https://doi.org/10.1017/S1431927621012125

Tyukalova E & Duchamp M (2020). Atomic resolution enabled STEM imaging of nanocrystals at cryogenic temperature. *J Phys Mater* **3**, 034006.
Uggerhøj E & Frandsen F (1970). Fast-electron channeling investigated by means of Rutherford scattering. *Phys Rev B* **2**, 582–590.
Unwin PNT & Henderson R (1975). Molecular structure determination by electron microscopy of unstained crystalline specimens. *J Mol Biol* **94**, 425–440.
Van Aert S, Batenburg KJ, Rossel MD, Erni R & Van Tendeloo G (2011). Three-dimensional atomic imaging of crystalline nanoparticles. *Nature* **470**, 374–377.
Van Aert S, De Backer A, Martinez GT, Goris B, Bals S, Van Tendeloo G & Rosenauer A (2013). Procedure to count atoms with trustworthy single-atom sensitivity. *Phys Rev B* **87**, 064107.
Van Aert S, den Dekker AJ, van den Bos A, Van Dyck D & Chen JH (2005). Maximum likelihood estimation of structure parameters from high resolution electron microscopy images. Part II: A practical example. *Ultramicroscopy* **104**, 107–125.
Van Aert S, Van den Broek W, Goos P & Van Dyck D (2012). Model-based electron microscopy: From images toward precise numbers for unknown structure parameters. *Micron* **43**, 509–515.
Van Aert S, Verbeeck J, Erni R, Bals S, Luysberg M, Van Dyck D & Van Tendeloo G (2009). Quantitative atomic resolution mapping using high-angle annular dark field scanning transmission electron microscopy. *Ultramicroscopy* **109**, 1236–1244.
van Benthem K, Lupini AR, Kim M, Baik HS, Doh S, Lee J-H, Oxley MP, Findlay SD, Allen LJ, Luck JT & Pennycook SJ (2005). Three-dimensional imaging of individual hafnium atoms inside a semiconductor device. *Appl Phys Lett* **87**, 034104.
van den Bos KHW, De Backer A, Martinez GT, Winckelmans N, Bals S, Nellist PD & Van Aert S (2016). Unscrambling mixed elements using high angle annular dark field scanning transmission electron microscopy. *Phys Rev Lett* **116**, 246101 (1–6).
van den Bos KHW, Janssens L, De Backer A, Nellist PD & Van Aert S (2019). The atomic lensing model: New opportunities for atom-by-atom metrology of heterogeneous nanomaterials. *Ultramicroscopy* **203**, 155–162.
Van Dyck D, Bokel RMJ & Zandbergen HW (1998). Does crystal tilt enhance the electron interaction? *Microsc Microanal* **4**, 428–434.
Van Dyck D & Op de Beeck M (1996). A simple intuitive theory for electron diffraction. *Ultramicroscopy* **64**, 99–107.
Van Helden A (1977). The invention of the telescope. *Trans Am Philos Soc* **67**, 1–67.
Varela M, Findlay SD, Lupini AR, Christen HM, Borisevich AY, Dellby N, Krivanek OL, Nellist PD, Oxley MP, Allen LJ & Pennycook SJ (2004). Spectroscopic imaging of single atoms within a bulk solid. *Phys Rev Lett* **92**, 095502.
Velazco A, Nord M, Béché A & Verbeeck J (2020). Evaluation of different rectangular scan strategies for STEM imaging. *Ultramicroscopy* **215**, 113021.
Venables JA, Cowley JM & von Harrach HS (1987). A field-emission STEM for surface studies. *EMAG87, Manchester, Inst Phys Conf Ser* **90**, 85–88.
Venkatraman K, Levin BDA, March K, Rez P & Crozier PA (2019). Vibrational spectroscopy at atomic resolution with electron impact scattering. *Nat Phys* **15**, 1237–1241.
Vinothkumar KR & Henderson R (2016). Single particle electron cryomicroscopy: Trends, issues and future perspective. *Q Rev Biophys* **49**, e13.
von Ardenne M (1938*a*). Die grenzen für das Auflösungsvermögen des elektronenmikroskops. *Z Phys* **108**, 338–353.
von Ardenne M (1938*b*). Das Elektronen-Rastermikroskop. Theoretische Grundlagen. *Z Phys* **109**, 553–572.
von Ardenne M (1938*c*). Das Elektronen-Rastermikroskop. Praktische Ausführung. *Z Tech Phys* **19**, 407–416.
von Ardenne M (1939). Intensitätsfragen und Auflösungsvermögen des Elektronenmikroskops. *Z Phys* **112**, 744–752.
von Ardenne M (1940). Über das Auftreten von Schwärzungslinien bei der elektronenmikroskopischen Abbildung kristalliner Lamellen. *Z Phys* **116**, 736–738.
von Harrach HS (1994). Medium-voltage field-emission STEM—The ultimate AEM. *Microsc Microanal Microstruct* **5**, 153–164.
von Harrach HS (1995). Instrumental factors in high-resolution FEG STEM. *Ultramicroscopy* **58**, 1–5.
von Harrach HS (2009). Cold field emission and the scanning transmission electron microscope. *Adv Imaging Electron Phys* **159**, 287.
von Harrach HS, Nicholls AW, Jesson DE & Pennycook SJ (1993). First results of a 300 kV high resolution field-emission STEM. *EMAG 93, Inst Phys Conf Ser* **138**, 499–502.
Voyles PM (2017). Informatics and data science in materials microscopy. *Curr Opin Solid State Mater Sci* **21**, 141–158.
Voyles PM, Grazul JL & Muller DA (2003). Imaging individual atoms inside crystals with ADF-STEM. *Ultramicroscopy* **96**, 251–273.
Voyles PM, Muller DA, Grazul JL, Citrin PH & Gossmann HJL (2002). Atomic-scale imaging of individual dopant atoms and clusters in highly n-type bulk Si. *Nature* **416**, 826–829.
Wall J, Isaacson M & Langmore JP (1974*a*). Collection of scattered electrons in dark field electron-microscopy. II. Inelastic-scattering. *Optik* **39**, 359–374.
Wall J, Langmore J, Isaacson M & Crewe AV (1974*b*). Scanning-transmission electron-microscopy at high-resolution. *Proc Natl Acad Sci USA* **71**, 1–5.
Wall JS & Hainfeld JF (1986). Mass mapping with the scanning transmission electron microscope. *Ann Rev Biophys Biophys Chem* **15**, 355–376.
Wang C, Duan H, Chen C, Wu P, Qi D, Ye H, Jin H-J, Xin HL & Du K (2020). Three-dimensional atomic structure of grain boundaries resolved by atomic-resolution electron tomography. *Matter* **3**, 1999–2011.
Wang J, Huang W, Pei A, Li Y, Shi F, Yu X & Cui Y (2019*a*). Improving cyclability of Li metal batteries at elevated temperatures and its origin revealed by cryo-electron microscopy. *Nat Energy* **4**, 664–670.
Wang P, Zhang F, Gao S, Zhang M & Kirkland AI (2017). Electron ptychographic diffractive imaging of boron atoms in LaB_6 crystals. *Sci Rep* **7**, 2857.
Wang S, Buseck PR & Liu J (1995). High-angle annular dark-field microscopy of Franckeite. *Am Miner* **80**, 1174–1178.
Wang S, Liu J, Buseck P & Cowley JM (1990). Compositional observations of Franckeite using high-angle annular dark-field microscopy. *Proc. XII Int. Conf. Elec. Microsc.*, vol. **4**, pp. 398–399.
Wang SY & Cowley JM (1995). Shadow images for in-line holography in a STEM instrument. *Microsc Res Tech* **30**, 181–192.
Wang X, Li Y & Meng YS (2019*b*). Cryogenic electron microscopy for characterizing and diagnosing batteries. *Joule* **2**, 2225–2234.
Wang Z, Saito M, McKenna KP, Gu L, Tsukimoto S, Shluger AL & Ikuhara Y (2011). Atom-resolved imaging of ordered defect superstructures at individual grain boundaries. *Nature* **479**, 380–383.
Wang ZL (1994). Dislocation contrast in high-angle hollow-cone dark-field TEM. *Ultramicroscopy* **53**, 73–90.
Wang ZL & Cowley JM (1989). Simulating high-angle annular dark-field STEM images including inelastic thermal diffuse-scattering. *Ultramicroscopy* **31**, 437–454.
Wang ZL & Cowley JM (1990). Dynamic theory of high-angle annular-dark-field STEM lattice images for a Ge/Si interface. *Ultramicroscopy* **32**, 275–289.
Wardell IMR & Bovey PR (2009). Cold field emission and the scanning transmission electron microscope. *Adv Imaging Electron Phys* **159**, 221–285.
Wardell IRM, Morphew J & Bovey PE (1973). Results and performance of a high resolution STEM. *Proc. Conf. Scanning Electron Microscopy, Systems and Applications*, Institute of Physics, London, pp. 182–185.
Watanabe M, Kanno M & Okunishi E (2010). Atomic-resolution elemental mapping by EELS and XEDS in aberration corrected STEM. *JEOL News* **45**, 8–15.
Watanabe M & Williams DB (1999). Atomic-level detection by X-ray microanalysis on the analytical electron microscope. *Ultramicroscopy* **78**, 89–101.
Wen Y, Ophus C, Allen CS, Fang S, Chen J, Kaxiras E, Kirkland AI & Warner JH (2019). Simultaneous identification of low and high atomic number atoms in monolayer 2D materials using 4D scanning transmission electron microscopy. *Nano Lett* **19**, 6482–6491.
Wilson T (2011). Resolution and optical sectioning in the confocal microscope. *J Microsc* **244**, 113–121.
Wilson T & Carlini AR (1987). Size of the detector in confocal imaging systems. *Opt Lett* **12**, 227–229.
Wong K, Kirkland E, Xu P, Loane R & Silcox J (1992). Measurement of spherical aberration in STEM. *Ultramicroscopy* **40**, 139–150.
Wu L, Meng Q & Zhu Y (2020). Mapping valence electron distributions with multipole density formalism using 4D-STEM. *Ultramicroscopy* **219**, 113095.

Downloaded from https://www.cambridge.org/core. IP address: 68.98.49.119, on 04 Sep 2021 at 06:14:57, subject to the Cambridge Core terms of use, available at https://www.cambridge.org/core/terms. https://doi.org/10.1017/S1431927621012125

Wu RJ, Mittal A, Odlyzko ML & Mkhoyan KA (2017). Simplifying electron beam channeling in scanning transmission electron microscopy (STEM). *Microsc Microanal* **23**, 794–808.

Xin HL & Muller DA (2009). Aberration-corrected ADF-STEM depth sectioning and prospects for reliable 3D imaging in S/TEM. *J Electron Microsc* **58**, 157–165.

Xu P, Kirkland EJ, Silcox J & Keyse R (1990). High-resolution imaging of silicon (111) using a 100 keV STEM. *Ultramicroscopy* **32**, 93–102.

Xu R, Chen C-C, Wu L, Scott MC, Theis W, Ophus C, Bartels M, Yang Y, Ramezani-Dakhel H, Sawaya MR, Heinz H, Marks LD, Ercius P & Miao J (2015). Three-dimensional coordinates of individual atoms in materials revealed by electron tomography. *Nat Mater* **14**, 1099–1103.

Xu W & LeBeau JM (2018). A deep convolutional neural network to analyze position averaged convergent beam electron diffraction patterns. *Ultramicroscopy* **188**, 59–69.

Yamazaki T, Kawasaki M, Watanabe K, Hashimoto I & Shiojiri M (2002). Effect of small crystal tilt on atomic-resolution high-angle annular dark field STEM imaging. *Ultramicroscopy* **92**, 181–189.

Yamazaki T, Kotaka Y, Kikuchi Y & Watanabe K (2006). Precise measurement of third-order spherical aberration using low-order zone-axis Ronchigrams. *Ultramicroscopy* **106**, 153–163.

Yang H, Lozano JG, Pennycook TJ, Jones L, Hirsch PB & Nellist PD (2015). Imaging screw dislocations at atomic resolution by aberration-corrected electron optical sectioning. *Nat Commun* **6**, 7266.

Yang H, MacLaren I, Jones L, Martinez GT, Simson M, Huth M, Ryll H, Soltau H, Sagawa R, Kondo Y, Ophus C, Ercius P, Jin L, Kovács A & Nellist PD (2017*a*). Electron ptychographic phase imaging of light elements in crystalline materials using Wigner distribution deconvolution. *Ultramicroscopy* **180**, 173–179.

Yang H, Rutte R, Jones L, Simson M, Sagawa R, Ryll H, Huth M, Pennycook TJ, Green MLH, Soltau H, Kondo Y, Davis BG & Nellist PD (2016). Simultaneous atomic-resolution electron ptychography and Z-contrast imaging of light and heavy elements in complex nanostructures. *Nat Commun* **7**, 12532.

Yang JC, Bradley S & Gibson JM (2000). Rapid and semi-automated method for analysis of the number of atoms of ultra-small platinum clusters on carbon. *Microsc Microanal* **6**, 353–357.

Yang Y, Chen CC, Scott MC, Ophus C, Xu R, Pryor A, Wu L, Sun F, Theis W, Zhou J, Eisenbach M, Kent PRC, Sabirianov RF, Zeng H, Ercius P & Miao J (2017*b*). Deciphering chemical order/disorder and material properties at the single-atom level. *Nature* **542**, 75–79.

Yang Y, Zhou J, Zhu F, Yuan Y, Chang DJ, Kim DS, Pham M, Rana A, Tian X, Yao Y, Osher SJ, Schmid AK, Hu L, Ercius P & Miao J (2021). Determining the three-dimensional atomic structure of an amorphous solid. *Nature* **592**, 60–64.

Yankovich A, Berkels B, Dahmen W, Binev P, Sanchez SI, Bradley SA, Li A, Szlufarska I & Voyles PM (2014). Picometre-precision analysis of scanning transmission electron microscopy images of platinum nanocatalysts. *Nat Commun* **5**, 4155.

Yip KM, Fischer N, Paknia E, Chari A & Stark H (2020). Atomic-resolution protein structure determination by cryo-EM. *Nature* **587**, 157–161.

Young N, Li Z, Chen Y, Palomba S, Di Vece M & Palmer R (2008). Weighing supported nanoparticles: Size-selected clusters as mass standards in nanometrology. *Phys Rev Lett* **101**, 246103.

Yu H, Ishikawa R, So Y-G, Shibata N, Kudo T, Zhou H & Ikuhara Y (2013). Direct atomic-resolution observation of two phases in the $Li_{1.2}Mn_{0.567}Ni_{0.166}Co_{0.067}O_2$ cathode material for lithium-ion batteries. *Angew Chem Int Ed* **52**, 5969–5973.

Yu Z, Muller DA & Silcox J (2008). Effects of specimen tilt in ADF-STEM imaging of a-Si/c-Si interfaces. *Ultramicroscopy* **108**, 494–501.

Yücelen E, Lazić I & Bosch EGT (2018). Phase contrast scanning transmission electron microscopy imaging of light and heavy atoms at the limit of contrast and resolution. *Sci Rep* **8**, 2676.

Yun H, Prakash A, Jalan B, Jeong JS & Mkhoyan KA (2020). STEM beam channeling in $BaSnO_3/LaAlO_3$ perovskite bilayers and visualization of 2D misfit dislocation network. *Ultramicroscopy* **208**, 112863.

Zach J (1989). Design of a high-resolution low-voltage scanning electron microscope. *Optik* **83**, 30–40.

Zach J & Haider M (1994). Correction of spherical and chromatic aberrations in a LVSEM. *Proceedings of ICEM-13 (Paris)*, vol. **1**, pp. 199–200.

Zach J & Haider M (1995*a*). Correction of spherical and chromatic aberration in a low-voltage SEM. *Optik* **98**, 112–118.

Zach J & Haider M (1995*b*). Aberration correction in a low voltage SEM by a multipole corrector. *Nucl Instrum Methods Phys Res A* **363**, 316–325.

Zamani RR, Hage FS, Lehmann S, Ramasse QM & Dick KA (2018). Atomic-resolution spectrum imaging of semiconductor nanowires. *Nano Lett* **18**, 1557–1563.

Zeitler E & Thomson MGR (1970*a*). Scanning transmission electron microscopy. I. *Optik* **31**, 258–280.

Zeitler E & Thomson MGR (1970*b*). Scanning transmission electron microscopy. II. *Optik* **31**, 359–366.

Zewail AH (2010). Four-dimensional electron microscopy. *Science* **328**, 187–193.

Zhang JY, Hwang J, Isaac BJ & Stemmer S (2015). Variable-angle high-angle annular dark-field imaging: Application to three-dimensional dopant atom profiling. *Sci Rep* **5**, 12419.

Zhang Q, He X, Shi J, Lu N, Li H, Yu Q, Zhang Z, Chen LQ, Morris B, Xu Q, Yu P, Gu L, Jin K & Nan CW (2017). Atomic-resolution imaging of electrically induced oxygen vacancy migration and phase transformation in $SrCoO_{2.5-\sigma}$. *Nat Commun* **8**, 104.

Zhou D, Mueller-Caspary K, Sigle W, Krause FF, Rosenauer A & van Aken P (2016). Sample tilt effects on atom column position determination in ABF-STEM imaging. *Ultramicroscopy* **160**, 110–117.

Zhou J, Yang Y, Yang Y, Kim DS, Yuan A, Tian X, Ophus C, Sun F, Schmid AK, Nathanson M, Heinz H, An Q, Zeng H, Ercius P & Miao J (2019). Observing crystal nucleation in four dimensions using atomic electron tomography. *Nature* **570**, 500–503.

Zhou L, Song J, Kim JS, Pei X, Huang C, Boyce M, Mendonça L, Clare D, Siebert A, Allen CS, Liberti E, Stuart D, Pan X, Nellist PD, Zhang P, Kirkland AI & Wang P (2020). Low-dose phase retrieval of biological specimens using cryo-electron ptychography. *Nat Commun* **11**, 2773.

Zhou W, Kapetanakis MD, Prange MP, Pantelides ST, Pennycook SJ & Idrobo J-C (2012*a*). Direct determination of the chemical bonding of individual impurities in graphene. *Phys Rev Lett* **109**, 206803.

Zhou W, Oxley MP, Lupini AR, Krivanek OL, Pennycook SJ & Idrobo J-C (2012*b*). Single atom microscopy. *Microsc Microanal* **18**, 1342–1354.

Zhu J & Cowley JM (1982). Microdiffraction from anti-phase boundaries in Cu_3Au. *Acta Crystallogr A* **38**, 718–724.

Ziatdinov M, Dyck O, Maksov A, Li X, Sang X, Xiao K, Unocic RR, Vasudevan R, Jesse S & Kalinin SV (2017). Deep learning of atomically resolved scanning transmission electron microscopy images: Chemical identification and tracking local transformations. *ACS Nano* **11**, 12742–12752.

Zuo JM, Shah AB, Kim H, Meng Y, Gao W & Rouviére J-L (2014). Lattice and strain analysis of atomic resolution z-contrast images based on template matching. *Ultramicroscopy* **136**, 50–60.

Zworykin VA (1934). Electric microscope. *1st Congresso Internazionale di Electroradio-biologia Atti*, vol. **1**, pp. 672–686.

Zworykin VA, Hillier J & Snyder RL (1942). A scanning electron microscope. *ASTM Bull* **117**, 15–23.

Downloaded from https://www.cambridge.org/core. IP address: 68.98.49.119, on 04 Sep 2021 at 06:14:57, subject to the Cambridge Core terms of use, available at https://www.cambridge.org/core/terms. https://doi.org/10.1017/S1431927621012125